8-2018

Low Temperature Simulations Framework For Quantum Dots And Point Contacts.

Harshad Sahasrabudhe
Purdue University

Recommended Citation

Sahasrabudhe, Harshad, "Low Temperature Simulations Framework For Quantum Dots And Point Contacts." (2018). *Open Access Dissertations*. 2060.
https://docs.lib.purdue.edu/open_access_dissertations/2060

LOW TEMPERATURE SIMULATIONS FRAMEWORK FOR QUANTUM DOTS AND POINT CONTACTS

A Dissertation

Submitted to the Faculty

of

Purdue University

by

Harshad Sahasrabudhe

In Partial Fulfillment of the

Requirements for the Degree

of

Doctor of Philosophy

August 2018

Purdue University

West Lafayette, Indiana

THE PURDUE UNIVERSITY GRADUATE SCHOOL
STATEMENT OF DISSERTATION APPROVAL

Dr. Michael Manfra, Chair
Department of Physics and Astronomy
Dr. Gerhard Klimeck, Chair
Department of Electrical and Computer Engineering
Dr. Rajib Rahman
Department of Electrical and Computer Engineering
Dr. Gabor Csathy
Department of Physics and Astronomy
Dr. Chris Greene
Department of Physics and Astronomy

Approved by:
Dr. John Finley
Head of the Department of Physics and Astronomy

Dedicated to Aai, Baba, Aaji, Mihir, and Leena.

ACKNOWLEDGMENTS

First and foremost, I would like to thank Prof. Rajib Rahman for his guidance, patience and support. Without his advice, this work would have been close to impossible. I also thank Prof. Michael Manfra for his guidance, vision and support. I thank Prof. Gerhard Klimeck for providing the infrastructure, computational resources and guidance. I thank Prof. Gabor Csathy and Prof. Chris Greene for serving as my committee members and for their guidance.

I extend my sincere thanks to Prof. Michael Povolotskyi and Dr. Bozidar Novakovic for intellectual discussions, support, and encouragement during crucial times of my PhD. I would have been lost if not for their help.

I thank Prof. Zubin Jacob for his support, guidance and enlightening discussions. I thank Prof. Bart Sorée for allowing me to do an internship at IMEC, Leuven and for his guidance. I thank Prof. Timothy Boykin for his quick correspondence over email and very helpful discussions. I thank Prof. Laszlo Gutay, with whom I was a teaching assistant for 5 terms, for his continued trust and support, and for letting me explore and learn how to teach effectively. I also want to thank Prof. Supriyo Datta, who taught me a lot through his lectures and discussions.

I thank my collaborators Jimmy Nakamura and Saeed Fallahi, who worked in the Manfra group, Kok Wai Chan who worked in the Dzurak group at UNSW, Rifat Ferdous, Archana Tankasala, Yu Wang, Hesameddin Ilatikhameneh, Tarek Ameen, and Fan Chen who worked in the Klimeck group, Prashant Shekhar who worked in the Zubin Jacob group, and Dimitrios Andrikopoulos who worked in IMEC, Leuven. These collaborations were extremely productive, and helped me extend my knowledge of the field, and understanding of the scientific community and culture.

I thank my colleagues Daniel Valencia, Chin-Yi Chen, Daniel Mejia, Prasad Sarangapani, Kuang-Chung Wang, James Charles, Daniel Lemus, Kai Miao, Yu He, Yuling Hsueh, Jun Huang, Gustavo Valencia, Xinchen Guo, Samik Mukherjee, Jared Bland and Shiva Teja Konakanchi for their warm support and encouragement.

I thank the Physics department staff Sandy Formica, Pam Blakey, Carol Buuck and Dr. Andrew Lewicki, and NCN staff Vicki Johnson, Ashlee Bryne, Leslie Schumacher, Lynn Zentner and Lowell Williams for all the administrative help they provided.

I thank my close friends Anupriya Karippadath, Ishan Srivastava, GV Srikanth, Priya Murria, Sarath Ramadurgam, Vandith Pamuru, Venkatesh Sridhar, Rithesh Iyer, Yash Gandhi and Vatsal Purohit.

Finally, and most importantly I thank my father Girish Sahasrabudhe, mother Neelima Sahasrabudhe, grandmother Prabha Sahasrabudhe, brother Mihir Sahasrabudhe and fiancée Leena Sathe for their unconditional love and support. Without them this would have been impossible.

TABLE OF CONTENTS

Page

LIST OF TABLES . . . ix

LIST OF FIGURES . . . x

SYMBOLS . . . xvi

ABBREVIATIONS . . . xvii

NOMENCLATURE . . . xviii

ABSTRACT . . . xix

1 INTRODUCTION . . . 1
  1.1 Quantum Computation . . . 3
  1.2 Physical realizations of quantum computers . . . 6
    1.2.1 FQHE based topological quantum computing . . . 7
    1.2.2 Si/SiO$_2$ based electron spin qubits . . . 18
  1.3 Importance of simulations . . . 28

2 ELECTROSTATIC SIMULATION FRAMEWORK . . . 31
  2.1 Free charges . . . 32
  2.2 Fixed charges . . . 34
  2.3 Poisson equation . . . 35
  2.4 Discretization . . . 35
    2.4.1 Finite element method . . . 36
    2.4.2 Meshing . . . 37
  2.5 Schrödinger-Poisson self-consistency . . . 38
  2.6 Numerics . . . 39
  2.7 Parallelization . . . 40
  2.8 Testing . . . 41
  2.9 Scaling . . . 41

3 OPTIMIZATION OF EDGE STATE VELOCITY IN THE INTEGER QUANTUM HALL REGIME . . . 45
  3.1 Introduction . . . 45
  3.2 Methodology . . . 49
    3.2.1 Poisson equation . . . 49
    3.2.2 Schrödinger equation . . . 51
    3.2.3 Discretization and numerics . . . 55
    3.2.4 Self-consistency . . . 56

Page
3.2.5 Quantum transport . . . 56
3.3 Results . . . 59
3.3.1 QPC resistance benchmark with experiment . . . 59
3.3.2 Sub-band energy and sheet density profiles . . . 61
3.3.3 QPC conductance in the IQHE regime . . . 63
3.3.4 Edge state wavefunctions in the QPC scattering region . . . 65
3.4 Optimization of edge state velocity . . . 65
3.4.1 Magnetic field dependence of velocity . . . 66
3.4.2 Gate voltage dependence of velocity . . . 69
3.4.3 Quantum well width dependence of velocity in double-sided delta doped structure . . . 71
3.5 Summary . . . 71
4 COMPUTATIONAL MODELING OF EXCHANGE SPLITTING IN SILICON-SILICON DIOXIDE DOUBLE QUANTUM DOTS . . . 75
4.1 Introduction . . . 75
4.2 Methodology . . . 76
4.2.1 Electrostatic simulations . . . 77
4.2.2 Tight binding simulations . . . 82
4.2.3 Full configuration interaction simulations . . . 82
4.3 Results . . . 83
4.3.1 Comparison of effective-mass and tight-binding energy levels . . 84
4.3.2 Tight binding model energy spectrum . . . 84
4.3.3 Two-electron energy spectrum . . . 84
4.3.4 Ground singlet composition and singlet anti-crossings . . . 86
4.3.5 Exchange splitting vs detuning . . . 89
4.3.6 Exchange splitting vs oxide thicknesses . . . 90
4.4 Summary . . . 90
5 SUMMARY AND OUTLOOK . . . 93
REFERENCES . . . 97
A WEAK FORMULATION OF SCHRÖDINGER AND POISSON EQUATIONS . . . 107
B BOUNDARY CONDITIONS FOR THE POISSON EQUATION . . . 111
C NEWTON'S METHOD FOR ITERATIVELY SOLVING THE SCHRÖDINGER-POISSON EQUATIONS . . . 113
D PREDICTOR-CORRECTOR METHOD . . . 117
E AGREEMENTS FOR REUSE OF PUBLISHED PAPERS . . . 121
VITA . . . 124

LIST OF TABLES

Table Page

2.1 Comparison of simulation and theory for harmonic oscillator eigenvalues . 41

4.1 Gate names (Fig. 4.3) and voltages used in electrostatic simulations. . . . 80

LIST OF FIGURES

Figure Page

1.1 Two types of heterostructures of GaAs (blue), AlGaAs (cyan) and AlAs (green) materials (see Figs. 7 and 6 respectively in [25]). The 2-dimensional electron gas (2DEG) is in GaAs, in a quantum well sandwiched between two AlGaAs layers in the left figure, and at the interface of a AlGaAs layer in the right figure. The magnetic field is applied perpendicular to the 2DEG. 8

1.2 a) Cyclotron orbits of electrons in a 2-dimensional electron gas (2DEG) with a perpendicular magnetic field. The cyclotron orbits are cut-off at the edges due to an electric field, because of which the electrons propagate at the edges. Contacts are added as shown using gold (shaded) regions to make a Hall bar. b) Energy as a function of position at the edge. The confinement at the edges due to an external potential V_{ext} raises the LLs (orange) such that they intersect with the Fermi energy level E_F (gray dashed line) creating edge states (half-filled dots). 9

1.3 Schematics of the top gates and 2DEG edges of a) a QPC in the strong back-scattering regime, b) weak back-scattering regime and c) a Fabry-Pérot interferometer. The red dashed lines with arrows indicate propagating electrons/quasi-particles along the 2DEG edges. The green dotted lines indicate tunneling across the edges. 14

1.4 Comparison between density and potential at the edge with and without electron interactions. a) For a smooth edge potential, the density at the edge has sharp steps as each LL has high DOS, all of which escapes the Fermi level at a single spatial point. b) When electron interactions are turned on, the Fermi level gets pinned to a LL causing a more energetically favorable smooth density variation. The edge has compressible (metallic) regions where the density changes smoothly and the potential changes very slowly, and incompressible (insulating) regions where the density is constant and potential varies faster. 17

1.5 An illustration of 2 qubits made from the spins of electrons trapped at the interface of silicon and silicon-dioxide materials under Aluminum gates with an applied positive voltage. The arrows represent electron spins. . . . 18

Figure Page

1.6 An illustration of the one and two electron energy spectrums in a double quantum dot vs detuning for a total of 2 electrons in the dots. a) One-electron energy spectrum shows the bonding and anti-bonding orbitals with spin energy levels separated by Zeeman splitting. The dashed lines show energy levels of $|\psi_L$ and $|\psi_R$ in left and right dots respectively at zero magnetic field. b) Two-electron energy spectrum shows the singlet and triplet states in the bonding and anti-bonding orbitals. The $|S(A,A)$, $|S(B,A)$ and $|S(B,B)$ states interact at low detuning to give four anti-crossings symmetrically located around zero detuning. The dashed lines show the behavior of energy levels when the off-diagonal singlet terms are turned off by uncoupling the dots. E_J is the exchange coupling between the $|T_0(B,A)$ and $|S(1,1)$ states. 25

2.1 An illustration showing the various factors that affect electrostatics in heterostructures. 31

2.2 Comparison between a mesh created using only tetrahedra (b) and by mixing tetrahedra, pyramids, prisms and hexahedra (a). (a) contains 745 vertices and (b) contains 9726 vertices. Both have 20nm resolution on the left side and 5nm resolution on the right in vertical direction. (a) uses pyramids and prisms to connect the tetrahedra to cuboids. 38

2.3 Dependency graph of numerical libraries 39

2.4 Partitioning of Schrödinger (blue) and Poisson (red) regions. The numbers show the processor onto which that part of the region goes. The shaded part is the spatial region which is on processor 0 of Schrödinger and processor 1 of Poisson mesh. Thus, quantum density is calculated on processor 0, and needs to be communicated to processor 1. 40

2.5 Strong scaling plots of a self-consistent quantum dot Schrödinger-Poisson calculation. a) Total start to end simulation time. b) Set-up time, during which the intersection of Schrödinger and Poisson meshes is calculated and communicated. The scaling for set-up is bad when most elements of the Schrödinger mesh fall in a region of the Poisson mesh that resides on a small number of processors. c) Semi-classical system solution time, during which the Poisson equation (Eq. 2.9) is solved self-consistently with the semi-classical density (Eqs. 2.4, 2.5) using the Newton's method discussed in Appendix C. d) Quantum system solution time, during which the Poisson equation (Eq. 2.9) is solved self-consistently with the Schrörindger equation (Eq. 2.1) using the PC method described in Appendix D. 43

Figure Page

3.1 The details of heterostructure and gate layout used for benchmarking the simulation method. **a)** A cartoon showing the different layers and the shaded 2DEG location in the 91 nm deep single hetero-junction structure with modulation doping. A uniform doping profile with a concentration of 4.8×10^{18} cm^{-3} between 17 and 31 nm depths was used in experiments. **b)** The conduction band and electron density profiles of the quantum well solved self-consistently using a 1D Schrödinger-Poisson simulation. Valence band maximum on the left edge is at 0 eV, and the dashed line is the Fermi level. **c)** The 1.5μm (cross-section) × 1.2μm (transport direction) × 250nm (growth direction) sized finite element mesh used to discretize Poisson equation for the QPC. The mesh contains tetrahedral elements (orange) to efficiently fill the dielectric regions which contain no free charge, and cuboid elements (blue) in the regions containing free charges. Pyramid and prism shaped elements (orange) are used to connect dielectric regions to charged regions. The cuboids in charged regions are thin along the growth direction, in which potential changes fast and coarse along the lateral direction in which potential changes slowly. The mesh contains $\sim$ 2.16 million points at which the electrostatic potential is solved. 47

3.2 The simulation flowchart. Quasi-1D Schrödinger and Poisson equations are solved self-consistently to get the electrostatic potential and 2DEG density near the QPC. Section 3.2.1 gives details of the Poisson equation, which takes into account top gates, surface states, incomplete donor ionization and uses a mixed FEM mesh to solve complex heterostructures efficiently. The quasi-1D Schrödinger equation is solved for QPCs as described in Section 3.2.2. The potential profile obtained from electrostatics is used in quantum transport simulations (Sec. 3.2.5) for calculating the QPC transmission, local density of states (LDOS), current densities, wavefunctions and their velocities. Electrostatic simulations are done using the NEMO5 [104] package, while the quantum transport simulations are done using the Kwant [106] package. 50

3.3 Comparison between experimentally measured and computed resistance of a 300 nm wide QPC. The measurement was done at 300 mK in 0 T magnetic field and using a constant AC current source of 10 nA. The red (light) and blue (dark) dashed lines indicate the depletion voltages in simulation and experiment respectively. 60

Figure Page

3.4 Sheet densities at different gate voltages for a 300 nm wide QPC, calculated using the Schrödinger-Poisson solver in a magnetic field of 2.2 T. Panels **c)** and **d)** show cuts along the X and Y axes, passing through the middle of the QPC. Sheet density in the bulk is $1.34\times10^{11}\text{cm}^{-2}$, and in the incompressible strip for $n = 1$ LL has a density of $1.06 \times 10^{11}\text{cm}^{-2}$. The incompressible strip can be seen as a light green region near the depleted 2DEG in **a)** and **b)**, and as flat region in **c)** and **d)**. 61

3.5 Sub-band energy ($E_F = 0$) and sheet density profiles near the edge of the 2DEG defined by depletion top gates at a magnetic field of 2.2 T (bulk filling factor $\nu_{\text{bulk}} = 2.52$) and gate voltage of -0.446 V compared to zero magnetic field values plotted using a dashed line. Edge state wavefunctions at the Fermi level for $\nu = 1$, 2 and 3 Landau levels obtained from quantum transport are also shown. 62

3.6 Conductance vs applied gate voltage of a 300 nm wide QPC at magnetic fields of 0.9T, 1.36T and 2.71T, and bulk filling factors of $\nu_{\text{bulk}} = 6.00$, $\nu_{\text{bulk}} = 3.97$ and $\nu_{\text{bulk}} = 1.99$ respectively. Each point represents an independent electrostatic simulation. The edge mode of even ν^{th} Landau level starts conducting just above a bulk filling factor of $\nu_{\text{bulk}} = \nu$. This is why we have conductance corresponding to one less edge state than the filling factor. 64

3.7 A plot of the 3 edge modes in the QPC structure in figure 3.1 for $n = 1$ (**a**), $n = 2$ (**b**) and $n = 3$ (**c**) Landau levels at $V_g = -0.342$V and $B =$ 0.9T. The arrows show the direction and relative magnitude of the current density. The conductance of QPC is $2 \times 2e^2/h$, since the innermost mode is reflected by the QPC. 64

3.8 Electric field expectation values of edge modes of $n = 1, 2, 3$ LLs for four different structures are plotted as a function of the spin-less bulk filling factor. The structures are described in more detail in section 3.4. Applied gate voltages (V_g) are -0.34V, -0.54V, -0.1V and +0.1V for plots a), b), c) and d) respectively. 67

3.9 a) and b): Velocities of edge states with spin for the structure in fig 3.8a) and d) respectively plotted as a function of the bulk filling factor ν_{bulk}. . . 68

3.10 Velocities of edge modes for outermost ($n = 1$) $n-$Landau level in same four structures as figure 3.8 at different magnetic fields are plotted as a function of the gate voltage. The spin-less bulk filling factors for the plotted magnetic fields are: a) $n_{\text{bulk}} = 3.04$, 1.51 and 1.14; b) $n_{\text{bulk}} = 2.96$, 2.12 and 1.27; c) $n_{\text{bulk}} = 3.75$, 1.88 and 1.40; d) $n_{\text{bulk}} = 2.93$, 2.14 and 1.44; respectively. 70

Figure Page

3.11 Edge state velocity for the n=1 Landau level averaged over different gate voltages as a function of the quantum well width for the structure in fig. 3.8d. 72

4.1 An illustration of the various device parameters in Si/SiO_2 double quantum dot. t_{SiO_2} and $t_{Al_2O_3}$ are the SiO_2 and Al_2O_3 thicknesses under the gate, $p = 36$ nm is the gate pitch, w is the gate width and d is the gate separation such that $p = w + d$ 77

4.2 Flowchart describing the calculation of two-electron wavefunctions and energy levels from computationally calculated tight binding one-electron wavefunctions. The electrostatic potential used for tight binding calculations is self-consistently calculated using the electrostatic simulation framework. 78

4.3 Finite element mesh used to discretize Schrödinger and Poisson equations with top gates shown as shaded regions. The mesh has $\sim 550,000$ nodes and $\sim$ 3.5 million elements. 79

4.4 An illustration of the gate voltages, dot charges and dot-gate capacitances. Top gates are green rectangles and charges are blurry red ellipses. 81

4.5 a) - c) Comparison of the lowest four energy levels obtained from effective-msss Hamiltonian (black/dark) and tight-binding Hamiltonian (cyan/light) as a function of detuning for 8-, 10- and 12-nm dot separation respectively. The Fermi level used in effective-mass electrostatic simulations is at 0 eV. d) - i) Anti-bonding, and m) - u) bonding orbital wavefunctions obtained from tight binding model. d) m), g) p) and j) s) are for leftmost, e) n), h) q) and k) t) are for zero, and f) o) i) r) and l) u) are for rightmost detuning points for 8-, 10- and 12-nm dot separation respectively. All the calculations are done using a gate pitch $p = 36$ nm, Al_2O_3 thickness $t_{Al_2O_3} = 1$ nm and SiO_2 thickness $t_{SiO_2} = 5.9$ nm. 85

4.6 a) - c) Tight binding energy spectrum for the double quantum dot as a function of detuning for 8-, 10- and 12-nm dot separations. The black lines with circles are the levels used in FCI calculations, whereas red lines with crosses are not used in FCI. The Fermi level used in effective-mass electrostatic simulations is at 0 eV. All the calculations are done using a gate pitch $p = 36$ nm, Al_2O_3 thickness $t_{Al_2O_3} = 1$ nm and SiO_2 thickness $t_{SiO_2} = 5.9$ nm. 86

4.7 a) - c) Two-electron energy levels obtained from FCI simulations for 8-, 10-, and 12-nm separation. The Fermi level used in effective-mass electrostatic simulations is at 0 eV. All the calculations are done using a gate pitch $p = 36$ nm, Al_2O_3 thickness $t_{Al_2O_3} = 1$ nm and SiO_2 thickness $t_{SiO_2} = 5.9$ nm.87

Figure Page

4.8 a) - c) Contributions from $|S(B,B)$, $|S(A,A)$ and $|S(B,A)$ singlets to the ground singlet. Dashed lines show the anti-crossing points (not (1,1)-(0,2) anti-crossings) where amplitudes of $|S(B,B)$ and $|S(B,A)$ are equal. All the calculations are done using a gate pitch $p = 36$ nm, Al_2O_3 thickness $t_{Al_2O_3} = 1$ nm and SiO_2 thickness $t_{SiO_2} = 5.9$ nm. 87

4.9 a) - c) Exchange splitting vs detuning for different dot separations. All the calculations are done using a gate pitch $p = 36$ nm, Al_2O_3 thickness $t_{Al_2O_3} = 1$ nm and SiO_2 thickness $t_{SiO_2} = 5.9$ nm. 88

4.10 Exchange splitting at zero detuning vs SiO_2 and Al_2O_3 oxide thicknesses. . 89

C.1 An example of a Newton iteration with 1 function and 1 variable. 113

D.1 Density of states (DOS) for periodicity in 3, 2, 1 and 0 directions. . . . 117

D.2 Flow chart of the Predictor-corrector method. Inner loop uses Newton's method to solve predictor Poisson equation and gives a potential update to the outer Schrödinger solver. Initial potential is obtained by solving Poisson equation with semi-classical density. 118

SYMBOLS

e	elementary charge
ψ, Φ	3-dimensional single electron wavefunction
χ	2-dimensional single electron wavefunction
ψ	1-dimensional single electron wavefunction
Ψ	2-electron wavefunction
σ	sheet density
V	electrostatic potential
m^*	effective mass
E_F	Fermi level
E_C	conduction band minimum
E_V	valence band minimum
E	electric field
B	magnetic field
E_Z	Zeeman splitting
ϕ_0	magnetic flux quantum
v	velocity
n	spinless Landau level index
ν	spinful Landau level index
I	current
H_{SO}	spin-orbit Hamiltonian
H_{nuc}	hyperfine Hamiltonian

ABBREVIATIONS

2DEG	2-dimensional electron gas
QD	quantum dot
QPC	quantum point contact
DOS	density of states
IQHE	integer quantum Hall effect
FQHE	fractional quantum Hall effect
LL	Landau level
CF	composite Fermion
FPI	Fabry-Pérot interferometer
MZI	Mach-Zehnder interferometer
AB	Aharonov-Bohm
CD	Coulomb dominated
Res	reservoir
SET	single electron transistor
S	source
D	drain
SD	Slater determinant

NOMENCLATURE

GaAs	gallium arsenide
AlGaAs	aluminum gallium arsenide
AlAs	aluminum arsenide
Si	silicon
SiO_2	silicon-dioxide
Al	aluminum
Al_2O_3	aluminum-dioxide

ABSTRACT

Sahasrabudhe, Harshad Ph.D., Purdue University, August 2018. Low Temperature Simulations Framework For Quantum Dots And Point Contacts. Major Professors: Gerhard Klimeck and Michael Manfra.

Quantum computing is becoming increasingly important due to its potential in solving complex optimization problems such as protein folding, and the ability to model correlated electronic systems. Designing of semiconductor based quantum computers is challenging due to the vast number of parameters that need to be optimized from fabrication to their operation. Simulations of these devices could help with the design process. A computational modeling framework is presented that can model quantum point contacts and quantum dots, which are the building blocks of semiconductor based quantum computers. Care was taken to minimize the number of parameters, and use only those parameters that are connected directly to the devices and materials. The devices for fractional quantum Hall effect based topological quantum computers and electron spin based quantum computers are considered. The simulation results matched experiments, based on which predictions for improved devices are made.

1. INTRODUCTION

Mesoscopic electronic devices have progressed at a very fast pace since the invention of the transistor. Downscaling for efficiency and speed has happened over many generations of devices such as bipolar junction transistors (1948), metal-oxide-semiconductor field effect transistors [1] (1960), high electron mobility transistors [2] (1979) and the more recent fin field-effect transistors [3] (2001). Accompanying the improvement of devices were innovations in the processes used to fabricate them, which spurred materials research and led to advances in condensed matter physics, most notably the discovery of the integer [4] (1980) and fractional [5] (1982) quantum Hall effects (QHE).

Over the years the devices, and the circuits made using them have become increasingly complicated, requiring modeling tools to shorten the design time. The devices themselves are nearing the limit of downscaling due to the unwanted tunneling of electrons through them. Computationally solving some of the currently unsolved and important problems in quantum chemistry (such as protein folding), in machine learning (such as programming of human-brain-sized neural networks), in many-body interacting quantum systems, and in other fields remains intractable using transistor-based processors.

Recent advances in condensed matter physics, and the prospect of tackling these problems using the principles of superposition and entanglement in quantum mechanics has replenished the interest in quantum computation [6–8]. Quantum computers based on semiconductors, which are just one of the many different candidates [9], have recently attracted interest. Semiconductor based quantum computers are important because of the highly developed semiconductor processing technology that is already in place from the years of research and development in the field. They are also favorable due to the possibility of fitting a million quantum bits (qubits) on a single chip [10, 11]. Recent developments on quantum computing devices based on silicon [12] and gallium arsenide [13] have put this field on fast track. These devices, just like the transistor based computers that came before them, are very difficult to design, requiring fine tuning of a vast number of parameters from fabrication to their operation. Modeling of these devices for better operation and scaling has become increasingly important.

In this thesis a tool is presented, which can realistically model some building blocks of semiconductor based quantum computing devices, such as quantum point contacts (QPCs) and quantum dots (QDs). The development of the tool is guided by the following 3 constraints:

1. *Parameters*: Parameters used should be directly tied to the experiments and their number should be as small as possible.
2. *Experimental agreement*: The model should capture all the relevant physics and the results should agree with the experiment.
3. *Prediction*: Predictions should be reliable as well as provide insights into how the experiments are to be modified.

The biggest challenge presented by these constraints is keeping the computational cost manageable while considering interactions between electrons. This challenge is addressed in Chapter 2.

Even though the behavior of QDs (zero-dimensional) and that of QPCs (one-dimensional) are completely different, the tool tackles them both by solving the effect of gating, heterostructure interfaces, surface states, and doping on the micro-meter scale on electrons. The electrostatics parameters used in this tool are the gate and heterostructure geometry, gate voltages, doping density and profile, and surface charge. The material parameters used are band gap, effective mass and dielectric constant. The output from implementation of the tool includes quantities like the electrostatic potential profile and the electron densities. Further processing of the output is specific to the device under investigation and produces quantities such as QPC conductance, edge-state velocities, QD charging energies, double QD exchange splitting and so on.

In the following sections of the introduction, the requirements for physical realization of quantum computing and the different approaches that are being currently researched are introduced. Topological quantum computation using anyonic (as opposed to Fermionic or Bosonic) particles in the fractional quantum Hall (FQH) effect is discussed. Topological quantum computation is less error prone than that based on spatial information, e.g. electron spins trapped in quantum dots, because most of the noise affecting the quantum system is spatial. The 5/2 FQH state could be formed from the anyonic particles that are required by topological quantum computers [14]. The devices that were proposed for detection of these anyonic particles, namely the quantum Hall interferometers, are discussed in this context. Electrons in quantum dots can also be used as qubits for universal quantum computation. Single and double qubit operations based on electron spins trapped in quantum dots has been demonstrated [15,16], and ongoing efforts are focused on scaling this system to a large number of operations qubits. The simulation model, results and predictions for GaAs/AlGaAs useful in topological quantum computers are presented in Chapter 3, and those for Si/SiO_2 based quantum dots are presented in Chapter 4.

1.1 Quantum Computation

Superposition

Classical computation uses the ON or OFF states of wires as "bits" for storing and processing information. For example, the number 8 can be stored as an ON state of 3 wires $(111)_2$. Quantum computation uses quantum bits ("qubits") which are two state quantum systems that can be in a *superposition* of the two states. A general state of a qubit can be written as the wavefunction $|\psi \;\; = \alpha\,|0 \;\; + \beta\,|1$, where $|0$ and $|1$ are the two orthogonal states of the qubit, α and β are two complex numbers such that $|\alpha|^2 + |\beta|^2 = 1$, and the probabilities of the measuring $|0$ and $|1$ are $|\alpha|^2$ and

$|\beta|^2$ respectively. The complex numbers can be represented by angles θ and ϕ made with the $z-$ and $x-$ axes by a unit vector centered at the origin, so that $\alpha = \cos(\theta/2)$ and $\beta = e^{i\phi}\sin(\theta/2)$. The general state $|\psi\rangle$ of a qubit can then be visualized to be anywhere on the surface of a unit sphere, known as the Bloch sphere, with the states $|1\rangle$ and $|0\rangle$ along $+z$ and $-z$ axes.

Measurement

Measurement collapses the superposition of quantum state into one of the states $|0\rangle$ or $|1\rangle$. Measuring the wavefunction of a qubit $|\psi\rangle = \alpha|0\rangle + \beta|1\rangle$ will result in the qubit collapsing into $|0\rangle$ or $|1\rangle$ with a probability of $|\alpha|^2$ and $|\beta|^2$ respectively.

Entanglement

An n-bit computer can store 2^n different states, as each bit can be in a 0 or 1 state. Classical computers can only process 1 of the 2^n states at a time as the classical bit can only be either 0 or 1. Quantum computers can process an arbitrary number of states spanned by the 2^n states, based on the physical connections between the qubits. This is made possible by the principle of superposition (overlap of 0 and 1 states of a qubit) combined with the phenomenon of entanglement of multiple qubits. Entanglement forces the final state of a qubit to be dependent on the outcome of measurement of another qubit. Two qubits can be entangled using two-qubit reversible gates such as the controlled-NOT (CNOT) gate.

Decoherence

The qubit can interact with its environment in various ways leading to decay in its state, a phenomenon known as decoherence, which poses one of the biggest challenges in building large quantum computers. Decoherence is characterized by three time scales:

- T_2 related to the variability of repeated experiments on a single qubit, i.e. low frequency variations in the local energy landscape.
- T_2 related to the processes which disturb the qubit for a short time in which the qubit absorbs and emits energy from the environment regaining its initial energy state.
- T_1 related to the eventual loss of the energy stored in the qubit to the environment for example by lattice vibrations.

The T_2 and T_1 processes lead to an irreversible loss of information. T_2 time can be lengthened by rotating the qubit using echo techniques [15, 17–19], by making the qubit undergo T_2 evolution for an equal time on diametrically opposite ends of the Bloch sphere, which reverses the phase information loss to a certain extent. The error rates can be reduced by using two level states that rely on the topology of the system and are immune to changes in the local environment. An example of such a topological system would be the Majorana zero modes at the interface of a high spin orbit material (e.g. InAs) and a superconductor (e.g. Al) [14, 20]. Proposed quasiparticles in the 5/2 fractional quantum Hall effect also have this quality, provided we are able to engineer systems that support the fragile state.

Universal quantum computing

Classical computers use transistors to build gates for manipulating bits of information. For example, the NAND gate acts on two bits and gives an ON state only if both the bits are OFF. To achieve a universal classical computer, any type of classical gate can be built using NAND gates. In quantum computers, the gates have to be reversible for the qubit state to remain coherent ($|\alpha|^2 + |\beta|^2 = 1$). As the phase ($\phi$) between $|0\rangle$ and $|1\rangle$ can be any real number, an infinite number of quantum gates are possible; therefore, it is impossible to define a complete set of quantum gates for a universal quantum computer. However, any quantum gate can be approximated by repeated application of gates from a small set [21], e.g. the Hadamard, controlled-NOT and $\pi/8$ gates. All quantum algorithms are based on the recipe of initialization of qubits in a known state, coherent evolution using a combination of unitary gates, and finally measurement of individual qubits [22].

Requirements for quantum computers

The requirements for quantum computers, as pointed out by Ladd et. al [9], can be described as follows:

1. The qubit must be isolated from the environment to prevent leakage of information (e.g. the qubit state parameters α, β and ϕ).
2. The qubit design must be scalable: total energy and spatial cost of the quantum computer must not increase exponentially with the number of qubits.
3. The quantum computer must support universal logic: any point on the Bloch sphere must be reachable up to a certain error using a finite number of qubit operations.
4. The qubit should be correctable: it should be possible to remove entropy from the qubit to preserve its state. Error correction algorithms such as surface codes can be used [23].

1.2 Physical realizations of quantum computers

The first requirement of isolation of a two level system from the environment to perform single and double qubit operations has been satisfied in many physical systems such as trapped ions, nitrogen vacancies in diamond, superconducting qubits, electrons trapped in quantum dots or single donors in silicon. Scalability quickly becomes an issue due to the fact that addressing one or two qubits out of many requires local features near each qubit. Also, placing many qubits in a small area leads to the generation of heat, which will ultimately destroy the quantum state. The fourth requirement of correctability adds to these problems, as the correction algorithms need on the orders of 10-100 qubits for an available qubit computing unit, thus increasing the total number of physical qubits 10-100 fold.

The issues with scalability have been pointed out in semiconductor based electron spin qubits, and some solutions to these problems have also been provided [10, 11]. The proposed topological qubits do not need an apparatus for error correction, thus naturally addressing some issues with scalability. These two technologies, along with the mature superconducting qubit technology have had large investments from companies such as Intel, Microsoft and Google. Topological and electron spin qubits are discussed in Sections 1.2.1 and 1.2.2 respectively.

1.2.1 FQHE based topological quantum computing

Topological quantum bits based on anyonic quasiparticles in the FQHE were first proposed by Das Sarma et al [24]. In the following sub-sections, the IQH, FQH effects and interferometery experiments are introduced, after which the electrostatic QPC simulations are motivated. It should be noted that a complete description of IQHE and FQHE requires the consideration of disorder, whereas only a simple and concise physical picture without disorder is provided here. The QPC simulations are described in detail in Chapter 3.

Integer Quantum Hall Effect (IQHE)

Integer quantum Hall effect can be observed in a 2-dimensional electron gas (2DEG) at a clean interface of 2 materials, such as GaAs and $\mathrm{Al_xGa_{1\text{-}x}As}$ (see Fig. 1.1), when an external perpendicular magnetic field is applied. Due to the perpendicular magnetic field, the electrons (which have a lateral intrinsic velocity as they are trapped in a 1D quantum well) undergo a circular motion (see Fig. 1.2a) known as a cyclotron orbit. The radius of the cyclotron orbit becomes quantized due to the

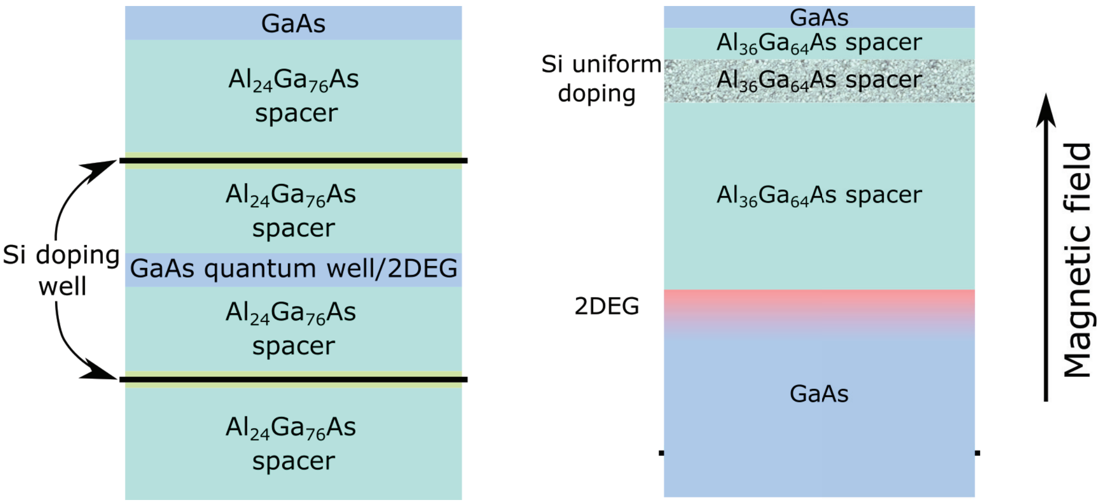

Figure 1.1. Two types of heterostructures of GaAs (blue), AlGaAs (cyan) and AlAs (green) materials (see Figs. 7 and 6 respectively in [25]). The 2-dimensional electron gas (2DEG) is in GaAs, in a quantum well sandwiched between two AlGaAs layers in the left figure, and at the interface of a AlGaAs layer in the right figure. The magnetic field is applied perpendicular to the 2DEG.

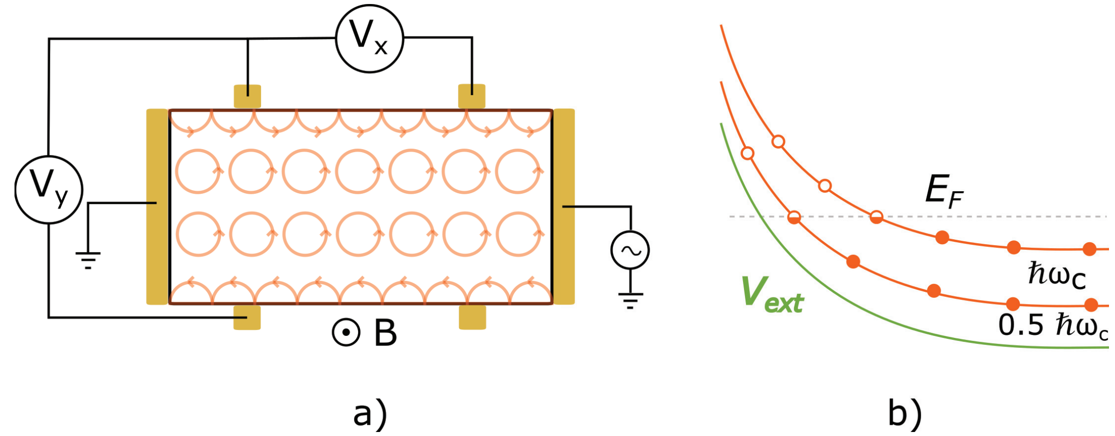

Figure 1.2. a) Cyclotron orbits of electrons in a 2-dimensional electron gas (2DEG) with a perpendicular magnetic field. The cyclotron orbits are cut-off at the edges due to an electric field, because of which the electrons propagate at the edges. Contacts are added as shown using gold (shaded) regions to make a Hall bar. b) Energy as a function of position at the edge. The confinement at the edges due to an external potential V_{ext} raises the LLs (orange) such that they intersect with the Fermi energy level E_F (gray dashed line) creating edge states (half-filled dots).

interference of the electron wavefunction as the electrons are confined to a plane. The quantized cyclotron orbits form Landau levels (LLs) in energy, which resemble the energy levels of a quantum harmonic oscillator:

$$E_n = (n + \frac{1}{2})\hbar\omega_c;\ \omega_c = \frac{eB}{m^*};\ n = 0, 1, 2, ... \tag{1.1}$$

Here m^* is the effective mass, e is the charge of electrons in the GaAs crystal, and B is the external magnetic field. Electrons start moving along the edges of the 2DEG due to the edge electric field (see Fig. 1.2b) known as $E \times B$ drift, which can also be thought of as electrons in cyclotron orbits bouncing off a wall (see Fig. 1.2a). Forward and backward propagating electrons are located on the opposite ends of the 2DEG (Fig. 1.2a).

A small AC current source (I nano-Amps) can be connected to the 2DEG, and the longitudinal (V_x) and transverse (V_y) potential differences across the 2DEG can be measured using a Hall bar geometry (see Fig. 1.2a). The electric field at the edges that leads to the electron drift is independent of the voltage of the AC current source. In the quantum Hall effect, the longitudinal resistivity ($\propto V_x/I$) and conductivity ($\propto I/V_x$) become zero when the Fermi level lies in between LLs away from the edges (see Fig. 1 of [26]). The longitudinal resistivity is zero as forward moving electrons cannot scatter to the backward moving edge, which is located at the other side of the Hall bar. The conductivity is zero as the amount of current I doesn't depend on the applied voltage V_x (as the edge electric field is independent of V_x for small V_x).

The transverse/Hall resistivity/resistance (V_y/I) shows more interesting properties. The Hall resistivity vs magnetic field has plateaus with the resistivity exactly $\hbar/ie^2$, where $i = 1, 2, 3, ...$ is the number of completely filled LLs (see Fig. 1 of [26]). The index i changes with the external magnetic field as the splitting between the LLs is dependent on the external magnetic field (eq. 1.1). The Hall resistivity forms plateaus, because exactly 1 electron per LL is transfered from the bottom edge to the top edge or vice-versa when current is flowing, as the cyclotron orbits are truncated at the edges. Therefore, plateaus in the Hall resistivity are characteristic of the LLs, each of which transfers a quantized amount of charge in the cross-section of the Hall bar.

Bulk Filling factor

The bulk filling factor is defined as the number of occupied LLs away from the edges. Here the notation n_{bulk} is used for LLs containing both electron spins and ν_{bulk} is used for LLs containing one of the spins. The filling factors can then be written as

$$\nu_{\text{bulk}} = \frac{N}{BA/\phi_0} = \frac{\sigma h}{eB};\ n_{\text{bulk}} = \frac{N}{BA/(\phi_0/2)} = \frac{\sigma h}{2eB} \tag{1.2}$$

where N is the total number of electrons in an area A with a perpendicular magnetic field B, BA is the total magnetic flux, $\phi_0 = h/e$ is the flux quantum, and σ is the number of electrons per unit area (N/A) also called the sheet density. A flux quantum is the amount of flux that an electron wavefunction needs to enclose to acquire a 2π phase-shift. Thus, each cyclotron orbit encloses a ϕ_0 amount of flux. Each spin-ful LL has $\frac{B}{\phi_0}$ available states per unit area.

Fractional Quantum Hall Effect (FQHE)

The FQHE reveals the even more interesting physics of a system made up of thousands of strongly interacting electrons. In FQHE, the Hall resistance has plateaus at fractional filling factors for example $\nu_{\text{bulk}} = \frac{3}{7}, \frac{2}{5}, \frac{1}{3}, \frac{1}{5}, ...$ (see Fig. 1 of [27]). Plateaus at fractional filling indicate that a fractional charge is transferred in the Hall bar cross-section. This cannot be explained using LLs formed by electrons, as each of them can only transfer 1 electron in the Hall bar cross-section and not a fraction of an electron.

Another interesting observation to be made is that the longitudinal resistivity is constant and finite, and Hall resistivity is linear as a function of the magnetic field at $\nu_{\text{bulk}} = \frac{1}{2}$ (see Fig. 1 of [27]). This is very similar to the Hall effect at very low magnetic fields (see left edge of Fig. 1 of [27]). It was first pointed out by Laughlin that the uniform sheet density many body ground state at $\nu_{\text{bulk}} = \frac{1}{2p+1},\ p = 1, 2, ...$ ($2p + 1$ flux quanta per electron) consists of electrons bound to $2p$ flux quanta [28]. Therefore, at $\nu_{\text{bulk}} = \frac{1}{2}$ filling, the electrons bound to 2 flux quanta would form a Fermi sea with 0 effective magnetic field. The many body ground state is highly degenerate with fractionally charged excitations having $\frac{e}{2p+1}$ charge. This would explain the plateaus at $\nu_{\text{bulk}} = \frac{1}{3}, \frac{1}{5}, \frac{1}{7}, ...$, but not other filling fractions such as $\nu_{\text{bulk}} = \frac{3}{7}, \frac{2}{5}, ...$

Plateaus at $\nu_{\text{bulk}} = \frac{3}{7}, \frac{2}{5}, ...$ were explained by Jain in his composite Fermion (CF) picture [29]. In this picture, an electron bound to $2p$ flux quanta, called ^{2p}CF (which is the Laughlin ground state) behaves as a quasiparticle. At $\nu_{\text{bulk}} = \frac{1}{3}$, the ^{2}CF would take up 2 flux quanta per electron, leaving an effective magnetic field B^* with 1 flux quantum per ^{2}CF. As a ^{2}CF goes around one flux quantum, it would gain a phase of 2π giving a constructive interference. Therefore in this situation, an electron would be effectively going around $2p + 1 = 3$ flux quanta, with $1/(2p + 1)^{th} = 1/3^{rd}$ of its orbit truncated at the edges, leading to the transfer of $1/(2p+1)^{th} = 1/3^{rd}$ ^{2}CF and a charge $\frac{e}{2p+1} = \frac{e}{3}$ across the Hall bar cross-section when current is flowing. Therefore, the plateau at $\nu_{\text{bulk}} = \frac{1}{3}$ would be the first LL of ^{2}CF, also known as a Λ level [30]. We have the case of 2 ^{2}CFs per flux quantum for $\frac{5}{2} = 2 + \frac{1}{2}$ flux quanta per electron, and in general $\pm\nu^*$ ^{2p}CFs per flux quantum for $2p \pm \frac{1}{\nu^*}$ flux quanta per electron, where the $-$ sign indicates a reversal of the effective magnetic field with respect to the external magnetic field. Then, a filling fraction $\nu_{\text{bulk}} = 1/\ \ 2p \pm \frac{1}{\nu^*}\ \ = \frac{\nu^*}{2p\nu^* \pm 1}$ would have ν^* filled Λ levels which would transfer $\frac{1}{2p\nu^* \pm 1}^{\text{th}}$ of ^{2p}CFs per Λ level to give a total charge transfer of $\frac{e\nu^*}{2p\nu^* + 1}$ across the Hall bar due to truncated cyclotron orbits when current is flowing.

It is worthwhile to note the various energy scales in FQHE for GaAs (Chap. 5 of [31]). Splitting between the LLs is $\hbar\omega_c \approx 1.723$ meV/T, Coulomb interaction between electrons is $\frac{e^2}{\ } \approx 4.3$ meV/T$^{1/2}$ where   is the dielectric constant and $= 25$ nm/T$^{1/2}$ is the magnetic length, and Zeeman splitting is 2.5 μeV/T. For very large magnetic fields, the LL and Zeeman splittings are much larger than the Coulomb interactions.

Coulomb interactions between electrons in a single LL lead to the formation of many body ground states. The splitting between Λ levels is

$$\Delta = \hbar\omega_c^* = \hbar\left(eB^*\right)/m_{\mathrm{CF}} \tag{1.3}$$

where m_{CF} is the CF effective mass (not equal to the electron effective mass), which can be deduced from the temperature dependence of Shubnikov-de Hass oscillations [32], and B^* is the CF effective magnetic field that remains after $2p$ flux quanta per electron have been removed. The concept of m_{CF} can be a bit misleading as it strongly depends on the interactions between the CFs [33].

Most of the FQHE plateaus occur at filling fractions $\nu_{\mathrm{bulk}} = \frac{\nu^*}{2p\nu^* \pm 1}$. Yet, there are some more plateaus e.g. at $\nu_{\mathrm{bulk}} = \frac{5}{2}, \frac{12}{5}, \ldots$ that do not fall in this category. The ground states at these fractions are believed to be many-body states of CFs, i.e. FQHE of CFs [30]. The $\nu_{\mathrm{bulk}} = \frac{5}{2}$ is theorized to have a CF sea at $\nu = \frac{1}{2}$ filling factor in the $n = 2$ LL with a background of fully filled $n = 1$ LL leading to a paired p-wave state [34]. This state would have non-Abelian $e/4$ charge quasiparticles that would be required by a FQHE based quantum computer [20]. The lifetime of quasiparticles in the 5/2 state depends on the excitation gap Δ, which in turn is highly dependent on the electron density and quality of the sample [35].

Quantum Point Contacts (QPCs)

Electrons or quasiparticles traveling along the lateral edges of the 2DEG in a Hall bar can be brought together using quantum point contacts (QPCs) [36]. QPCs are made up of two metallic top gates that act as Schottky contacts. A negative bias is applied to the QPC gates, which deplete the 2DEG underneath and creates edges under them. The confining potential at the edges under the QPC gates is highly dependent on the heterostructure and gate geometry. For example, gates placed closer to the 2DEG in etched trenches create a sharper edge than gates placed away

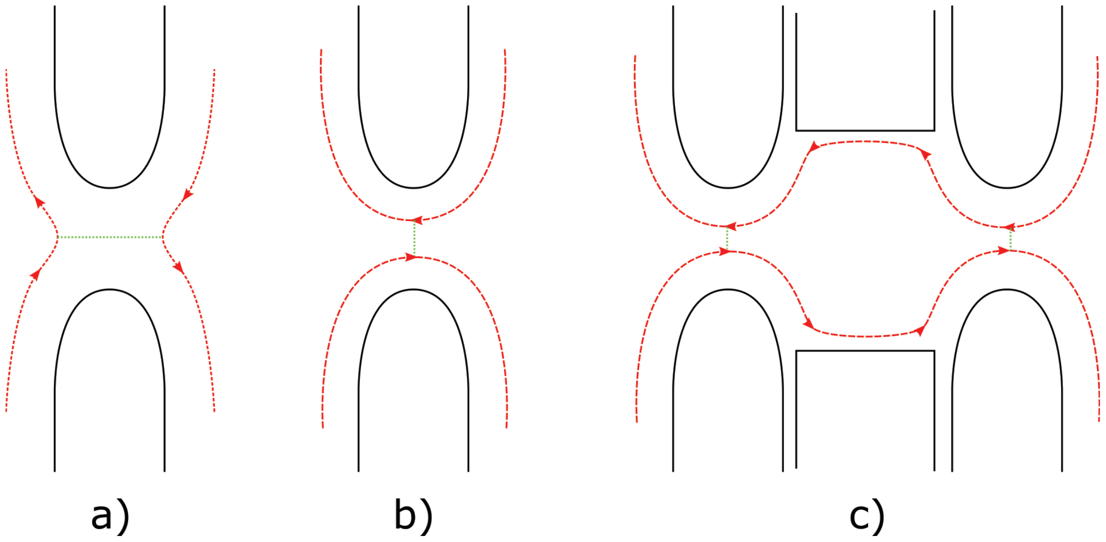

Figure 1.3. Schematics of the top gates and 2DEG edges of a) a QPC in the strong back-scattering regime, b) weak back-scattering regime and c) a Fabry-Pérot interferometer. The red dashed lines with arrows indicate propagating electrons/quasi-particles along the 2DEG edges. The green dotted lines indicate tunneling across the edges.

from the 2DEG on top of the heterostructure. The edge potential created by different gate geometries is discussed in Chapter 3.

The QPCs create a constriction in the 2DEG, which has quantized transverse modes through which electrons can propagate, leading to a step-like resistance or conductance as a function of the voltage on the QPC gates [37]. If a QPC has strong backscattering, the edge states cannot pass through the QPC, and the sheet density in the middle of the QPC is smaller than the rest of the 2DEG (Fig. 1.3a). In this case, the electrons tunnel through the QPC from one side of the QPC to the other, perpendicular to the gates as shown using a dotted green line in 1.3a). If a QPC has weak backscattering (large transmission, or less confinement), edge states can go through it and electrons can tunnel from one edge close to one QPC gate, to the other edge close to the other gate (Fig. 1.3b). Each LL has an edge state, and it is possible that while the edge of the energetically highest filled LL doesn't pass through the QPC, the lowest filled LL edges goes through.

Quantum Hall Interferometery

Interferometers are made using 2 QPCs with transmission probabilities t_1 and t_2 to create a puddle of 2DEG in between. As the electrons travel along the edge of the 2DEG puddle, they enclose magnetic flux and acquire an Aharonov-Bohm (AB) phase. When the acquired phase is $(2n+1)\pi$ $(n = 0, 1, 2, ...)$, circulating electrons undergo destructive interference, and when it's $2n\pi$ $(n = 1, 2, 3, ...)$ there is constructive interference. The acquired phase can be varied by changing either the area enclosed by the paths, which can be controlled by a plunger top gate, or by changing the external magnetic field. The measured current at an ohmic contact collecting the electrons reflected or transmitted from the QPCs then shows an oscillatory behavior (Aharonov-Bohm effect) as a function of plunger gate voltage and magnetic field.

Two types of interferometers are possible: Mach-Zehnder interferometer (MZI) and Fabry-Pérot interferometer (FPI). In MZI (see Fig. 1 of [38]), the first QPC splits the incoming edge states along a reflected path and a transmitted path. These 2 paths interfere at the second QPC, for which the reflected and transmitted currents are complementary and can be separately measured. In FPI [39] (Fig. 1.3 c), the transmitted path through the first QPC enters a 2DEG puddle enclosed by the 2 QPCs. This path circulates the enclosed 2DEG by continuously reflecting off of the 2 QPCs. Interference oscillations are observed in the path transmitted through the second QPC.

The main difference between FPI and MZI is the presence of Coulomb-dominated (CD) oscillations in FPI [40], which are absent in MZI. CD oscillations in the conductance vs the magnetic field and plunger gate voltage happen as the enclosed 2DEG area in the FPI oscillates a function of the enclosed magnetic flux. This is due to electron repulsions as the 2DEG tries to enclose an integer multiple of flux quantums in the FPI. In the CD regime, the conductance plateaus show an opposite slope as the AB regime with magnetic field and plunger gate voltage. In MZI, the CD oscillations are not observed due to the presence of an Ohmic contact which can exchange electrons with the 2DEG puddle between the QPCs.

In both types of interferometers the interfering particles have to travel long distances ($\sim$ 1-10 microns) between the QPCs. To observe a strong interference pattern, the particles must maintain coherence while they go around the interferometer. This can be achieved by engineering devices that support high velocity particles at the 2DEG edges, or by reducing the device size.

Physics at the edge

The velocity of the particles traveling along the edge depends on the local electric and magnetic fields. The classical drift velocity of charged particles in electric and magnetic fields is

$$\mathbf{v} = \frac{\mathbf{E} \times \mathbf{B}}{B^2} \tag{1.4}$$

The electric field at the edge depends on the charge environment in the device, repulsion between electrons and the density of states (DOS). Application of magnetic field creates LLs which have a high DOS confined to a small energy range. Due to this DOS structure, the edge potential and density change in steps as compared to a smooth variation when the magnetic field is absent.

Fig. 1.4 illustrates the effect of electron interaction on the density and potential, which leads to the creation of compressible (metallic) and incompressible (insulating) regions at the edge [41, 42]. Thus, the electric field at the edge varies non-intuitively and needs to be solved computationally to get an accurate electron velocity for a given structure. This is addressed in Chapter 3.

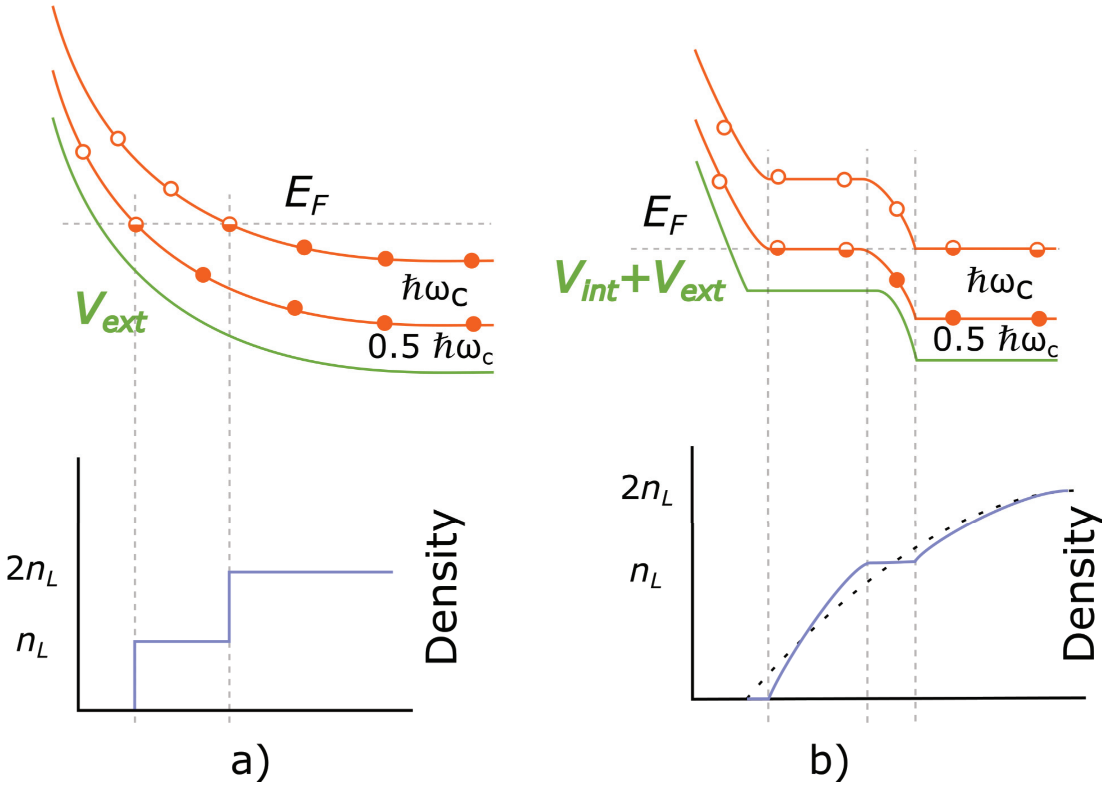

Figure 1.4. Comparison between density and potential at the edge with and without electron interactions. a) For a smooth edge potential, the density at the edge has sharp steps as each LL has high DOS, all of which escapes the Fermi level at a single spatial point. b) When electron interactions are turned on, the Fermi level gets pinned to a LL causing a more energetically favorable smooth density variation. The edge has compressible (metallic) regions where the density changes smoothly and the potential changes very slowly, and incompressible (insulating) regions where the density is constant and potential varies faster.

FQHE based quantum computer

One 5/2 FQHE quasiparticle-based qubit [24] is made up of two Fabry-Pérot interferometers sharing a QPC, so a total of 3 QPCs (see Fig. 2 of [24]). An anti-dot (a potential hill [43] as opposed to a dot which is a potential depression) is placed in the center of each interferometer using depletion top gates connected by a bridge [39]. The qubit is initialized by putting a charge $e/2$ (2 quasiparticles) on the anti-dots, which either have a neutral (Majorana) Fermion on them after initialization or do not (there is no superposition as quasiparticles are measured by the 2DEG). The transmission of the 2 interferometers is dependent on whether a neutral (Majorana) Fermion is present (state |0) or absent (state |1) on the anti-dots. A NOT gate is constructed by a series of QPC gate voltage variations which will finally transfer a quasiparticle from one anti-dot to the other. This system doesn't support universal computing since an arbitrary superposition of |0 and |1 is not possible.

1.2.2 Si/SiO$_2$ based electron spin qubits

Quantum information can also be stored and processed spatially using a small number of electrons, instead of topologically in the 2DEG state. Electron spin qubits encode quantum information using the electron spin in a magnetic field, which creates 2 states energetically separated by the Zeeman splitting. Single electrons can be trapped and manipulated at Si/SiGe [44,45], GaAs/AlGaAs [46–48] and Si/SiO$_2$ [15] interfaces, dopant atoms e.g. phosphorus in silicon [49] etc. Si/SiO$_2$ based spin qubits are particularly promising due to their highly developed processing technology, comparatively longer coherence times, and potential for scalability [10,11]. In this section, details of the quantum dot based electron spin qubit in Si/SiO$_2$ heterostructure are discussed, after which the electrostatic simulations for these devices are motivated.

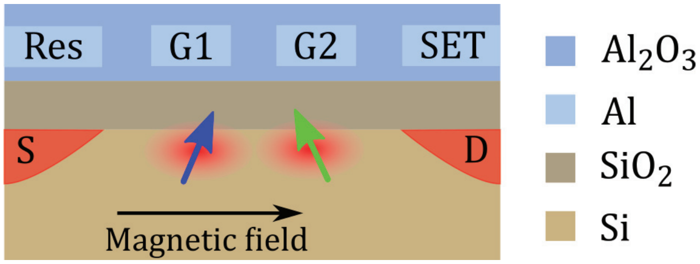

Figure 1.5. An illustration of 2 qubits made from the spins of electrons trapped at the interface of silicon and silicon-dioxide materials under Aluminum gates with an applied positive voltage. The arrows represent electron spins.

Device geometry

One qubit is made by trapping a single Si conduction band electron in a quantum dot [15]. The quantum dot ($\sim$ 30 nm diameter) is made electrostatically at the interface of silicon and silicon-dioxide materials by using a top accumulation gate e.g. “G1” or “G2” as shown in Fig. 1.5. The accumulation gate is made using Al deposited on top of SiO_2 and Al_2O_3 with an applied positive gate voltage. The SiO_2 and Al_2O_3 oxide thicknesses under the gates are around 5.9 nm and 1 nm respectively. A bath of electrons (the source or “S” in Fig. 1.5) is made close to the quantum dots using a reservoir gate “Res” in Fig. 1.5). Electrons with up or down spins can be selectively loaded in the quantum dots by adjusting the energy levels in the dots using the top gates, with respect to the reservoir [50]. A single electron transistor gate (“SET” in Fig. 1.5) that creates the drain electron bath (“D” in Fig. 1.5) is used to measure the electron spins in the dots. Both the loading of electrons and measurement of the spin is based on the concept of Coulomb blockade [51].

Energy scales in a Si/SiO_2 quantum dot

The gap between Si conduction and valence bands, also called the band gap, is $\sim$ 1.17 eV at mili-Kelvin temperatures (Chap. 8 of [52]). The lowest energy conduction band electrons in Si occupy a valley between Γ and X symmetry points, and close to the X symmetry point in the band structure. This valley is 6-fold degenerate with components along x+, x-, y+, y-, z+ and z- axes. The constant energy surface in this valley is an ellipsoid with the long-axis aligned with the symmetry direction of that valley.

At the Si/SiO_2 interface, the crystal inversion symmetry of Si is broken and an electric field is present due to the top gates and accumulation of charge. The inversion symmetry breaking lifts the 6-fold valley degeneracy and lowers the energy of z+/- valleys with respect to x+/- and y+/- valleys if the interface is perpendicular to the z-axis (Fig. 7 of [50]). The electric field further splits z+/- valleys by a splitting that was measured to be around 0.3-0.8 meV [53], while the numerically calculated values are in the range 1.6-2.1 meV [53] for interface electric fields in the range 26.5-30 MV/m.

For 2 electrons in neighboring quantum dots as shown in Fig. 1.5, the Coulomb repulsion between the electrons is $\sim$ 4.5 meV. More electrons are energetically forbidden from occupying the dots due to the Coulomb repulsion. The exchange interaction or Pauli repulsion between the electrons is ~ 4 μeV. The exchange interaction is due to the indistinguishability of electrons and an anti-symmetry in the wavefunction of 2 electrons under exchange. Both the Coulomb repulsion and exchange interaction between the electrons in the 2 dots is highly dependent on the separation in the energy levels of the 2 dots considered separately, also known as detuning. This property is used in the qubit architecture and is discussed in the following sections.

The up and down electron spins are energetically separated by the Zeeman splitting ($E_Z = g\mu_B B$, where $g \sim 1.998$ is the electron g-factor in Si, μ_B is the Bohr magneton and B is the magnetic field). The Zeeman splitting is around 160 μeV for a magnetic field of 1.4 Tesla, which is much larger than the thermal energy at 50 mili-Kelvin temperature (0.43 μeV). Therefore, the spin qubit maintains its state longer in mili-Kelvin temperatures than at higher temperatures as the higher energy spin decays to the lower energy spin by releasing a phonon (lattice vibration).

Eigenstates of the double quantum dot

The number of electrons in the 2 quantum dots can be controlled by adjusting the energy levels using top gates. Electrons entering or exiting the dots can be detected by a change in the current through the SET. A plot of the derivative of SET current vs the voltages on gates G1 and G2 (stability plot) shows diamond shaped regions with a constant number of electrons, known as Coulomb diamonds (Fig. 1c of [16]). The electron spin qubits are formed in the region of the stability plots having a total of 2 electrons. Three configurations: (2,0), (1,1) and (0,2) are possible, where the notation $(n_1,\, n_2)$ is for n_1 electrons in the left dot and n_2 electrons in the right dot.

Each quantum dot behaves like a hydrogen atom with $s, p, d, ...$ orbitals. Two neighboring quantum dots having a wavefunction overlap act as H_2 molecule with controllable on-site energies (detuning). The two s-orbitals in the two dots form bonding ($|\psi_B\rangle$) and anti-bonding ($|\psi_A\rangle$) orbitals due to the wavefunction overlap between the dots

$$|\psi_B\rangle = \frac{1}{\sqrt{2}}\left(|\psi_L\rangle + |\psi_R\rangle\right);\ |\psi_A\rangle = \frac{1}{\sqrt{2}}\left(|\psi_L\rangle - |\psi_R\rangle\right) \tag{1.5}$$

where $|\psi_L\rangle$ and $|\psi_R\rangle$ are the eigenstates of left and right dots respectively. The bonding orbital has a larger probability in the energetically lower dot, whereas the anti-bonding orbital has a larger probability in the higher energy dot. When the two dots are at the same energy (zero detuning), both the bonding and anti-bonding orbitals have equal probabilities in the two dots. Including the electron spins and the two orbitals, a total of 4 one-electron states participate in the low energy spectrum of the double dot: $|\psi_{B\downarrow}\rangle$, $|\psi_{B\uparrow}\rangle$, $|\psi_{A\downarrow}\rangle$ and $|\psi_{A\uparrow}\rangle$.

The two-electron states are constructed from Slater determinants of one-electron states. The Slater determinants satisfy the indistinguishability and exchange anti-symmetry of the wavefunction. The combined spin of the two spin-1/2 electrons follows angular momentum addition rules to give the following 4 states

$$\begin{aligned}
|T_+\rangle &= |\uparrow\rangle_1 |\uparrow\rangle_2\,; && s = 1,\ s_z = 1 \\
|T_0\rangle &= \frac{|\uparrow\rangle_1 |\downarrow\rangle_2 + |\downarrow\rangle_1 |\uparrow\rangle_2}{\sqrt{2}}; && s = 1, s_z = 0 \\
|T_-\rangle &= |\downarrow\rangle_1 |\downarrow\rangle_2\,; && s = 1,\ s_z = -1 \\
|S\rangle &= \frac{|\uparrow\rangle_1 |\downarrow\rangle_2 - |\downarrow\rangle_1 |\uparrow\rangle_2}{\sqrt{2}}; && s = 0,\ s_z = 0
\end{aligned} \tag{1.6}$$

where the subscripts 1 and 2 differentiate between the electrons. The singlet spin state $|S\rangle$ is anti-symmetric under exchange of spins, whereas the triplet spin states $|T_-\rangle$, $|T_0\rangle$ and $|T_+\rangle$ are symmetric. The overall wavefunction of electrons contains both the spatial ($|\psi_B\ $, $|\psi_A\ $) and spin ($|\uparrow\rangle$, $|\downarrow\rangle$) parts. As the overall two-electron wavefunction has to be anti-symmetric under the exchange of electrons, the spatial part of spin singlet is symmetric, whereas that of the spin triplets is anti-symmetric.

The lowest 6 two-electron states that are important in the (2,0)-(1,1)-(0,2) regime [54] can be constructed from the Slater determinants (SD) of the bonding and anti-bonding orbitals as shown here

$$\begin{aligned} |T_+(B,A)\ &= \frac{|\psi_B\ _1|\psi_A\ _2 - |\psi_A\ _1|\psi_B\ _2}{\sqrt{2}} \otimes |\uparrow\ _1|\uparrow\rangle_2 \\ &= \frac{|\psi_{B\uparrow}\ _1|\psi_{A\uparrow}\ _2 - |\psi_{A\uparrow}\ _1|\psi_{B\uparrow}\ _2}{\sqrt{2}} \\ &= \mathrm{SD}\left(|\psi_{B\uparrow}\ , |\psi_{A\uparrow}\ \right) = \mathrm{SD}_{2,4} \end{aligned} \tag{1.7}$$

$$\begin{aligned} |T_-(B,A)\ &= \frac{|\psi_B\ _1|\psi_A\ _2 - |\psi_A\ _1|\psi_B\ _2}{\sqrt{2}} \otimes |\downarrow\ _1|\downarrow\rangle_2 \\ &= \frac{|\psi_{B\downarrow}\ _1|\psi_{A\downarrow}\ _2 - |\psi_{A\downarrow}\ _1|\psi_{B\downarrow}\ _2}{\sqrt{2}} \\ &= \mathrm{SD}\left(|\psi_{B\downarrow}\ , |\psi_{A\downarrow}\ \right) = \mathrm{SD}_{1,3} \end{aligned} \tag{1.8}$$

$$\begin{aligned} |T_0(B,A)\ &= \frac{|\psi_B\ _1|\psi_A\ _2 - |\psi_A\ _1|\psi_B\ _2}{\sqrt{2}} \otimes \frac{|\uparrow\rangle_1|\downarrow\rangle_2 + |\downarrow\rangle_1|\uparrow\rangle_2}{\sqrt{2}} \\ &= \frac{1}{\sqrt{2}}\quad \frac{|\psi_{B\uparrow}\ _1|\psi_{A\downarrow}\ _2 - |\psi_{A\downarrow}\ _1|\psi_{B\uparrow}\ _2}{\sqrt{2}} + \frac{|\psi_{B\downarrow}\ _1|\psi_{A\uparrow}\ _2 - |\psi_{A\uparrow}\ _1|\psi_{B\downarrow}\ _2}{\sqrt{2}} \\ &= \frac{\mathrm{SD}\left(|\psi_{B\uparrow}\ , |\psi_{A\downarrow}\ \right) + \mathrm{SD}\left(|\psi_{B\downarrow}\ , |\psi_{A\uparrow}\ \right)}{\sqrt{2}} = \frac{\mathrm{SD}_{2,3} + \mathrm{SD}_{1,4}}{\sqrt{2}} \end{aligned} \tag{1.9}$$

$$\begin{aligned} |S(B,B)\ &= |\psi_B\ _1|\psi_B\ _2 \otimes \frac{|\uparrow\rangle_1|\downarrow\rangle_2 - |\downarrow\ _1|\uparrow\rangle_2}{\sqrt{2}} \\ &= \frac{|\psi_{B\uparrow}\ _1|\psi_{B\downarrow}\ _2 - |\psi_{B\downarrow}\ _1|\psi_{B\uparrow}\ _2}{\sqrt{2}} \\ &= \mathrm{SD}\left(|\psi_{B\uparrow}\ , |\psi_{B\downarrow}\ \right) = \mathrm{SD}_{1,2} \end{aligned} \tag{1.10}$$

$$\begin{aligned} |S(A,A) &= |\psi_A\ _1|\psi_A\ _2 \otimes \frac{|\uparrow\rangle_1 |\downarrow\rangle_2 - |\downarrow\ _1 |\uparrow\rangle_2}{\sqrt{2}} \\ &= \frac{|\psi_{A\uparrow}\ _1 |\psi_{A\downarrow}\ _2 - |\psi_{A\downarrow}\ _1 |\psi_{A\uparrow}\ _2}{\sqrt{2}} \\ &= \mathrm{SD}\left(|\psi_{A\uparrow}\ , |\psi_{A\downarrow}\ \right) = \mathrm{SD}_{3,4} \end{aligned} \tag{1.11}$$

$$\begin{aligned} |S(B,A) &= \frac{|\psi_B\ _1|\psi_A\ _2 + |\psi_A\ _1|\psi_B\ _2}{\sqrt{2}} \otimes \frac{|\uparrow\rangle_1 |\downarrow\rangle_2 - |\downarrow\ _1 |\uparrow\rangle_2}{\sqrt{2}} \\ &= \frac{1}{\sqrt{2}} \quad \frac{|\psi_{B\uparrow}\ _1 |\psi_{A\downarrow}\ _2 - |\psi_{A\downarrow}\ _1 |\psi_{B\uparrow}\ _2}{\sqrt{2}} - \frac{|\psi_{B\downarrow}\ _1 |\psi_{A\uparrow}\ _2 - |\psi_{A\uparrow}\ _1 |\psi_{B\downarrow}\ _2}{\sqrt{2}} \\ &= \frac{\mathrm{SD}\left(|\psi_{B\uparrow}\ , |\psi_{A\downarrow}\ \right) - \mathrm{SD}\left(|\psi_{B\downarrow}\ , |\psi_{A\uparrow}\ \right)}{\sqrt{2}} = \frac{\mathrm{SD}_{2,3} - \mathrm{SD}_{1,4}}{\sqrt{2}} \end{aligned} \tag{1.12}$$

Energy spectrum of the double quantum dot

The Hamiltonian of a double quantum dot containing 2 electrons can be written in the effective mass approximation as follows

$$H = \frac{1}{2m^*} \quad \mathbf{p}_1 + \frac{e}{c}\mathbf{A} \quad ^2 + \quad \mathbf{p}_2 + \frac{e}{c}\mathbf{A} \quad ^2 \quad + V + \frac{e^2}{4\pi\epsilon\,|\mathbf{r}_1 - \mathbf{r}_2|} + H_Z + H_{SO} + H_{nuc}\,. \tag{1.13}$$

Here the first two terms are the kinetic energy terms of the two electrons containing the vector potential $\mathbf{A}$ due to the magnetic field, V is the electrostatic potential of the double dot, next term is the Coulomb interaction between electrons, H_Z is the Zeeman splitting, H_{SO} is the spin-orbit coupling due to the interface, and H_{nuc} is the hyperfine interaction due to Si^{29} nuclei that introduce an anisortopy in the magnetic field. This Hamiltonian can be solved using various methods such as Hartree-Fock [55], molecular orbital [55], Heitler-London [56, 57], Hund-Mulliken [57, 58], truncated basis [54], full configuration interaction [59] etc.

All of these methods use a single electron basis as a starting point. Various approximations to the double-dot potential such as quadratic with quartic terms have been used for analytically calculating the single electron basis states. Here, a

Hubbard model is provided that gives an overall picture of the single electron energy spectrum. Each dot is treated as an atom tightly confining an electron. The tightly bound wavefunctions of an electron in a dot ($|\psi_L\ \ , |\psi_R\ $) can be calculated by solving the one-electron one-dot Hamiltonians

$$H_L = \frac{p^2}{2m^*} + V_L,\ \ H_R = \frac{p^2}{2m^*} + V_R \tag{1.14}$$

where V_L and V_R are the electrostatic potentials of the left and right dot such that $V = V_L + V_R$. Here the magnetic field is set to 0 and the spin-orbit coupling is neglected for simplicity. The double dot Hubbard Hamiltonian in the basis of $|\psi_L$ and $|\psi_R$ can then be written as

$$H_{Hub}\,|\psi_{Hub}\ \ = \begin{pmatrix} \varepsilon/2 & t \\ t & -\varepsilon/2 \end{pmatrix} \begin{pmatrix} \psi_L \\ \psi_R \end{pmatrix} \Bigg\{ t = \ \ \psi_{L/R}\,|H_{LR}|\,\psi_{R/L}\ \ ;\ H_{LR} = \frac{p^2}{2m^*} + V \tag{1.15}$$

where ε is the detuning and t is the hopping term between the dots. The eigenvalues of this Hamiltonian are

$$E_{A/B} = \pm\ \ \overline{\varepsilon^2/4 + t^2}, \tag{1.16}$$

and the wavefunctions are the bonding and anti-bonding orbitals as shown in Eq. 1.5. These energy levels, including spin splitting due to magnetic field are plotted in Fig. 1.6a. The splitting between the bonding and anti-bonding orbitals at $\varepsilon = 0$ is the orbital splitting, $E_{orb} = 2t$. The orbital splitting is $\sim 0.3 - 1.0$ meV in Si/SiO$_2$ double quantum dots.

Neglecting the vector potential, spin-orbit coupling and hyperfine interaction for simplicity, we can write down the two-electron Hamiltonian using Eq. 1.13.

$$H = \frac{p_1^2}{2m^*} + \frac{p_2^2}{2m^*} + V + H_Z + \frac{e^2}{4\pi\epsilon\,|\mathbf{r}_1 - \mathbf{r}_2|} \tag{1.17}$$

The two electron Hamiltonian can then be constructed in the basis

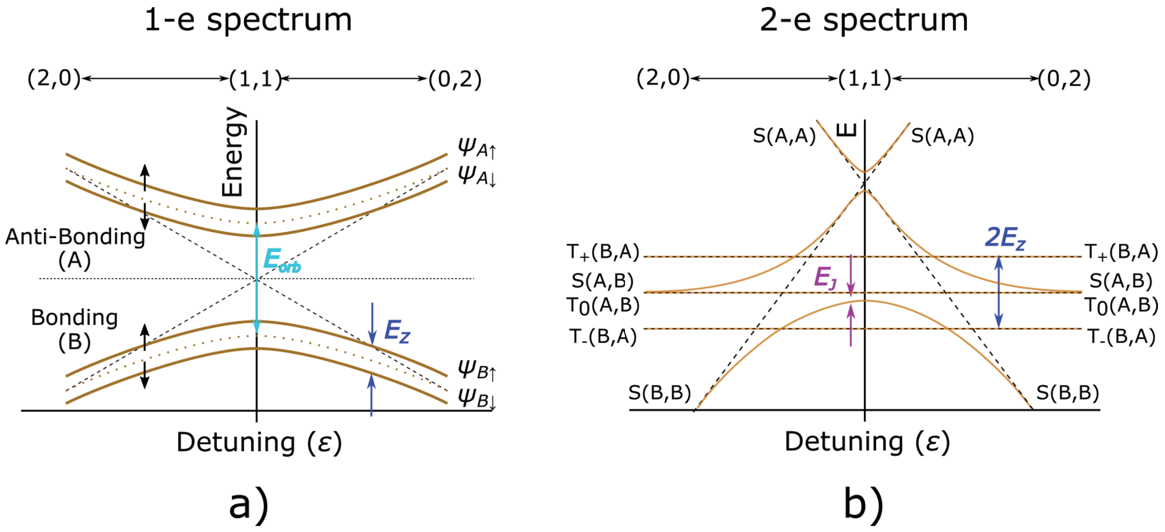

Figure 1.6. An illustration of the one and two electron energy spectrums in a double quantum dot vs detuning for a total of 2 electrons in the dots. a) One-electron energy spectrum shows the bonding and anti-bonding orbitals with spin energy levels separated by Zeeman splitting. The dashed lines show energy levels of $|\psi_L$ and $|\psi_R$ in left and right dots respectively at zero magnetic field. b) Two-electron energy spectrum shows the singlet and triplet states in the bonding and anti-bonding orbitals. The $|S(A,A)$, $|S(B,A)$ and $|S(B,B)$ states interact at low detuning to give four anti-crossings symmetrically located around zero detuning. The dashed lines show the behavior of energy levels when the off-diagonal singlet terms are turned off by uncoupling the dots. E_J is the exchange coupling between the $|T_0(B,A)$ and $|S(1,1)$ states.

$$\Psi = \begin{pmatrix} |S(A,A) \\ |S(B,B) \\ |S(B,A) \\ |T_+(B,A) \\ |T_0(B,A) \\ |T_-(B,A) \end{pmatrix} \Bigg\{ \qquad (1.18)$$

giving us

$$H = \begin{pmatrix} U_A + 2E_A & X & \sqrt{2}T_A & & H_{SO} & \\ X & U_B + 2E_B & \sqrt{2}T_B & & & \\ \sqrt{2}T_A & \sqrt{2}T_B & V_+ & & H_{nuc} & \\ & & & V_- + E_Z & & \\ & H_{SO} & H_{nuc} & & V_- & \\ & & & & & V_- - E_Z \end{pmatrix} \tag{1.19}$$

Where

$$U_{A/B} = \quad \psi^\dagger_{A/B}(\mathbf{r}_1)\psi^\dagger_{A/B}(\mathbf{r}_2)\frac{e^2}{4\pi\epsilon\,|\mathbf{r}_1 - \mathbf{r}_2|}\psi_{A/B}(\mathbf{r}_1)\psi_{A/B}(\mathbf{r}_2)\,d\mathbf{r}_1\,d\mathbf{r}_2 \tag{1.20}$$

are the Coulomb interaction terms when both electrons are in bonding/anti-bonding orbitals,

$$X = \quad \psi^\dagger_{A}(\mathbf{r}_1)\psi^\dagger_{A}(\mathbf{r}_2)\frac{e^2}{4\pi\epsilon\,|\mathbf{r}_1 - \mathbf{r}_2|}\psi_{B}(\mathbf{r}_1)\psi_{B}(\mathbf{r}_2)\,d\mathbf{r}_1\,d\mathbf{r}_2 \tag{1.21}$$

is the two-electron hopping term between the $|S(A, A)$ and $|S(B, B)$ states,

$$T_{A/B} = \quad \psi^\dagger_{A/B}(\mathbf{r}_1)\psi^\dagger_{A/B}(\mathbf{r}_2)\frac{e^2}{4\pi\epsilon\,|\mathbf{r}_1 - \mathbf{r}_2|}\psi_{A}(\mathbf{r}_1)\psi_{B}(\mathbf{r}_2)\,d\mathbf{r}_1\,d\mathbf{r}_2 \tag{1.22}$$

are the tunnel coupling terms between $|S(B, A)$ and $|S(A, A)$ or $|S(B, B)$, and $V_\pm = J_{AB} \pm K_{AB}$ are the on-site energies of $|S(B, A)$ and $|T_0(B, A)$ states respectively where

$$\begin{aligned} J_{AB} &= \quad \psi^\dagger_{A}(\mathbf{r}_1)\psi^\dagger_{B}(\mathbf{r}_2)\frac{e^2}{4\pi\epsilon\,|\mathbf{r}_1 - \mathbf{r}_2|}\psi_{A}(\mathbf{r}_1)\psi_{B}(\mathbf{r}_2)\,d\mathbf{r}_1\,d\mathbf{r}_2\,, \\ K_{AB} &= \quad \psi^\dagger_{A}(\mathbf{r}_1)\psi^\dagger_{B}(\mathbf{r}_2)\frac{e^2}{4\pi\epsilon\,|\mathbf{r}_1 - \mathbf{r}_2|}\psi_{B}(\mathbf{r}_1)\psi_{A}(\mathbf{r}_2)\,d\mathbf{r}_1\,d\mathbf{r}_2 \end{aligned} \tag{1.23}$$

are the Coulomb and exchange terms. $|S(B, A)$ is coupled to the triplet states by hyperfine interaction terms and $|T_0(B, A)$ is coupled to $|S(A, A)$ and $|S(B, B)$ by spin-orbit interaction [54]. This Hamiltonian gives us the two-electron energy spectrum plotted in Fig. 1.6b.

Spin qubit operation

For a single qubit operation, the dots are electrostatically separated such that the hopping (t) and the tunnel coupling ($T_{A/B}$) terms are close to zero. For two qubit operation, the dots are intentionally brought closer to form bonding/anti-bonding orbitals. This could be done with a top gate between the dots to turn on the exchange coupling [11].

A single spin qubit is operated using the phenomenon of Rabi oscillations [15]. Rabi oscillations are induced between spin up ($|1\rangle$) and down ($|0\rangle$) using an oscillating magnetic field. The oscillating magnetic field drives the qubit between $|0\rangle$ and $|1\rangle$ states with a frequency called the Rabi frequency

$$\Omega = \sqrt{(\omega - \omega_0)^2 + \omega_1^2} \tag{1.24}$$

where ω is the magnetic field oscillation frequency, $\hbar\omega_0 = \hbar\gamma B_0$ is the Zeeman splitting with B_0 the constant magnetic field, and $\omega_1 = \gamma B_1$ where B_1 is the amplitude of the oscillating magnetic field. $\gamma = g\mu_B/\hbar$ is the gyromagnetic ratio where g is the g-factor of electrons at the Si interface, which depends on the direction of the constant magnetic field with respect to the crystal and the valley in which the electron resides [60, 61]. An oscillating magnetic field can be induced using an AC current in an electron spin resonance (ESR) line fabricated close to the dots [15], by placing a micro-magnet close to the dots and applying AC voltage to the top gates [62], or by creating a magnetic field gradient in the nuclear spins and applying AC voltage to the top gates [63].

The NOT gate is a $\pi_{x/y}$ gate (rotation about x or y axes on the Bloch sphere) in which the oscillating magnetic field is applied till the spin flips, which causes a $\theta_f - \theta_i = \pi$ rotation on the Bloch sphere. For a $\pi_{x/y}/2$ gate, the duration of oscillating magnetic field is half that of $\pi_{x/y}$ gate. A π_z gate requires the qubit to be adiabatically evolved for half the time period of Larmor precession of the electron spin.

In the CNOT gate demonstration [16], the electrons in the double dot are initialized in the ground singlet state $|S(1,1)$ at zero detuning. $|S(1,1)$ is a combination of $|S(B,B)$ and $|S(A,A)$ states. An AC voltage pulse on one of the qubits drives two types of oscillations: $|S(1,1)\rangle \leftrightarrow |T_+(B,A)$ and $|S(1,1)\rangle \leftrightarrow |T_-(B,A)$. The resonance frequencies of these oscillations are separated by the exchange splitting E_J between the $|S(1,1)$ and $|T_0(B,A)$ (Fig. 1.6b and Fig. 2d of [16])

$$h \;\; \nu_{(S\rightarrow T_+)} - \nu_{(S\rightarrow T_-)} \;\; = E_J \tag{1.25}$$

Therefore, using a frequency $\nu_{(S\rightarrow T_+)}$ microwave pulse on the left dot will drive a spin flip only when the electron in the right dot is spin up. This operates as a CNOT gate.

1.3 Importance of simulations

It was shown in Sec. 1.2.1 that electron/quasi-particle coherence is important for the observation of interference oscillations and the operation of a FQHE based qubit. The coherence length of a particle can be increased either by increasing the coherence time or the velocity. It was discussed that the velocity is directly proportional to the electric field at the edge, and therefore it is important to have heterostructures and gates that support a high edge electric field. Meeting these design specifications purely using experimental tools is time consuming, and previous studies [41,42,64–66] don't offer a clear path towards better designs. It is thus important to develop a modeling tool for GaAs/AlGaAs heterostructures which is geared towards device design.

It was shown in Sec. 1.2.2 that the exchange splitting is an important parameter in the CNOT gate operation. Although analytical and numerical studies [54–59] calculate this using analytical electrostatic potentials for the dots, they don't provide a quantitative picture which is essential for the design. Also, no attempt has yet been made to link the exchange splitting to the device parameters such as gate voltages, gate geometry, oxide thicknesses etc. The electrostatic simulations framework presented here can fill in this gap. Details of the Si/SiO$_2$ quantum dot simulations are presented in Chapter 4.

2. ELECTROSTATIC SIMULATION FRAMEWORK

This chapter describes the low temperature simulations framework for QDs and QPCs. The goal of the framework is to model electrostatics in heterostructures for 2-dimensional (2DEG), 1-dimensional (QPCs) and 0-dimensional (QD) systems at low temperatures. Free charges (e.g. conduction band electrons), fixed charges (e.g. charges on dopant atoms in a crystal) and electric field and voltage of the top gates etc. contribute to the electrostatics as shown in Fig. 2.1. The main challenges are to 1) calculate the minimum energy configuration of the interacting free charges, and 2) tackle large devices containing trillions of atoms. The following sections describe how these two challenges are met. Quantum mechanics plays a major role in the electrostatics as it affects the fixed and free charge densities.

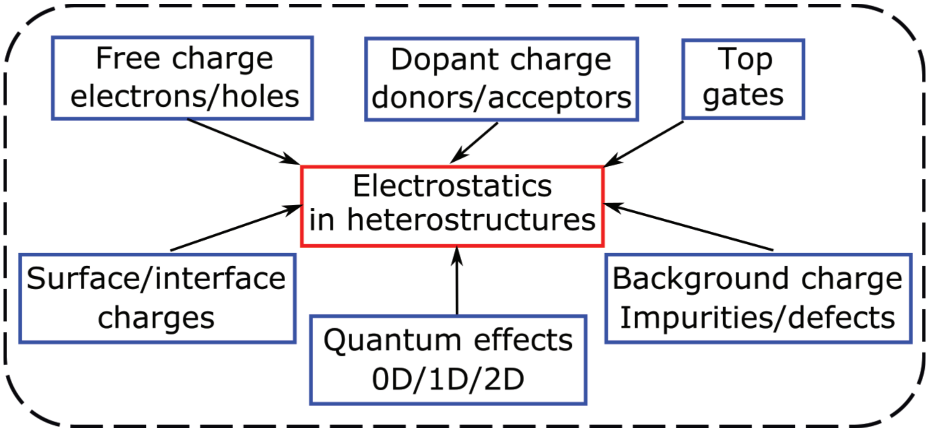

Figure 2.1. An illustration showing the various factors that affect electrostatics in heterostructures.

2.1 Free charges

Free charges in a heterostructure reside in the conduction and valence bands of the materials. Conduction band is made from the outermost shells whereas valence band is made from the inner shells of an atom. A forbidden energy gap between these two bands is present for semiconductors due to the periodicity of potential wells on atoms in a crystal. The dispersion (energy vs momentum) of electrons at the conduction band minimum and valence band maximum is similar to that of a free electron, but with a different curvature that gives rise to an effective mass.

The semiconductor heterostructures used for QDs and QPCs are made up of GaAs, AlGaAs, AlAs and Si materials. QD and QPC devices are several microns in size and can contain trillions of atoms that participate in the electrostatics. Using an atomistic tight binding or density functional theory Hamiltonian in these devices is unnecessary and computationally infeasible. Therefore, a continuum effective mass Schrödinger equation Hamiltonian is used at low temperature and low energy in these materials [67–69]

$$\frac{-\hbar^2}{2m_0}\nabla\cdot \quad \frac{1}{m^*(\mathbf{r})}\cdot\nabla\psi(\mathbf{r}) \quad + \left[E_C + qV(\mathbf{r})\right]\psi(\mathbf{r}) = E\psi(\mathbf{r}) \tag{2.1}$$

where

$$\frac{1}{m^*(\mathbf{r})} = \begin{pmatrix} 1/m_l^*(\mathbf{r}) & & \\ & 1/m_t^*(\mathbf{r}) & \\ \Big\{ & & 1/m_t^*(\mathbf{r}) \end{pmatrix} \Bigg\{ \tag{2.2}$$

the position-dependent effective mass tensor with $m_l^*(\mathbf{r})$ and $m_t^*(\mathbf{r})$ the position dependent longitudinal and transverse effective masses, which describes the curvature of the conduction or valence bands at a valley, E_C is the energy at the conduction band minimum, $q = -e$ is the charge of an electron, V is the electrostatic potential, $\psi(\mathbf{r})$ is the wavefunction and E is the eigen energy.

The free electron charge density n can then be obtained from the eigenfunctions $\psi_i(\mathbf{r})$ and energy eigenvalues E_i as follows

$$
\begin{aligned}
n(\mathbf{r}) &= \underset{i}{\quad} N_i(\mathbf{r})|\psi_i(\mathbf{r})|^2, \\
N_i(\mathbf{r}) &= \begin{cases} \frac{g_v g_s}{1+\exp((E_i-E_F)/kT)}, & 0-D \\ g_v \frac{m_t^*(\mathbf{r})kT}{\pi\hbar^2} \ln \;\; 1+\exp \;\; \frac{E_F-E_i}{kT} \quad , & 1-D \\ g_v \frac{2m_t^*(\mathbf{r})kT}{\pi\hbar^2} \mathcal{F}_{-\frac{1}{2}} \;\; \frac{E_i-E_F}{kT} \quad , & 2-D \end{cases}
\end{aligned}
\tag{2.3}
$$

where $N_i(\mathbf{r})$ is the occupancy of the i^{th} energy level which is expanded for no periodicity (QD), periodicity in 1-dimension (QPC) and 2-dimensions (2DEG) [68], g_v and g_s are the valley and spin degeneracies, $\mathcal{F}_{-\frac{1}{2}}$ is the Fermi integral of order -1/2, E_f is the Fermi level, k is the Boltzmann constant and T is the temperature. Eq. 2.1 is solved in 3, 2 and 1 dimensions for 0-dimensional (QD), 1-dimensional (QPC) and 2-dimensional periodicities respectively.

Charge density can also be obtained semi-classically without solving the Schrödinger equation (Eqs. 2.1 and 2.3). This can be used as an approximate guess of the free charge density. The semi-classical charge density for electrons and holes is obtained by integrating the quantum density of states in a material with 3-dimensional periodicity and is given by

$$
n_{\text{semicl}}(\mathbf{r}) = N_C \mathcal{F}_{\frac{1}{2}} \quad \frac{E_F - E_C(\mathbf{r})}{kT} \quad , N_C = g_s \quad \frac{m_{e,dos}^*(\mathbf{r})kT}{2\pi\hbar^2}^{\frac{3}{2}} \tag{2.4}
$$

$$
p_{\text{semicl}}(\mathbf{r}) = N_V \mathcal{F}_{\frac{1}{2}} \quad \frac{E_V(\mathbf{r}) - E_F}{kT} \quad , N_V = g_s \quad \frac{m_{h,dos}^*(\mathbf{r})kT}{2\pi\hbar^2}^{\frac{3}{2}} \tag{2.5}
$$

where $m_{e,dos}^*(\mathbf{r}) = g_v^{\frac{2}{3}} (m_l^* m_t^*)^{\frac{1}{3}}$ and $m_{h,dos}^*(\mathbf{r})$ are the 3D density of states effective masses of electrons and holes respectively, and $\mathcal{F}_{\frac{1}{2}}$ is the Fermi integral of order 1/2.

Exchange and correlation energy corrections

The free charges have Coulomb and Pauli repulsions between then which can be approximated using density functional theory with a density dependent correction for the exchange and correlation energies. Exchange and correlation energy correction in local density approximation (LDA) [70], which is widely used for semiconductors [68, 71], is given by

$$\begin{aligned} V_{xc}(\mathbf{r}) &= \frac{-q^2}{4\pi^2} \quad 3\pi^2 n(\mathbf{r}) \quad {}^{\frac{1}{3}} \quad 1 + 0.7334x \ln \quad 1 + x^{-1} \qquad , \\ x &= \frac{1}{21} \quad \frac{4\pi n(\mathbf{r}) b^3}{3} \quad {}^{\frac{-1}{3}} \qquad , \\ b &= \frac{4\pi\epsilon\hbar^2}{m^* q^2} \end{aligned} \tag{2.6}$$

This term adds to Eq. 2.1. The effect of the free charge on itself in the mean field is modeled using the Hartree approximation, which involves self-consistently solving Eq. 2.1 with the semiconductor Poisson equation discussed in Sec. 2.5.

2.2 Fixed charges

The sources of fixed charges can be ionized dopant atoms with more (acceptor) or less (donor) electrons than their neutral configuration, and electrons trapped in impurities, crystal defects and dangling bond on the surface. The concentration of ionized donors N_D^+ and acceptors N_A^- is described by the incomplete ionization model [72] given by

$$N_D^+(\mathbf{r}) = N_D \frac{1}{1 + g_D \exp \quad \frac{E_F - E_D(\mathbf{r})}{kT}} = N_D \frac{1}{1 + g_D \exp \quad \frac{E_F - E_C(\mathbf{r}) + E_d}{kT}} \tag{2.7}$$

$$N_A^-(\mathbf{r}) = N_A \frac{1}{1 + g_A \exp \quad \frac{E_A(\mathbf{r}) - E_F}{kT}} = N_A \frac{1}{1 + g_A \exp \quad \frac{E_V(\mathbf{r}) + E_a - E_F}{kT}} \tag{2.8}$$

where N_D and N_A are the actual donor and acceptor concentrations, g_D is the donor level degeneracy (usually $g_D = 2$ because of spin degeneracy) and g_A is the acceptor level degeneracy (usually $g_A = 4$ because of spin and heavy hole - light hole degeneracies), $E_D(\mathbf{r})$ and $E_A(\mathbf{r})$ are the donor and acceptor energy levels, $E_d = E_C(\mathbf{r}) - E_D(\mathbf{r})$

is the donor ionization energy, and $E_a = E_A(\mathbf{r}) - E_V(\mathbf{r})$ is the acceptor ionization energy.

The trap and defect charges are randomly distributed in a crystal with a certain density, and they can be treated as fixed background charges in the continuum model. Surface charges due to dangling bonds act as a Schottky barrier and lead to a pinning of the Fermi in the middle of the band gap [73]. These can be modeled as an electric field at the surface [74], or using complicated models for the surface density of states [75, 76]. In the tool, an electric field is applied at the surface to model the surface states.

2.3 Poisson equation

Electrostatic potential V in Eq. 2.1 is dependent on the charges, gate voltages and electric field at the boundary. V can be calculated by solving the semiconductor Poisson equation given by

$$-\nabla . [\ {}_0\ {}_r(\mathbf{r})\nabla V(\mathbf{r})] = \rho(\mathbf{r}) = \ p(\mathbf{r}) - n(\mathbf{r}) + N_D^+(\mathbf{r}) - N_A^-(\mathbf{r}) \qquad (2.9)$$

where ${}_0$ and ${}_r(\mathbf{r})$ are the permittivity of vacuum and the position-dependent dielectric constant respectively, $n(\mathbf{r})$ and $p(\mathbf{r})$ are electron and hole charge densities defined in Eqs. 2.3, 2.4 and 2.5, $N_D^+(\mathbf{r})$ and $N_A^-(\mathbf{r})$ are concentrations of ionized donors and acceptors defined in Eqs. 2.7 and 2.8 respectively. Self-consistently solving the semiconductor Poisson equation with the Schrödinger equation (Eq. 2.1) is discussed in Sec. 2.5.

2.4 Discretization

The continuum Schrödinger (Eq. 2.1) and Poisson (Eq. 2.9) equations can be solved numerically by discretizing them on a spatial mesh. Finite difference (FD), finite volume (FV) and finite element methods (FEM) are the most widely used discretization methods for semiconductor equations. The biggest differences between these three methods are 1) the definition of a function over the discrete space, 2) the definition of derivatives of the function, and 3) the method of defining boundary conditions.

QD and QPC devices have a complicated gate geometry that requires versatile meshing techniques such as Delaunay triangulation that can accommodate any shape. Also, the electron/hole density at the heterostructure interface lies in a very thin region (2-30 nm) compared to the heterostructure height (50-500 nm), requiring a very finely spaced mesh (< 1 nm spacing) in certain regions. A uniform mesh is unsuitable for such a device, and the implementation of finite difference and volume discretizations over non-uniform meshes can be tedious. FEM supports meshes with the required versatility, and therefore it is used for this tool.

2.4.1 Finite element method

In FEM, a continuous function f is discretized over a mesh using basis functions $\varphi(x)$. This is the Galerkin's method [77]. The discretized function is written as

$$f(x) = \sum_i f_i \varphi_i(x)$$

where f_i is the coefficient of the i^{th} basis function $\varphi_i(x)$. The basis functions are orthonormal functions associated with each point on the mesh. The order of FEM discretization is the largest power of a coordinate in a basis function. There are o basis functions associated with each point for an order o FEM discretization. In this tool, Langrange polynomials are used for constructing the basis functions.

The simulation domain can be discretized into finite elements of different shapes and sizes. The LibMesh library [78] has been utilized for integrating the equations discretized using FEM. LibMesh allows for FEM meshes with 3D mixed elements like tetrahedra, prisms, pyramids and hexahedra. The mesh can be structured, unstructured or have both types of subdomains. This feature of LibMesh has been utilized in this work to reduce the number of vertices without losing accuracy.

Weak form of Schrödinger and Poisson equations

The effective-mass Schrödinger (Eq. 2.1) and semiconductor Poisson (Eq. 2.9) equations are discretized using FEM. The discretization procedure is shown in Appendix A. The discretized equations are written in an integral form called the weak form (Eqs. A.2 and A.4), which can be converted into the matrix form (Eqs. A.3 and A.5) with each row or column of the matrix corresponding to a FEM basis function.

Boundary conditions for Poisson equation

The effect of top gates and surface charges is included in the Poisson equation using boundary conditions as shown in Appendix B. For Schottky contacts, the gate voltage is converted to the electrostatic potential using the difference in metal-semiconductor ionization energy, and applied as a Dirichlet boundary condition as described in Sec. B. Surface charge can be included as a Neumann boundary condition as shown in Sec. B. For Schottky contacts with a charge at the interface, mixed boundary condition is used as shown in Sec. B.

2.4.2 Meshing

The software Gmsh [79] has been used to create both structured, unstructured and mixed finite element method. The FEM mesh is generated to give nanometer resolution in the vertical direction for complicated GaAs/AlGaAs heterostructures, such as the Si doping well [80]. Simple tetrahedral elements, even when refinement is used give a large number of nodes in the mesh (as shown in Fig. 2.2b) which increases the computational resources required for the problem. The reason for this is that a tetrahedral element due to it's shape cannot have fine resolution in vertical direction and coarse resolution in lateral directions at the same time. However, this is exactly what is required because confining potential varies slowly in lateral directions as compared to vertical. Tetrahedral elements are required on the top surface to

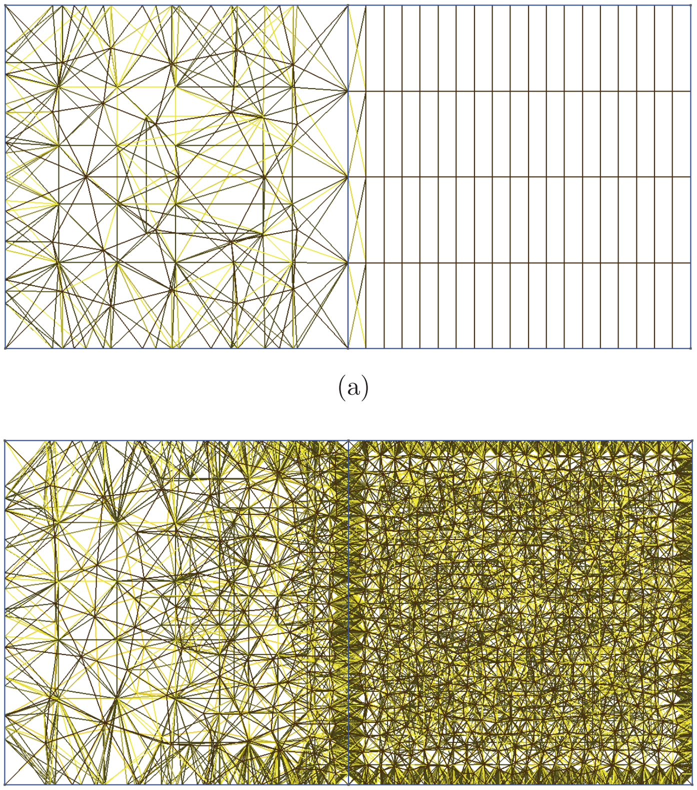

(a)

(b)

Figure 2.2. Comparison between a mesh created using only tetrahedra (b) and by mixing tetrahedra, pyramids, prisms and hexahedra (a). (a) contains 745 vertices and (b) contains 9726 vertices. Both have 20nm resolution on the left side and 5nm resolution on the right in vertical direction. (a) uses pyramids and prisms to connect the tetrahedra to cuboids.

match gate geometry, and cuboid elements in the regions of doping and semi-classical or quantum charge density. Therefore, a mixed FEM mesh is used as shown in Fig. 2.2a.

2.5 Schrödinger-Poisson self-consistency

To model electron-electron repulsion in the mean field using the Hartree approximation, continuum Schrödinger (Eq. 2.1) and Poisson (Eq. 2.9) have to be solved self-consistently. When the two equations are self-consistently solved, quantum density obtained by solving Schrödinger equation, gives the same electrostatic potential from solving Poisson equation that was used to calculate it. The Hartree approximation neglects exchange and correlation energies of electrons, which can be modeled using density functional theory by adding an extra term as shown in Sec. 2.1.

The Poisson equation becomes non-linear in electrostatic potential when quantum density is included. Such a system can be solved iteratively using Newton's method as described in Appendix C. The system becomes more non-linear in quantum dots at mili-Kelvin temperatures, for which the Newton's method becomes inadequate. In this case, the Predictor-Corrector (PC) method is used, which is derived in Appendix D. The PC method works by isolating the non-linearity in an inner loop (predictor) that uses an inexact quantum density calculated from first order perturbation theory. The inner loop acts like a Jacobian by predicting the next step for the outer loop (corrector).

2.6 Numerics

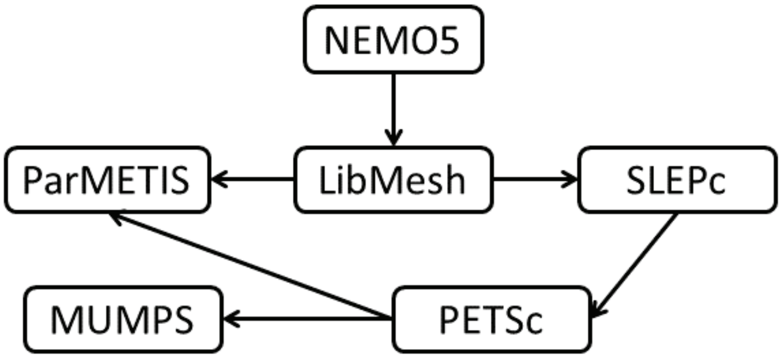

Figure 2.3. Dependency graph of numerical libraries

The tool primarily uses the LibMesh [78] library for handling the meshes, parallelization across multiple processes by domain decomposition, and calling the numerical solvers. The library dependency is shown in fig. 2.3. The most computationally intensive numerical tasks in the self-consistent quantum simulation are 1) computing eigenvalues of the Schrödinger equation in matrix form (Eq. A.3), and 2) solving the linear system in Eq. C.1 to get potential V^{n+1} for $n+1^{th}$ step. The library SLEPc [81,82] is used for computing the lowest eigenvalues using the generalized Davidson method. The geometric algebraic multi-grid (GAMG) preconditioner along with the generalized minimum residual method (GMRES) in the PETSc library [83,84] is used to solve the Poisson linear system. These methods are highly scalable.

2.7 Parallelization

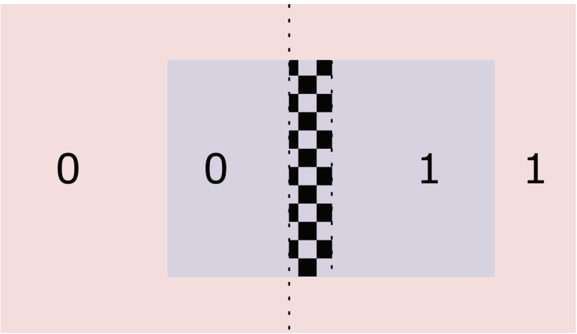

Figure 2.4. Partitioning of Schrödinger (blue) and Poisson (red) regions. The numbers show the processor onto which that part of the region goes. The shaded part is the spatial region which is on processor 0 of Schrödinger and processor 1 of Poisson mesh. Thus, quantum density is calculated on processor 0, and needs to be communicated to processor 1.

LibMesh library is used to import the mesh and distribute it onto multiple processors. Partitioning of the elements onto different processors is done by LibMesh using the ParMETIS library, depending on the connectivity graph of the elements. The mesh used for solving Schrödinger equation is a subset of the Poisson mesh. Since both meshes are partitioned among the maximum number of available processes, a spatial location might belong to different processors in the two meshes as shown in fig. 2.4. During the set-up phase, points on one mesh are located on the other and points in the intersecting regions are communicated. When the density is solved later in each iteration, data at the relevant points is communicated using non-blocking sends (MPI_ISend) and blocking receives (MPI_Recv) available in standard MPI library implementations.

2.8 Testing

Table 2.1.
Comparison of simulation and theory for harmonic oscillator eigenvalues

Theory	**Simulation**	**Degeneracy**
5.05	5.08	1
8.43	8.48	3
11.85	11.90	5

(a) 3D harmonic oscillator

Theory	**Simulation**
3.109	3.108
6.484	6.481
9.863	9.853

(b) 1D harmonic oscillator

The implemented effective mass Schrödinger solver was tested using 3D and 1D harmonic oscillator potentials, since the eigenvalues and eigenvectors can be analytically calculated. The computed eigenvalues for 3D case match within 1% of theoretical values, as shown in Table 2.1.

2.9 Scaling

A test structure made up of a double quantum dot in Si/SiO$_2$ heterostructure is simulated with semi-classical first followed by quantum density. The Poisson mesh size is 443,290 nodes and 2,585,055 elements whereas Schrödinger mesh size is 124,968 nodes and 706,601 elements. The simulation was run on 32, 42, 48, 56 and 64 processors. Both the semi-classical and quantum solvers are seen to scale well up-to 64 processors as shown in fig 2.5. The set-up time doesn't scale very well if most of the nodes of the Schrödinger mesh fall in a small number of processor domains of the Poisson mesh.

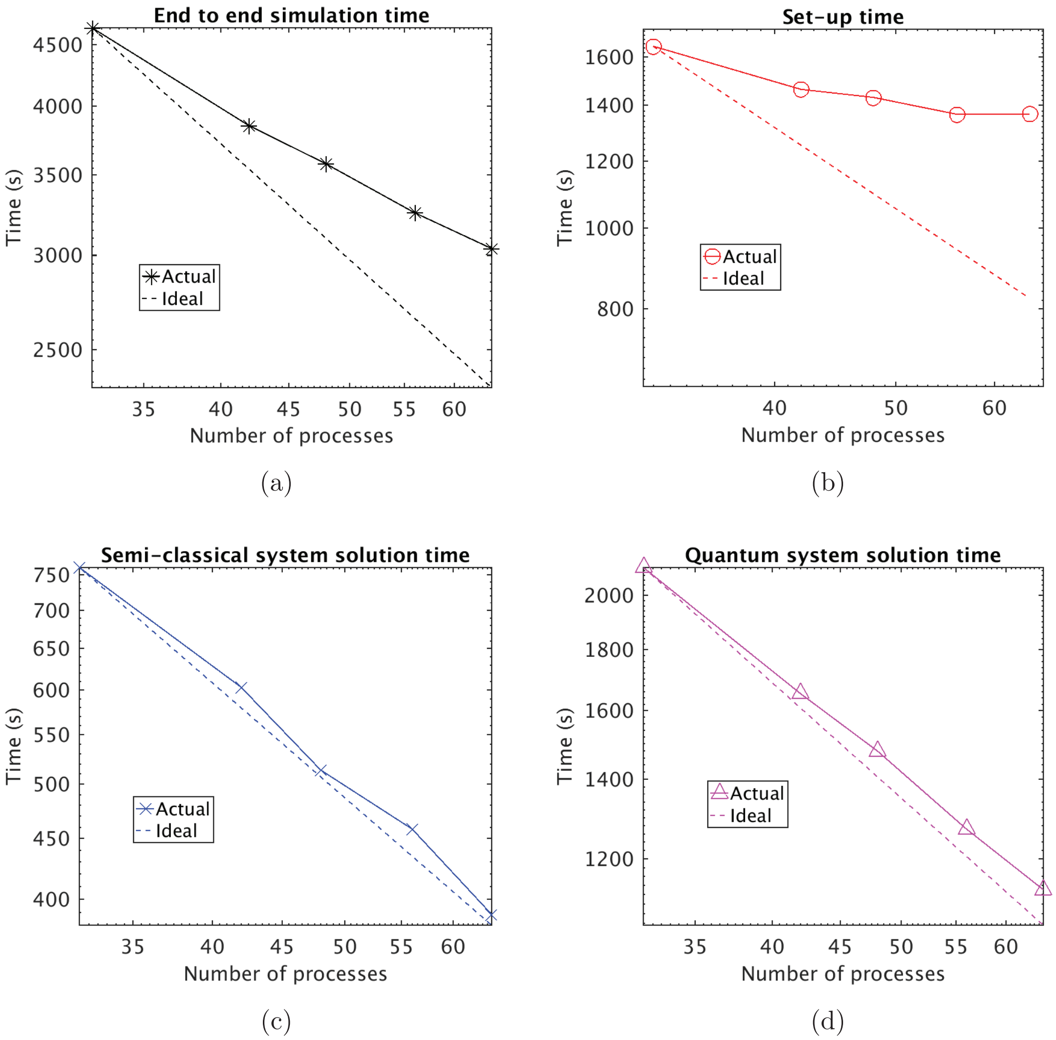

(a) (b) (c) (d)

Figure 2.5. Strong scaling plots of a self-consistent quantum dot Schrödinger-Poisson calculation. a) Total start to end simulation time. b) Set-up time, during which the intersection of Schrödinger and Poisson meshes is calculated and communicated. The scaling for set-up is bad when most elements of the Schrödinger mesh fall in a region of the Poisson mesh that resides on a small number of processors. c) Semi-classical system solution time, during which the Poisson equation (Eq. 2.9) is solved self-consistently with the semi-classical density (Eqs. 2.4, 2.5) using the Newton's method discussed in Appendix C. d) Quantum system solution time, during which the Poisson equation (Eq. 2.9) is solved self-consistently with the Schrörindger equation (Eq. 2.1) using the PC method described in Appendix D.

3. OPTIMIZATION OF EDGE STATE VELOCITY IN THE INTEGER QUANTUM HALL REGIME

This chapter has been reproduced with permission from [85] (doi: 10.1103/PhysRevB.97.085302). The reuse license is displayed in Appendix E.

3.1 Introduction

Electronic interferometers have been used as tools to probe the behavior of edge states in the quantum Hall regime. A typical electronic interferometer consists of two Quantum Point Contacts (QPCs) which act as electron beam splitters, in analogy to optical interference experiments. Electrons traversing the interferometer's path accumulate an Aharonov-Bohm phase equal to 2π times the number of magnetic flux quanta encircled. This phase can be controlled either by varying the area of the device or changing the magnetic field, yielding conductance oscillations. A major challenge for electronic interferometry is that the interfering particles must maintain phase coherence throughout their trajectory around the interference path. This is possible only if the quasiparticle edge state velocity is high enough that the time taken to traverse the interference path is smaller than the phase coherence time. Unsurprisingly, a strong correlation has been observed between the edge state velocity and the visibility of interference oscillations in the integer quantum Hall regime [86].

The fractional quantum Hall effect (FQHE) emerges from Coulomb interactions between electrons in a two-dimensional electron gas (2DEG) in a perpendicular magnetic field [29]. The FQHE states are predicted to host exotic quasiparticle excitations which carry fractional charge and obey anyonic braiding statistics, and these properties may be probed in interferometers [13, 14, 38, 87]. While Aharonov-Bohm interferometery has been conducted in the integer quantum Hall regime [38,39,88], extending to the fractional quantum Hall regime has proven to be difficult. The problem of maintaining coherence may be exacerbated in the FQH regime due to the presence of neutral edge modes, which have been predicted [33,89,90] and experimentally observed [91, 92] at many states. Crucially, the neutral edge mode becomes entangled with the charge mode and must also maintain coherence along the trajectory of the interferometer [93], which may preclude observation of interference because the neutral modes are expected to propagate with a much lower velocity than the charge modes [94, 95]. Thus, optimizing device parameters to maximize the velocity of edge modes is critical to observing interference in the FQHE regime.

The drift velocity of charge carriers in the classical Hall effect is equal to the ratio of electric field to magnetic field, E/B. On general grounds the edge state velocity in the quantum Hall regime is expected to be proportional to the velocity scale set by E/B, where in this case the electric field E is due to the confining potential at the edge. Experiments in the IQHE have confirmed that the edge velocity is approximately proportional to $1/B$ [88, 96–98]; however, a framework for analyzing the confinement potential and predicting the velocities in different heterostructures and gating schemes is needed. While for concreteness we analyze edge velocities in the IQHE regime, the principle that edge state velocity increases for sharper confining potential is expected to generalize to the fractional regime as well [94, 95]. Additionally, it has been found that precise tuning of the quantum point contacts is required to achieve interference [88], so we seek to understand the behavior of QPCs both in the quantum Hall regime and at zero magnetic field. We focus on the case of GaAs/AlGaAs heterostructures with 2DEG edges defined by metallic gates.

Numerical simulations have proven to be valuable tools for designing heterostructures [99] and gated devices [64,100], as well as in explaining the results of experiments in the quantum Hall regime [101, 102]. The Poisson equation has been previously solved computationally in the IQHE regime for GaAs/AlGaAs heterostructures using a Thomas-Fermi approximation (TFA) to calculate the electron density and potential due to QPCs [64, 100, 103]. However in these works the doping ionization is not con-

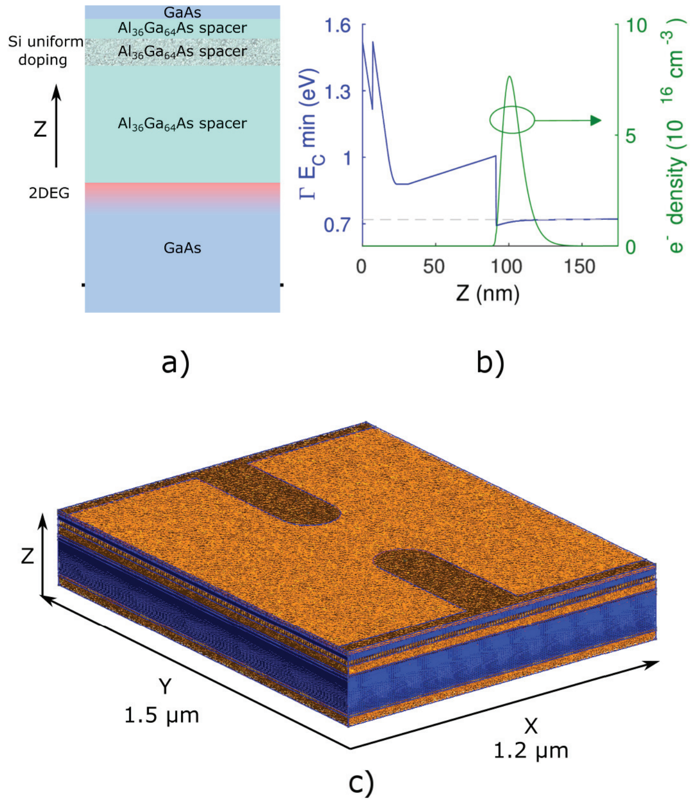

Figure 3.1. The details of heterostructure and gate layout used for benchmarking the simulation method. **a)** A cartoon showing the different layers and the shaded 2DEG location in the 91 nm deep single hetero-junction structure with modulation doping. A uniform doping profile with a concentration of 4.8×10^{18} cm^{-3} between 17 and 31 nm depths was used in experiments. **b)** The conduction band and electron density profiles of the quantum well solved self-consistently using a 1D Schrödinger-Poisson simulation. Valence band maximum on the left edge is at 0 eV, and the dashed line is the Fermi level. **c)** The 1.5μm (cross-section) × 1.2μm (transport direction) × 250nm (growth direction) sized finite element mesh used to discretize Poisson equation for the QPC. The mesh contains tetrahedral elements (orange) to efficiently fill the dielectric regions which contain no free charge, and cuboid elements (blue) in the regions containing free charges. Pyramid and prism shaped elements (orange) are used to connect dielectric regions to charged regions. The cuboids in charged regions are thin along the growth direction, in which potential changes fast and coarse along the lateral direction in which potential changes slowly. The mesh contains $\sim$ 2.16 million points at which the electrostatic potential is solved.

sidered self-consistently. Also, these works model doping and quantum well regions in 2-dimensions instead of 3-dimensions. Taking these parameters into account is essential for correctly modeling the electric field at the edges, and in turn, the edge state velocity.

Here a method is presented for calculating electron edge state velocities and electron density in gated QPCs in the IQHE regime. The electrostatic simulations tool developed in the NEMO5 [104] package is used for self-consistently solving the three-dimensional Schrödinger and Poisson equations in the IQHE regime. Following Stopa et al. [105] and Fiori et al. [74], the 3D Schrödinger equation is split into 1D and 2D parts. The electron interactions are calculated using the mean field Hartree approximation in electrostatic simulations. A frequently used incomplete ionization model (discussed in Sec. 2.2) is employed for dopants in which Fermi-Dirac statistics and a donor energy level is used. The full 3D Poisson equation is solved by accounting for the thickness of doping layers and 2DEG. Electrostatic simulations solve the potential landscape and use a Gaussian broadened Landau level density of states in the IQHE regime. The potential obtained is used in quantum transport simulations [106] to solve the 2D Schrödinger equation with open boundaries for the QPCs and calculate the edge state wavefunctions.

The calculated conductance for QPCs is compared with experimentally measured values to benchmark the simulations. The simulated 2DEG density is also compared with experiments to tune certain parameters such as donor ionization energy. The methodology is discussed in section 3.2. Figure 3.1 details the heterostructure and QPC gate layout used for benchmarking. On the experimental side, the heterostructure was grown by Molecular Beam Epitaxy (MBE) and Ti/Au metal gates were deposited on the surface. The devices used in the experiment have the same physical dimensions as in the simulation. The method is benchmarked with experiments in Sec. 3.3.1. Sheet density, sub-band energy and edge state wavefunction profiles are discussed in the rest of Sec. 3.3. In Sec. 3.4, the edge state velocity is studied as a function of magnetic field and gate voltage for four different structures in a attempt to maximize the velocity.

3.2 Methodology

Typically, interference experiments operate with small source-drain biases on the order of μV to avoid heating the 2DEG [88, 107]. The subband energy of electrons due to confinement in the quantum well varies on the order of meV and is much larger than the applied bias. Source-drain bias is thus neglected in electrostatic simulations. The overall repulsive effect of electron density on itself is calculated by solving the Schrödinger equation self-consistently with the Poisson equation, which is a standard practice for modeling semiconductor heterostructures [67]. The two equations are discretized using a non-uniform mixed element finite element mesh (Figure 3.1c). Self-consistent iterations are done using the predictor-corrector method [108]. Figure 3.2 shows the simulation flow.

3.2.1 Poisson equation

The effects due to the top surface, donors, gates and background disorder are included in the semiconductor Poisson equation (Eq. 2.9).

Donor Statistics

The charge density due to donors is included using Eq. 2.7. A single donor level is considered in the simulations and its ionization energy $E_C - E_D$ is tuned such that the bulk 2DEG sheet density calculated from self-consistent 1D simulations matches the one obtained from experiments. The Si modulation doping layers screen the effect of top gates because of the presence of donor energy levels near the conduction band. Si atoms in $\mathrm{Al_xGa_{1\text{-}x}As}$ appear to be in both shallow and deep donor levels at $x > 0.2$. However, at $x = 0.36$, majority of Si atoms become deep donor levels, the

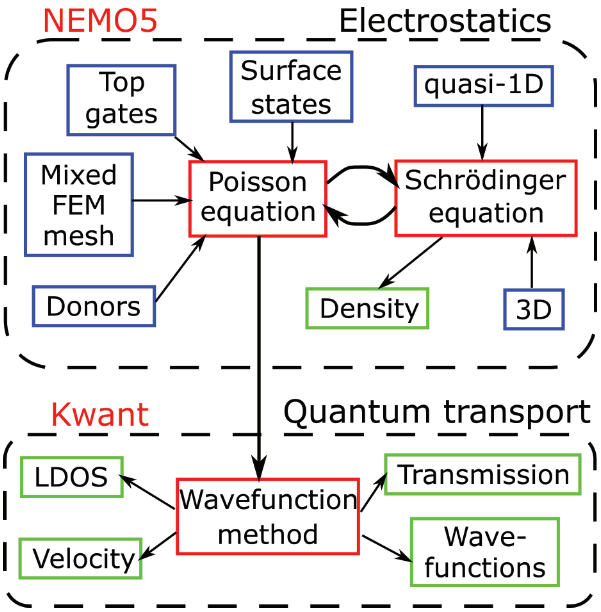

Figure 3.2. The simulation flowchart. Quasi-1D Schrödinger and Poisson equations are solved self-consistently to get the electrostatic potential and 2DEG density near the QPC. Section 3.2.1 gives details of the Poisson equation, which takes into account top gates, surface states, incomplete donor ionization and uses a mixed FEM mesh to solve complex heterostructures efficiently. The quasi-1D Schrödinger equation is solved for QPCs as described in Section 3.2.2. The potential profile obtained from electrostatics is used in quantum transport simulations (Sec. 3.2.5) for calculating the QPC transmission, local density of states (LDOS), current densities, wave-functions and their velocities. Electrostatic simulations are done using the NEMO5 [104] package, while the quantum transport simulations are done using the Kwant [106] package.

so-called DX centers [109]. The physical origin of DX centers is under controversy and the most accepted model proposed by Chadi and Chang [110] suggests that the DX center is formed by the displacement of substitutional Si atom along [111] direction to lower the electronic energy. In this model, there is a potential barrier for trapping and de-trapping of electrons in DX centers which results in freezing out the electrons at low temperatures. Hence, the only participating donors when the sample is not illuminated, are those which remain ionized as the device is cooled down to mK temperatures.

The effective total density of participating Si donors N_D in eq (2.7) also needs to be modified from the real doping density used in experiments to model the effect of donor freeze out. To model the freezing out of donors, self-consistent 1D simulations of the heterostructure are done first with all the donors present and then the unionized donors are removed in 3D simulations. The unionized donors, which are removed in 3D simulations, are kept while the ionization energy is tuned. After considering the effect of frozen electrons in deep centers, the simulated gate voltage required for depleting the 2DEG is comparable to the experimentally observed value.

Fermi level pinning due to dangling bonds on exposed GaAs surface

The Fermi level pinning on the exposed top GaAs/AlGaAs surfaces is included in the model for QPCs using Neumann boundary conditions in the Poisson equation (2.9). Charge density on the exposed surface due to occupied dangling bonds creates a Schottky barrier [73]. The Schottky barrier can be modeled by setting a constant voltage (usually -0.7 to -0.8 V) with respect to the Fermi level at the top surface using the Dirichlet boundary condition [111]. To model the Fermi level pinning, an electric field can also be specified at the top using the Neumann boundary condition [112]. The electric field is calculated from the slope of the conduction band when Dirichlet boundary condition is used in 1D simulations. Setting the electric field at the top is equivalent to having frozen charges at the top surface. Other more complicated models [75, 76, 102] can be used to specify a density of states at the surface, which lead to Fermi level pinning. Potential and density in the QPC channel are affected by the boundary condition of the exposed surface as shown for heterostructures with shallow 2DEG [74].

3.2.2 Schrödinger equation

Free electrons in the quantum well at the GaAs/AlGaAs interface occupy the lowest sub-band in the GaAs conduction band gamma valley and can be approximated by a parabolic dispersion relation [67]. Thus the effective-mass Schrödinger equation (Eq. 2.1) can be used. The position-dependent effective mass $m^*(r) = 0.067m_e$ is equal for both GaAs and AlGaAs gamma valleys, where m_e is the free electron mass. Electrostatic potential V is obtained from solving the Poisson equation (2.9). The Electrostatic potential changes slower in the lateral direction than in the growth direction. Following the work of Fiori et al [74], the 3D wavefunction Φ can thus be expanded as $\Phi(x, y, z) = \psi(x, y, z)\chi(x, y)$. Here ψ is the 1-D wavefunction along Z (growth) axis evaluated at different points in the X-Y plane. χ is the 2D envelope along the lateral direction. The 3D Schrödinger equation can be separated into 1D and 2D parts by substituting the expression for Φ:

$$-\frac{\hbar^2}{2}\frac{\partial}{\partial z}\frac{1}{m^*}\frac{\partial\psi}{\partial z} + V_{tot}\psi = \tilde{E}\psi \tag{3.1}$$

$$-\frac{\hbar^2}{2m^*}\nabla_\perp^2\chi + \tilde{E}_i = E\chi \tag{3.2}$$

$\tilde{E}_i \equiv \tilde{E}_i(x, y)$, called the sub-band energy, is the eigenvalue corresponding to ψ_i. We assume the sub-band energy to be flat as it is slowly varying and calculate the approximate electron density to be used in self-consistent simulations

$$\begin{aligned} n(x, y, z) = &\frac{kTm^*}{\pi\hbar^2}\sum_{i=1}^{\infty}|\psi_i(x, y, z)|^2 \\ &\times \ln\left(1 + \exp\left(-\frac{\tilde{E}_i(x, y) - E_F}{kT}\right)\right) \end{aligned} \tag{3.3}$$

The log term comes from integrating the density of states of a parabolic dispersion for 2D periodic systems.

For QPCs, equation (3.2) has open boundary conditions and needs to be solved using quantum transport algorithms (discussed in sec 3.2.5) to model the transmission, resistance, quantum current density and edge state velocity. Electrostatic simulations require the electron density for self-consistently obtaining the electrostatic potential. Using quantum transport algorithms to calculate the density in micron sized structures is computationally prohibitive. Ballistic transport simulations produce a delta function DOS in the bulk for the Landau levels, for which the energy is difficult to pinpoint, requiring a fine energy grid for integrating the electron density. Adding inelastic scattering terms to the quantum transport equations [113] for broadening the Landau level DOS would further increase the computational requirements. Making the assumption of a slowly varying sub-band energy in equation (3.2) to analytically integrate the electron density for the electrostatic simulations is computationally efficient, but neglects the lateral spread of the edge state wavefunction. The sub-band energy profile obtained from electrostatic simulations is used to solve eq. (3.2) with open boundaries. This approach has been shown to match experimental QPC conductance in zero magnetic field [74].

Integer Quantum Hall Regime

The method described in the previous section is employed in the IQHE regime, where Gaussian broadened Landau level density of states is used. In the presence of a perpendicular magnetic field, equation (3.2) can be re-written as

$$\frac{(i\hbar\nabla_{\perp} + e\mathbf{A})^2}{2m^*}\chi + \tilde{E}_i + g\mu_B B\sigma_z = E\chi \tag{3.4}$$

A is the vector potential, g is the Landé g-factor (discussed later), μ_B is the Bohr magneton and B is the magnetic field. The assumption of a slowly varying $\tilde{E}_i$ is employed again, which reduces equation (3.4) to that of non-interacting electrons trapped in 2D in presence of a perpendicular magnetic field. Then, solving (3.4) gives us the Landau level (LL) density of states (DOS) for the i^{th} sub-band

$$\begin{gathered} D_B^i = \frac{1}{2\pi l_B^2} \sum_{n=0}^{\infty} \delta\left(E - E_{i,n}^+\right) + \delta\left(E - E_{i,n}^-\right) \\ E_{i,n}^+ = \tilde{E}_i + (n + 1/2)\,\hbar\omega_c + g\mu_B B/2 \\ E_{i,n}^- = \tilde{E}_i + (n + 1/2)\,\hbar\omega_c - g\mu_B B/2 \end{gathered} \tag{3.5}$$

where, $l_B = \quad \overline{\hbar/eB}$ is the magnetic length and $\omega_c = eB/m^*$ is the cyclotron frequency. The $\tilde{E}$ term introduces a position dependence to the LL energy. This expression was used by Chklovskii et al. [41] for calculating electrostatics at the edges in the IQHE.

Real devices have broadened LL DOS due to disorder, collision broadening and effects due to a finite wavefunction width, which has been studied in detail by others [114]. To account for these effects, a Gaussian spread DOS around the LL is used.

$$\begin{aligned}\tilde{D}_B^i = \frac{1}{2\pi l_B^2} \, {}^{\infty}_{n=0} \, \frac{1}{\sqrt{2\pi}\Delta E} \; \exp \quad -\frac{E - E_{i,n}^{+}}{2\Delta E^2}^{2} \\ + \exp \quad -\frac{E - E_{i,n}^{-}}{2\Delta E^2}^{2}\end{aligned} \tag{3.6}$$

$\Delta E = \gamma\hbar\omega_c$ is a parameter than defines the spread of the states around the LL energy. The electron density can thus be written as

$$n_B\left(x, y, z\right) = \quad {}^{\infty}_{i=1} \quad {}^{\infty}_{-\infty} \frac{\left|\psi_i\left(x, y, z\right)\right|^2 \tilde{D}_B^i}{1 + \exp \quad \frac{E_i - E_F}{kT}} \, dE \tag{3.7}$$

Güven and Gerhardts investigated the effect of changing γ and temperature on the potential profile [114, 115]. They calculated the potential profile for different values of γ and $t = kT/\hbar\omega_c$. Here, the value $\gamma = 0.05$ is used, which amounts to a standard deviation of 5% of the LL spacing. t is a dimensionless parameter which represents the relative strengths of thermal and magnetic energy scales. Güven and Gerhardts showed that the incompressible region width decreases by roughly 50% when the temperature is increased from $t = 1$ to $t = 2$ for $\gamma = 0.025$. Typical electron temperatures for interferometry experiments range from $10 - 300$mK and magnetic fields are in the range $0.5 - 10$T [116]. For these parameters, t is in the range 5×10^{-5} to 3×10^{-2}. The Fermi function can thus be approximated as a step function without affecting the width of incompressible regions more than the mesh spacing. Evaluating eq. (3.7) with a step Fermi function gives

$$
\begin{aligned}
n_B\left(x,y,z\right) = \frac{1}{4\pi l_B^2} \sum_{i=1}^{\infty} \quad \left|\psi_i\left(x,y,z\right)\right|^2 \\
\times \sum_{n=0}^{\infty} \quad 2 \pm \mathrm{erf} \quad \frac{E_F - E_{i,n}^{+}}{\sqrt{2}\Delta E} \quad \pm \mathrm{erf} \quad \frac{E_F - E_{i,n}^{-}}{\sqrt{2}\Delta E}
\end{aligned}
\tag{3.8}
$$

The first term in the summation comes from integrating the half Gaussian curve under the LL energy. The second term comes from integrating the density of states lying between the LL energy and the Fermi level. + or − sign is used when Fermi level is above or below $E_{i,n}^{+}$ and $E_{i,n}^{-}$ respectively. Using this expression for calculating the density helps with convergence, and gradually increasing magnetic field and temperature from 0 is not required.

Landé g-factor

The g-factor in bulk GaAs is 0.44; however, for two-dimensional electrons in the quantum Hall regime, spin splitting is enhanced due to exchange interactions, and experimental measurements of the spin gap in GaAs/AlGaAs heterostructures have yielded effective g-factors up to 11.65 [117]. The interactions between spin polarized electrons which lead to this enhanced spin splitting can be taken into account using the local spin density approximation (LSDA) [118]. To compare the potential landscape with and without spin splitting, calculations were performed using an effective g-factor of 5.2, the same as the value used by Bilgeç et al. [118], so that the results are comparable with the results using LSDA. No substantial effect was found on the incompressible strip widths due to the low magnetic field range and Landau level broadening.

3.2.3 Discretization and numerics

The quasi-1D Schrödinger and Poisson equations are discretized using finite element method (FEM). For Poisson equation, a mixed element FEM mesh (Fig. 3.1c) containing tetrahedral elements in the dielectric region and cuboid elements in the charged region is used. The electrostatic potential changes faster along the growth direction near the GaAs/AlGaAs interface than in the 2DEG plane. The cuboids are thus 1 nm thick along the growth direction and around 10 nm wide perpendicular to it. The mixed meshes are created using Gmsh software [119]. This mesh treatment allows modeling of large geometries without affecting the computational burden and accuracy. The FEM mesh for Schrödinger equation has only cuboid elements when it is solved for 3D confined case. For QPCs, a 2D rectangular grid is used in plane and a 1D uniform grid along growth direction. The quasi-1D Schrödinger equation is solved independently at each node of the 2D grid to get the 3D density.

The Poisson equation is solved using non-linear solvers present in PETSc [84], along with some additional techniques discussed in the next section. Wavefunctions and eigenvalues in the quantum well are solved using the Krylov-Schur algorithm in the numerical library SLEPc [120]. The integration, parallelization and data handling related to the mesh was done using the software LibMesh [78]. A single simulation at a particular gate voltage and magnetic field runs on ~ 100 processors and takes 1-2 hours to complete.

3.2.4 Self-consistency

Convergence is difficult to achieve and it is system dependent at low temperatures and in presence of magnetic field. To get a monotonic convergence in all types of heterostructures and gate geometries, the predictor-corrector (PC) method (discussed in Appendix D) is used [108].

3.2.5 Quantum transport

2D wavefunctions of the edge states can be obtained by solving equations (3.2) or (3.4) with open boundary conditions using the non-equilibrium quantum transport methods based on non-equilibrium Green's functions (NEGF) [121, 122] or the quantum transmitting boundary method (QTBM) [123]. This work uses the software Kwant [106] which is based on a wave-function approach similar to QTBM for solving the open system.

Zero magnetic field

The 2D part of the Schrödinger equation without magnetic field is discretized using a square grid of side $a = 3$ nm. The effective mass Hamiltonian with 3nm grid has a parabolic dispersion within the relevant energy range of 6 meV above the conduction band minimum. The Hamiltonian can be written as

$$\mathcal{H} = \begin{pmatrix} \ddots & T & \\ T^\dagger & H & T \\ & T^\dagger & \ddots \end{pmatrix} \tag{3.9}$$

$\mathcal{H}$ is an infinite matrix including the 2 left and right semi-infinite regions. H represents the Hamiltonian of one slab of points perpendicular to the direction of transport, and T represents the coupling between the slabs.

$$H = \begin{pmatrix} \ddots & t & \\ t & \tilde{E} - 4t & t \\ & t & \ddots \end{pmatrix} T = \begin{pmatrix} \ddots & & & \\ & t & & \\ & & t & \\ & & & \ddots \end{pmatrix} \tag{3.10}$$

Here $t = \hbar^2/2m^*a^2$, and $\tilde{E}$ is the sub-band energy evaluated at each grid point by cubic interpolation. The Hamiltonian in eq. (3.9) is infinite, and periodicity in semi-infinite regions is required to make it finite. The infinite matrix is reduced to a finite matrix by solving the translationally invariant Schrödinger equation in the semi-infinite region [106] and using the solution of the semi-infinite region as a boundary condition for the QPC region. The Schrödinger equation with the open boundary conditions is then solved as a linear system at a certain energy. The wavefunctions and transmission are obtained from Kwant.

Non-zero magnetic field

The 2D Hamiltonian in presence of a perpendicular magnetic field can be written in a finite difference form with open boundaries similar to eq. (3.9). The kinetic energy term contains vector potential $\mathbf{A}$ due to the magnetic field. Landau gauge is suitable in this case as the dependence of vector potential on the transport (x) direction can be eliminated to make the Hamiltonian periodic. The vector potential used in the work is $\mathbf{A} = -By\hat{\mathbf{x}}$, which gives a constant magnetic field $\mathbf{B} = B\hat{\mathbf{z}}$. As the minimum magnetic length (at 3 T) is approximately 15 nm and our grid size is 3 nm, we can make the Peierls phase approximation to include the vector potential in the off-diagonal part of the Hamiltonian. The diagonal Hamiltonian block of eq. (3.10) remains unchanged, while the off-diagonal block becomes

$$T_B = \begin{pmatrix} \ddots & & & \\ & te^{i\phi} & & \\ & & te^{i\phi} & \\ & & & \ddots \end{pmatrix} \tag{3.11}$$

$$\phi = -\frac{e}{\hbar}\int_{(ai,aj)}^{(a(i+1),aj)} \mathbf{A}\cdot\mathbf{dl} = \frac{a^2 jeB}{\hbar}$$

Here, the path integration is done along a straight path connecting points (ai, aj) and $(a(i+1), aj)$, where i and j are the indices of the points on the square grid. The integral on paths connecting points in the same slab will be zero, since the vector potential points along $\hat{\mathbf{x}}$.

Velocity, current density and resistance

The wavefunction envelopes obtained by solving the quantum transport Hamiltonians are written as χ^i_ν, where i denotes the i^{th} transverse slab and ν is the wavefunction number. The velocity of the ν^{th} transverse mode is then calculated using a dot product of the ν^{th} wavefunctions $\chi^{i\dagger}_\nu$ in slab i and χ^{i+1}_ν in slab $i+1$.

$$v_\nu = \frac{2ae}{\hbar}\mathrm{Im} \quad \chi_\nu^{i\dagger}\chi_\nu^{i+1} \tag{3.12}$$

The local current density of a particular mode between two grid points (i, j) and $(i\ , j\ )$ is calculated using the current operator

$$I_\nu((i, j) \rightarrow (i\ , j\ )) = 2\mathrm{Im} \quad \chi_\nu^{i,j}\mathcal{H}_{i,j,i',j'}\chi_\nu^{i',j'} \tag{3.13}$$

$\mathcal{H}_{i,j,i',j'}$ is the matrix element between grid points (i, j) and $(i\ , j\ )$. The transmission of each mode at the Fermi level, $T_\nu(E_F)$, is obtained directly from Kwant. The resistance is assumed to be in the linear regime, since the Fermi window is narrow at low temperature and source drain bias is on the order of μV. This assumption essentially means that the edge states are in equilibrium with the bulk, since the linear regime resistance is an equilibrium property. The linear response resistance of the QPC at low temperature can be written as [121]

$$R = \frac{h}{e^2} \quad {}_{\nu} \quad T_\nu\left(E_F\right) \quad {}^{-1} \tag{3.14}$$

3.3 Results

3.3.1 QPC resistance benchmark with experiment

Figure 3.3 shows a comparison between measured and computed resistance for a 300 nm wide QPC for the 91 nm deep 2DEG heterostructure. The resistance measurement was done at 300 mK, with no magnetic field using a constant AC current source of 10 nA. The computed resistance shows a good match with the experimentally measured values. The discrepancies between calculated and measured resistance are near depletion (low negative voltage) and pinch-off (high negative voltage) regimes, and agreements are in between these regimes. The electron beam lithography system used to define the QPC has an effective resolution of approximately 20nm, so variations in the true width of the QPC on the order of 20nm are expected, which could lead to additional discrepancy.

The computed depletion voltage is about twice the measured value, because a simple one-level donor ionization model is used and physics of DX center formation is not captured. Also, below the depletion gate voltage the experimental resistance falls to zero, whereas in the simulations the boundary of the 2DEG is the simulation domain (which is much smaller than a Hall bar) leading to a minimum finite resistance. Due to this unphysical condition, simulated resistance isn't shown for gate voltages above the depletion point. Near the pinch-off, the source-drain bias is the highest and thus the accuracy of eq. (3.14) is smaller than at lower voltages. The Thomas-Fermi approximation used to compute density of states laterally gives an inaccurate electrostatic potential in the QPC near pinch-off. Despite these minor discrepancies, the overall agreement between the experiment and simulation is satisfactory between the depletion and pinch-off regimes.

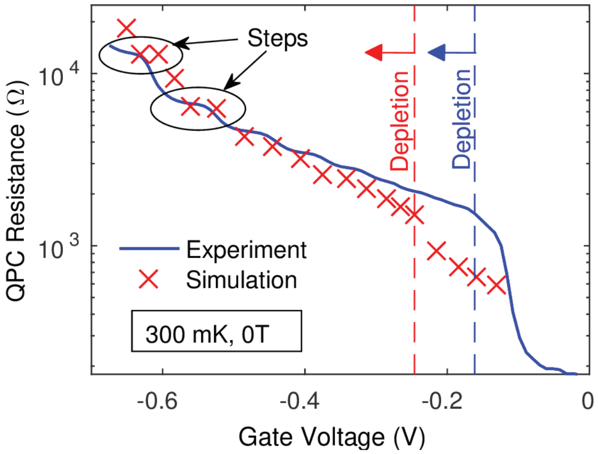

Figure 3.3. Comparison between experimentally measured and computed resistance of a 300 nm wide QPC. The measurement was done at 300 mK in 0 T magnetic field and using a constant AC current source of 10 nA. The red (light) and blue (dark) dashed lines indicate the depletion voltages in simulation and experiment respectively.

3.3.2 Sub-band energy and sheet density profiles

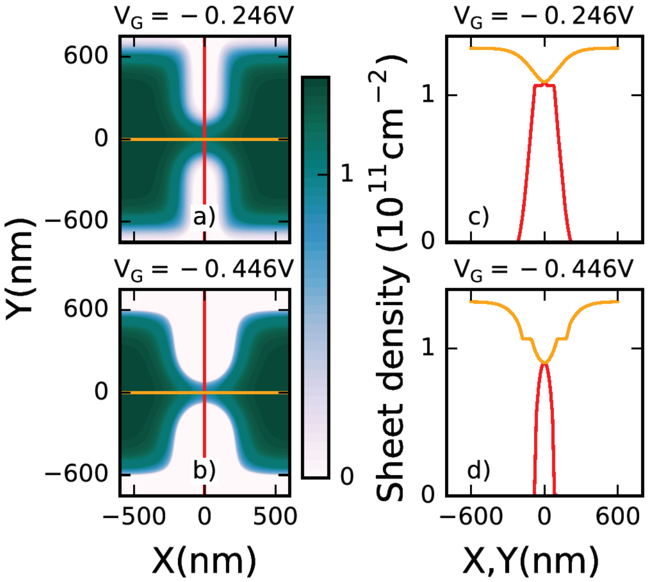

Figure 3.4. Sheet densities at different gate voltages for a 300 nm wide QPC, calculated using the Schrödinger-Poisson solver in a magnetic field of 2.2 T. Panels **c)** and **d)** show cuts along the X and Y axes, passing through the middle of the QPC. Sheet density in the bulk is $1.34 \times 10^{11}\text{cm}^{-2}$, and in the incompressible strip for $n = 1$ LL has a density of $1.06 \times 10^{11}\text{cm}^{-2}$. The incompressible strip can be seen as a light green region near the depleted 2DEG in **a)** and **b)**, and as flat region in **c)** and **d)**.

Figure 3.4 shows the sheet densities near the QPC for different gate voltages at a magnetic field of 2.2T. For a sheet density of $1.34\times10^{11}\text{cm}^{-2}$, a single incompressible strip is expected in the presence of a magnetic field of 2.2T. The incompressible strip can be seen as a band of light green with a density of around $1 \times 10^{11}\text{cm}^{-2}$ near the edges. Using electrostatic simulations, the electron density in the middle of the QPC can be obtained for different gate voltages and magnetic fields. This helps in designing QPCs with the required channel width so that the velocity can be maximized keeping a certain filling fraction in the middle. The correctness of density and potential profiles can be verified by comparing conductance of the constriction for different gate voltages with experiments. The conductance can be calculated using quantum transport simulations.

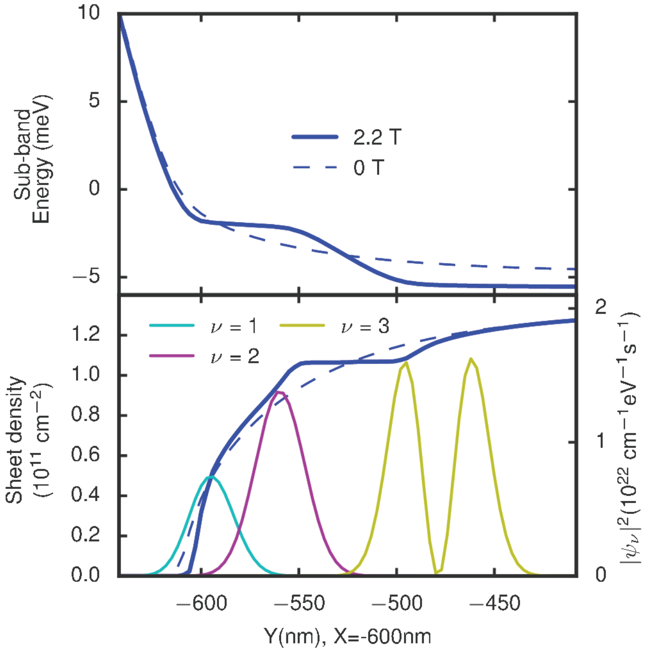

Figure 3.5. Sub-band energy ($E_F = 0$) and sheet density profiles near the edge of the 2DEG defined by depletion top gates at a magnetic field of 2.2 T (bulk filling factor $\nu_{\text{bulk}} = 2.52$) and gate voltage of -0.446 V compared to zero magnetic field values plotted using a dashed line. Edge state wavefunctions at the Fermi level for $\nu = 1$, 2 and 3 Landau levels obtained from quantum transport are also shown.

Figure 3.5 shows traces of the 1^{st} sub-band energy and 2DEG sheet density obtained perpendicular to the 2DEG edge defined by the top gate for a magnetic field of 2.2 T (bulk filling factor $\nu_{\text{bulk}} = 2.52$) and a gate voltage of -0.446 V. The electron density in the presence of magnetic field forms the so called dipolar strips as predicted by Chklovskii et al. [41]. These dipolar strips form as a result of LLs crossing the Fermi level, and because of the dominating electrostatic forces due to the gates leading to a density profile that looks similar to the one without magnetic field. The region where electron density remains constant is the incompressible region, as the Fermi level lies between LLs where the density of states is zero. The incompressible regions in the sub-band energy plot have a finite potential drop across them. The regions where the sub-band energy is flat are called compressible regions because they are located where the LLs intersect the Fermi level. The electrostatics in these regions is similar to that of metals due to a large available density of states.

Figure 3.5 also shows the edge state wavefunctions for Landau levels $\nu = 1$, 2 and 3 obtained from quantum transport simulations. $\nu = 1$ corresponds to spin down and $\nu = 2$ corresponds to spin up in the $n = 1$ Landau level, therefore their wavefunctions have a single lobe. Here, n-Landau levels are spin-less and contain twice the density of states as the ν-Landau levels. The $\nu = 3$ wavefunction lies in the $n = 2$ Landau level and has two lobes. These are the solutions for the Landau gauge. The plotted wavefunctions are normalized to carry a unit current (1 electron per second) such that their transmission equals 1. Therefore, the faster an edge state moves, the smaller its normalization. The wavefunctions clearly show that the edge states are present in the compressible regions.

3.3.3 QPC conductance in the IQHE regime

The conductance is calculated by summing up the transmissions due to all the modes at the Fermi level. Figure 3.6 plots conductance of the QPC at three different magnetic fields. The conductance shows exactly quantized plateaus in units of e^2/h when the modes are either completely transmitted or reflected by the QPC. $\nu - 1$ conducting modes are obtained when the bulk filling factor is close to an even integer. This is because the modes in the ν Landau level at that filling fraction have a very small velocity as shown in Sec. 3.4.1. The electron density and filling factors are obtained from electrostatic simulations. The quantum transport simulations independently show that the extended states lie at the center of LL density of states, which means that the conducting edge states lie in the compressible regions.

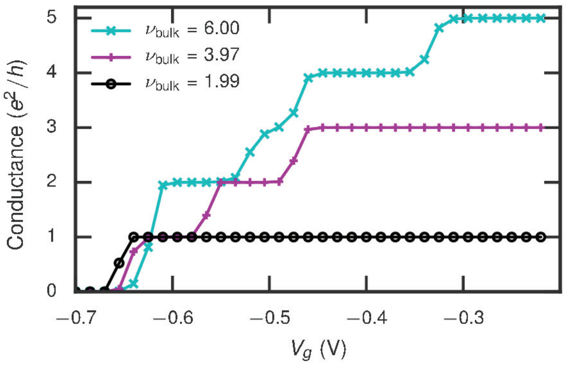

Figure 3.6. Conductance vs applied gate voltage of a 300 nm wide QPC at magnetic fields of 0.9T, 1.36T and 2.71T, and bulk filling factors of $\nu_{\text{bulk}} = 6.00$, $\nu_{\text{bulk}} = 3.97$ and $\nu_{\text{bulk}} = 1.99$ respectively. Each point represents an independent electrostatic simulation. The edge mode of even ν^{th} Landau level starts conducting just above a bulk filling factor of $\nu_{\text{bulk}} = \nu$. This is why we have conductance corresponding to one less edge state than the filling factor.

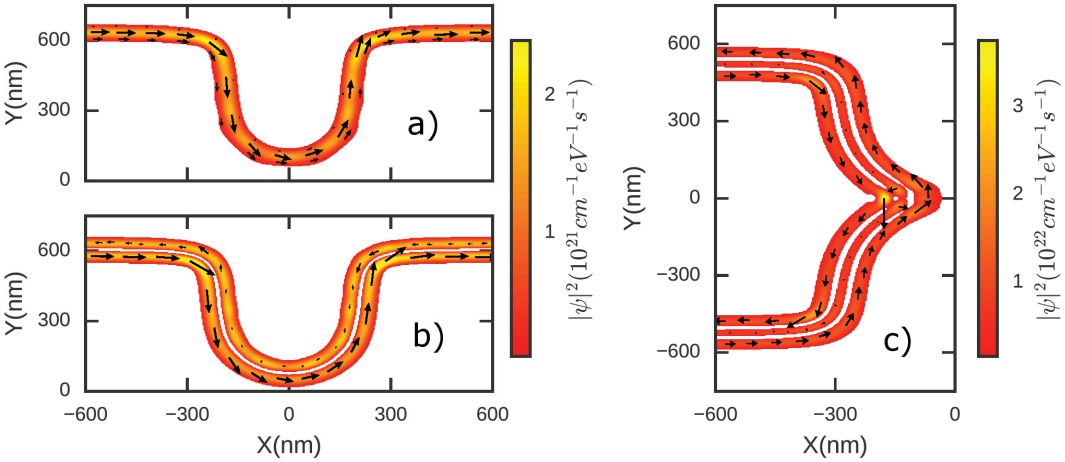

Figure 3.7. A plot of the 3 edge modes in the QPC structure in figure 3.1 for $n = 1$ (**a**), $n = 2$ (**b**) and $n = 3$ (**c**) Landau levels at $V_g = -0.342$V and $B = 0.9$T. The arrows show the direction and relative magnitude of the current density. The conductance of QPC is $2 \times 2e^2/h$, since the innermost mode is reflected by the QPC.

3.3.4 Edge state wavefunctions in the QPC scattering region

Figure 3.7 shows edge state wavefunctions at $V_G = -0.342$V and 0.9T (bulk filling factor of $\nu_{\text{bulk}} = 6$) for a QPC. Figures 3.7a) and b) have fully transmitted and 3.7c) has fully reflected edge states respectively. In this simulation, the spin is neglected and only the wavefunctions for the spin-less Landau levels n are shown. The wavefunctions for $n = 1$, 2 and 3 have 1, 2 and 3 lobes respectively, similar to the harmonic oscillator wavefunctions of the bulk 2D IQHE Hamiltonian in the Landau gauge. The wavefunctions for different spins in the same Landau level n have the same functional form. The current densities calculated using Eq. 3.13 are shown using black arrows. Interestingly, the local current density changes direction for $n = 2, 3$ (figures 3.7 b), c)) and goes opposite to the direction of the current flow. This may be understood semi-classically as the motion of the guiding center of the cyclotron orbit. Pile up of charge can be seen at the corners of the QPC defined 2DEG where the wavefunctions bend.

3.4 Optimization of edge state velocity

In this section the velocities of edge states of different Landau levels are shown as a function of gate voltage and magnetic field for different structures. Eq 3.12 is used for calculating the velocity of the edge states. The velocity obtained from this equation is found to be equal to E $/B$, where E is the expectation value of the electric field for the edge state wavefunctions. The goal of this section is to design heterostructures and gates to obtain a strong electric field at the 2DEG edges that yield high edge state velocities. The velocity saturates even though electric field near the gate gets stronger, due to the finite width of the edge state wavefunction. Therefore, the correct metric for defining the strength of the electric field is the velocity of the edge states, or the expectation value of the electric field for the edge state wavefunctions χ. In this section the velocities of propagating modes are evaluated in the semi-infinite region, thus they are the injection velocities of propagating modes. Velocities calculated elsewhere in the device, but away from the middle region of the QPC, are found to be close to the injection velocities.

Four different structures are considered, as shown in Fig. 3.8, in an attempt to maximize the velocity of edge states. The first structure (Fig. 3.8a) is the same as Fig. 3.1 with top gates. In the second structure (Fig. 3.8b), the doping is moved closer to the 2DEG from 17-31 nm depth to 40-54 nm depth to increase the 2DEG bulk DOS. A depletion top gate is added on the bulk interferometer region to get the same bulk density as the first structure. The gate which defines the edge of the 2DEG is separated from the bulk depletion gate by 100 nm. The idea behind this design is the improve the electric field by making a higher 2DEG DOS available near the edge. The third structure (Fig. 3.8c) has the same heterostructure as the first structure, but uses trench gates with vertical trench walls which can be made using anisotropic etching techniques. Anisotropically etched trench gates that are etched past the doping region have a stronger effect on the 2DEG because the screening due to doping is removed. The fourth structure (Fig. 3.8d) has double-sided delta doping with trench gates etched past the top doping layer, but not past the quantum well and the bottom doping layer. There remains a 25 nm AlGaAs spacer between the trench metallic gate and the quantum well. The 10 nm wide quantum well is at a depth of 155 nm and separated from the doping layers by 45 nm on both sides. The bulk 2DEG density in this heterostructure is 2.11×10^{11} cm^{-2} as compared to 1.34×10^{11} cm^{-2} in the other three structures. Keeping the second doping layer helps pull the electrons closer to the gate and thus increases the edge electric field.

3.4.1 Magnetic field dependence of velocity

The expectation values of the electric field for edge states of the n-Landau levels are plotted as a function of the spin-less bulk filling factor for the four different structures in figure 3.8. The electric field expectation for the spin-less edge state wavefunctions is plotted in Fif. 3.8 to compare the compressible strips widths. The

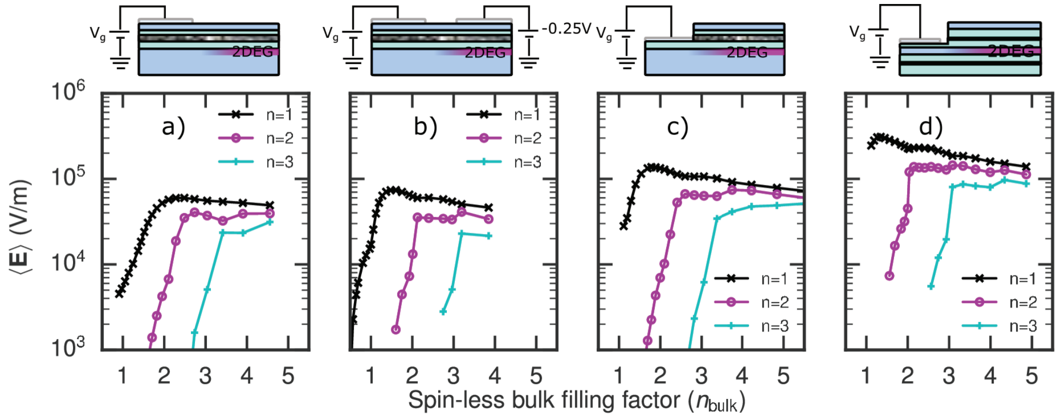

Figure 3.8. Electric field expectation values of edge modes of $n = 1, 2, 3$ LLs for four different structures are plotted as a function of the spin-less bulk filling factor. The structures are described in more detail in section 3.4. Applied gate voltages (V_g) are -0.34V, -0.54V, -0.1V and +0.1V for plots a), b), c) and d) respectively.

top gated structures require a negative bias on the top gate to deplete the 2DEG, whereas the 2DEG under trench gates is depleted at 0V because of the etched doping. A positive bias is applied in the fourth structure to pull the electrons towards the gate. It can be seen from the plots that the electric field expectation value goes to zero as the magnetic field is increased, for the edge states of Landau levels that are partially filled. The electric field expectation value for partially filled Landau levels starts dropping to zero close to half filled bulk Landau level, which means that the edge (extended) states lie at the center of the Landau level DOS.

The two features that define the sharpness of the edge are the maximum value of E and its slope as a function of the filling factor. Both these features depend on the width of compressible region. The compressible region is narrower in a structure as compared to another at a particular magnetic field (equal sub-band energy drop across the compressible regions in the two structures), when E is stronger in that structure. Due to this, the slope of E as a function of the bulk filling factor is also steeper because the width of the compressible region decreases to a smaller value.

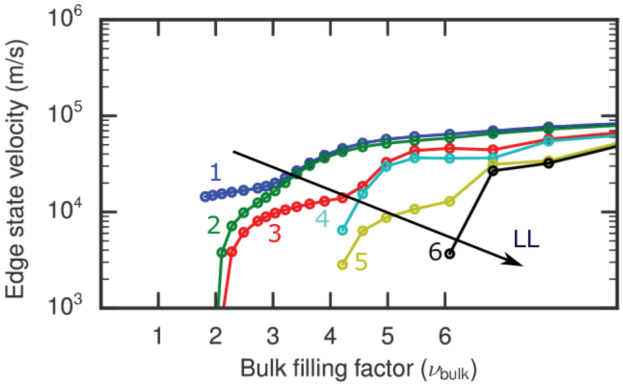

(a)

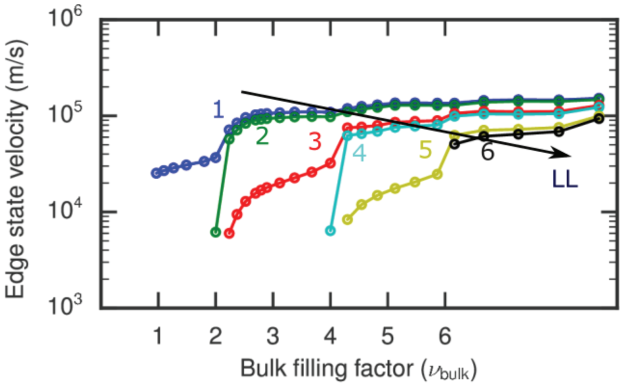

(b)

Figure 3.9. a) and b): Velocities of edge states with spin for the structure in fig 3.8a) and d) respectively plotted as a function of the bulk filling factor ν_{bulk}.

The electric field in trench gated double delta doped structure is the highest among the four structures (figure 3.8).

Figures 3.9a and 3.9b plot the edge state velocities for structures in Figs. 3.8a and 3.8d respectively when the spin is included in the Hamiltonian. With spin included the edge state wavefunctions, which were in the center of the compressible region when spin was excluded, split into two and move towards opposite ends of the compressible region. This can be seen in Fig. 3.5 for $\nu = 1, 2$. This is due to the Zeeman energy and the large effective spin splitting due to interactions [117]. Edge states with opposite spin from consecutive n-Landau levels lie close to each other, e.g. in fig. 3.5 for $\nu = 2, 3$. Therefore the velocity of even ν-Landau level edge states goes to zero just below the corresponding ν bulk filling factor as the wavefunction is close to the inner edge of the compressible region. The velocity of odd ν-Landau level edge states goes to zero close to $\nu - 1$ bulk filling factor as the wavefunction is close to the outer edge of the compressible region. This explains the maximum conductance in fig. 3.6 (conductance plot for the QPC in the IQHE regime). From these plots we can infer that the edge state velocity has an upper limit due to a finite width of the edge state wavefunctions. The velocities are also affected by the electrostatics. This can be clearly seen for the inner edge states, whose velocity decreases close to the even integer ν_{bulk} bulk filling factor and forms plateaus in between.

These results explain the visibility going to zero close to $\nu_{\text{bulk}} = 1$ and $\nu_{\text{bulk}} = 2$ for well defined outer and inner edge channels respectively, in the interferometer visibility measurements of Gurman et al. [86]. For higher bulk filling fractions, low velocity (due to the slow moving neutral modes possibly caused by Coulomb interactions) and inter edge scattering causes a drop in visibility [86], which cannot be predicted using this model. The velocities predicted by this model fall reasonably close to the experimentally measured values; for example $\sim 0.5 - 1.5 \times 10^5$ m/s measured by Mcclure et al [88] and $\sim 2 - 8 \times 10^4$ m/s measured by Gurman et al. [86]. The velocities in the trench gated structures are predicted to be higher on an average by a factor between 1-2 and as much as 10 at certain filling factors for the outer edge.

3.4.2 Gate voltage dependence of velocity

The edges of the 2DEG in the interferometer region are defined by either negatively biased top gates or by trench gates. The 2DEG in the top gated structures is not depleted until a certain negative gate voltage is reached as the doping layer screens the top gate. Trench gated structures on the other hand have depleted 2DEG irrespective of the applied gate voltage when the doping layer is also etched. A positive gate bias can then be applied on the trench gates to pull the edge of the 2DEG closer to the lithographically defined edge to possibly get a larger edge electric field. In the section, the edge state velocities for top and trench gated structures are compared, and their dependence on the gate voltage is studied.

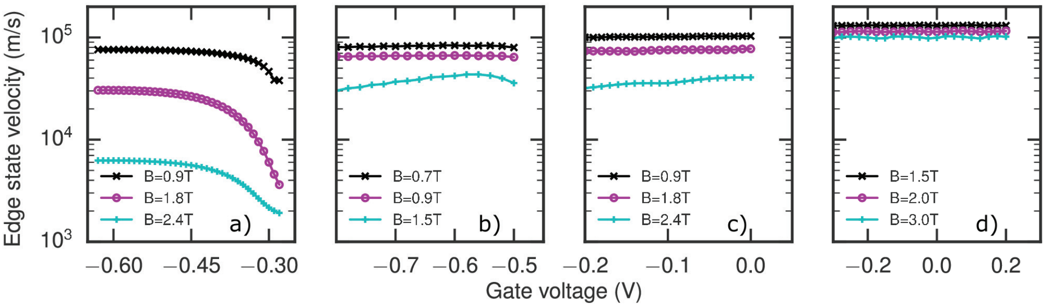

Figure 3.10. Velocities of edge modes for outermost ($n = 1$) $n-$Landau level in same four structures as figure 3.8 at different magnetic fields are plotted as a function of the gate voltage. The spin-less bulk filling factors for the plotted magnetic fields are: a) $n_{\text{bulk}} = 3.04$, 1.51 and 1.14; b) $n_{\text{bulk}} = 2.96$, 2.12 and 1.27; c) $n_{\text{bulk}} = 3.75$, 1.88 and 1.40; d) $n_{\text{bulk}} = 2.93$, 2.14 and 1.44; respectively.

Figure 3.10 plots the velocity of the outermost n-Landau level edge mode at different magnetic fields as a function of the gate voltage for the four structures studied in the previous sub-section. The velocity for the top gated structure (fig. 3.10a) increases as more negative voltage is applied on the gate and saturates at a certain value. This shows that the 2DEG is screened by the doping layer and the edge potential is the steepest when the doping layer is depleted. Fig. 3.10b shows velocities at high negative gate voltages in the saturated regime. A peak can be seen in the velocity near -0.6V for B=1.5T. This is because the edge state moves from under the outer top gate to under the inner top gate while passing through the region with exposed surface. This shows that the region with exposed surface has a larger electric field due to a higher local density of states. This effect is not seen at B=0.7T and B=0.9T because the wavefunctions become wider as magnetic field is reduced and the electric field is averaged out over a larger area. Figs. 3.10c and 3.10d are for the trench gated structures. The velocity increases in Fig. 3.10c the as the gate voltage becomes more positive for B=2.4T. This effect is less pronounced at lower magnetic fields where the wavefunctions are wider. Fig. 3.10d shows negligible dependence of the edge state velocity on gate voltage for the double-side doped trench-gated structure. This could be due to the positively charged lower doping layer pulling the edge state wavefunction closer to the lithographic edge. The gate voltage only changes the location of the edge state and not the electric field expectation value.

3.4.3 Quantum well width dependence of velocity in double-sided delta doped structure

In this sub-section the effect of quantum well width on edge state velocity is studied for the double-sided delta doped structure in fig. 3.8d. Fig. 3.11 plots the average of the edge state velocity for the $n = 1$ Landau level, calculated over the range of gate voltages in Fig. 3.10d. In general, E for edge states increases with the bulk 2DEG sheet density. The bulk 2DEG sheet density increases as the quantum well width is increased; therefore, the velocity also increases with the quantum well width for this structure. However, the quantum well width cannot be arbitrarily increased as this will lead to the formation of a bilayer sheet density. Also, higher magnetic fields are required to get the same filling fraction for larger quantum well widths. The 9 nm-, 10 nm- and 11 nm-wide quantum wells have 2DEG sheet densities of 1.93×10^{11}, 2.11×10^{11} and 2.20×10^{11} cm^{-2} respectively.

3.5 Summary

A simulation method for comparing the edge state velocity in different structures was presented which was used for designing heterostructures with larger edge state velocity. Schrödinger and Poisson equations were solved self-consistently for QPCs defined on GaAs/AlGaAs heterostructures, and the electron density and electrostatic potential were obtained in the IQHE. A set of 1-dimensional wavefunctions are solved

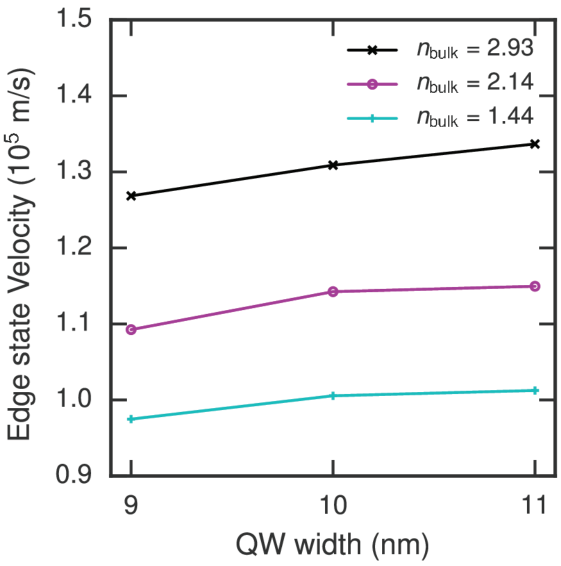

Figure 3.11. Edge state velocity for the n=1 Landau level averaged over different gate voltages as a function of the quantum well width for the structure in fig. 3.8d.

for the interfacial quantum well on a lateral 2-dimensional grid, and the Thomas-Fermi Approximation (TFA) is used to calculate lateral density of states to get the 3-dimensional electron density used in the electrostatic simulations. The broadening of Landau levels due to disorder and various other effects is considered in the TFA using a Gaussian broadening of LLs. Electrostatic simulations show the formation of compressible and incompressible regions near the edge of the 2DEG. The sub-band energies of the quantum well obtained from self-consistent simulations are used in 2-dimensional quantum transport calculations to get the transmission, edge state wavefunctions, velocities and current densities.

Sheet density, sub-band energy and edge state wavefunction profiles for QPCs were obtained from the model. The model was benchmarked by comparing the calculated resistance with the measured resistance for the same structure fabricated experimentally. The edge state wavefunctions were obtained from the quantum transport simulations, which represent the solutions of the 2-dimensional IQHE Hamiltonian in the Landau gauge and for a spatially varying electric field.

The velocity of edge states calculated using quantum transport simulations is equal to $E\ /B$, where E is the electric field expectation value for the edge states. The edge state velocity has an upper limit due to a finite width of the edge state wavefunctions. The magnetic field and gate voltage dependence of the edge state velocity was also compared for different structures. The velocity in the double delta doped anistropic etched trench gated structures was found to be the highest among the four structures considered. It was also showed that the velocity increases with the quantum well width in double side doped structures.

These results can be used to understand some of the visibility and velocity measurements of electronic interferometers operating in the integer quantum Hall regime [86, 88]. The device designs proposed here may lead to improved edge state velocity and thus improved performance of future interferometers, and may enable the observation of interference in the fractional quantum Hall regime.

4. COMPUTATIONAL MODELING OF EXCHANGE SPLITTING IN SILICON-SILICON DIOXIDE DOUBLE QUANTUM DOTS

Parts of this chapter will be submitted to journals in the future for publication, and the journals which publish the individual parts will own the copyrights for those parts.

4.1 Introduction

It was discussed in Section 1.2.2 that electrons trapped in electrostatic quantum dots at the interface of silicon and silicon-dioxide materials can be used for quantum computation. Single qubits are made from the spin of a single electron in which spin-up functions as $|1\rangle$ state and spin-down functions as $|0\rangle$ state. Initialization and read-out of the spin are done using an electron reservoir ("Res") and a single electron transistor ("SET") (Fig. 1.5) in which Coulomb blockade can be used for selective tunneling of an up or down spin electron from/to the dot. Qubit rotations or gates are performed using Rabi oscillations that can be induced by an effective oscillatory magnetic field.

Two qubit gates can be made from two electrons in nearby dots that are tunnel coupled, which means that there is a finite overlap of electron wavefunctions between the two dots. The two electrons then form singlet states which are symmetric/anti-symmetric in orbital/spin parts, and triplet states which are anti-symmetric/symmetric in orbital/spin parts respectively (Eqs. 1.7-1.12). The two qubit gate operation is then performed by applying an AC voltage to the confining gate of one qubit, that resonates with the energy separation between the ground singlet (anti-parallel-spin $|S(1,1)\rangle$) and triplet (parallel-spin $|T_+(B,A)\rangle$ and $|T_-(B,A)\rangle$) states. For the CNOT gate, the AC voltage pulse is resonant with $|S(1,1)$ -$|T_+(B,A)$ transition, in which the electron spin under the gate where the AC voltage is applied flips if the other electron is spin-up.

If the dots aren't tunnel coupled, the resonance frequencies $\nu_{(S\rightarrow T_+)}$ and $\nu_{(S\rightarrow T_-)}$ (Eq. 1.25) are equal. When the dots are tunnel coupled, the these two frequencies are separated by the exchange splitting E_J (Fig. 1.6b). The exchange splitting E_J defines the speed and fidelity of 2-qubit operations: if the slope of E_J vs detuning is large, charge noise couples strongly to the electrons leading to a smaller coherence time, and if E_J is small, a smaller 2-qubit gate speed leads to fewer possible 2-qubit operations over the coherence time. Therefore, the qubits have to be moved from "off" to "on" exchange coupling state before the operation and then restored.

Although the exchange splitting has been calculated as a function of detuning analytically and computationally using quadratic and quartic dot potentials [54–59], these results are qualitative and don't directly help in the device design process. A computational study of exchange splitting has the advantage over analytic studies of using atomistic one-electron wavefunctions having complex amplitudes for the valley part of the wavefunction, with full configuration interaction for two-electron interactions to give a more accurate quantitative model. Additionally, engineering the devices that operate in the desired range of exchange splitting requires design of gate geometry and oxide thicknesses as shown in Fig. 4.1. This chapter presents a computational study of the exchange splitting versus detuning, oxide thickness, and gate width and separation for a realistic device geometry.

4.2 Methodology

The electrostatic potential is calculated using the electrostatic simulation framework described in Chap. 2, in which effective-mass Schrödinger Eq. 2.1 is solved self-consistently with the semiconductor Poisson equation 2.9. The calculated potential is used in atomistic tight binding Hamiltonian [124] for calculating the single

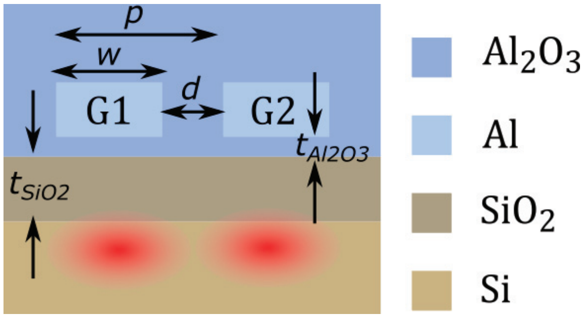

Figure 4.1. An illustration of the various device parameters in Si/SiO_2 double quantum dot. t_{SiO_2} and $t_{Al_2O_3}$ are the SiO_2 and Al_2O_3 thicknesses under the gate, $p = 36$ nm is the gate pitch, w is the gate width and d is the gate separation such that $p = w + d$

electron wavefunctions. The atomistic tight binding model gives z+/- valley splitting due to the interface electric field. The one-electron atomistic wavefunctions are then used in full configuration interaction (FCI) method for calculating the two-electron energy levels and eigenvectors. The complete calculation is described in Fig. 4.2. Details of electrostatic, atomistic and FCI methods are given in this section.

4.2.1 Electrostatic simulations

The Schrödinger and Poisson equations are discretized on a FEM mesh as shown in Fig. 4.3. The Poisson mesh covers the whole device, 2 μm $\times$ 1.5 μm $\times$ 0.5 μm in size, whereas the Schrödinger mesh is only in the region under the gates where the dots form. The Schrödinger mesh is a sub-mesh of Poisson mesh having coinciding nodes between the two meshes. Having coincident nodes helps with convergence of the non-linear system. The Poisson mesh is generated using the commercial software "Sentaurus Device". The node spacing along z-axis under confining gates is 0.1 nm since electrons are confined within 4 nm of the interface, and the effective mass along the vertical direction is ~ 4 times smaller than the lateral effective mass requiring a more accurate parabolic band.

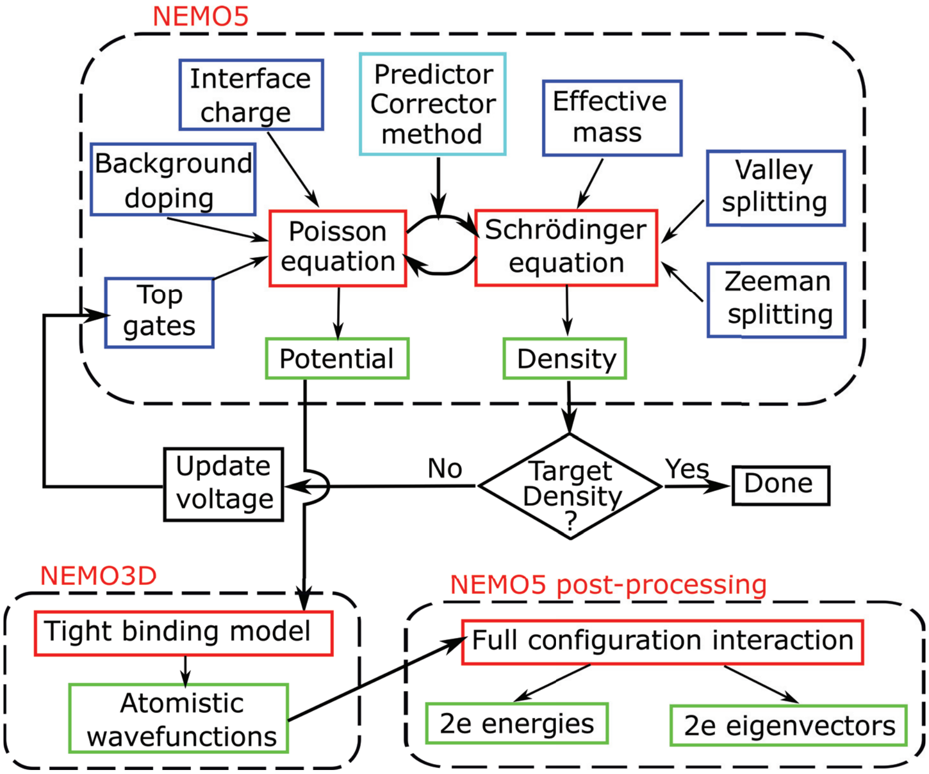

Figure 4.2. Flowchart describing the calculation of two-electron wavefunctions and energy levels from computationally calculated tight binding one-electron wavefunctions. The electrostatic potential used for tight binding calculations is self-consistently calculated using the electrostatic simulation framework.

The effective masses used in the effective mass tensor (Eq. 2.2) are $m_l^* = 0.891m_0$ and $m_t^* = 0.201m_0$ which are the effective masses of the tight binding model in the X valley [124], as compared to the experimental effective masses $m_l^* = 0.916m_0$ and $m_t^* = 0.190m_0$, where m_0 is the free electron mass. Effective masses of the tight binding model are used so that the converged potential from effective-mass Schrödinger-Poisson system would be close to one that could be obtained by self-consistently solving tight binding-Poisson system. The band gap is set to $E_C - E_V = 1.131$ eV obtained from the tight binding model as compared to the experimental $E_C - E_V = 1.118$ eV. Dielectric constants in Si, SiO_2 and Al_2O_3 used in the simulations

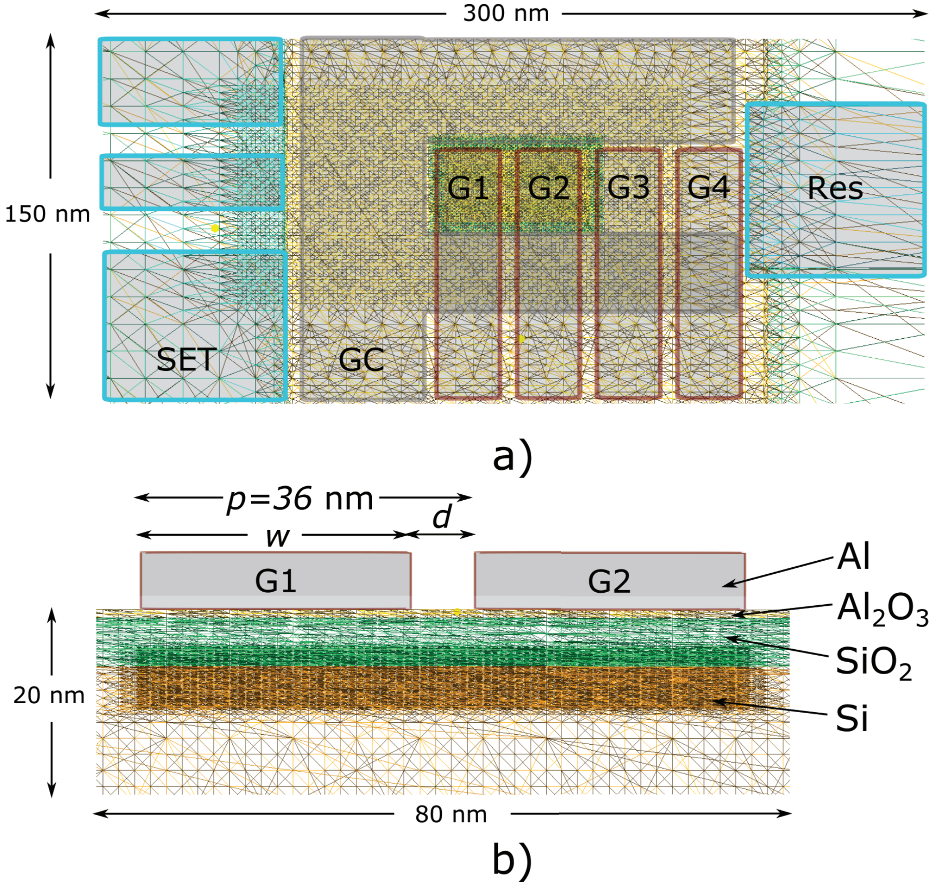

Figure 4.3. Finite element mesh used to discretize Schrödinger and Poisson equations with top gates shown as shaded regions. The mesh has $\sim 550,000$ nodes and ~ 3.5 million elements.

are 11.9, 3.9 and 9.8 respectively. A charge density of 1×10^{12} cm^{-2} was used at the interface of Si and SiO_2 materials to model surface impurities. The various gate voltages used in electrostatic simulations as per the experiments are shown in Table 4.1.

For capturing the correct density of states, which is important in electrostatics, a 4-band effective mass model is used. The energies for these 4 bands are shifted by the valley and Zeeman splittings, neglecting any overlap of the valley orbitals and spin mixing. The valley orbital overlap is important for Coulomb and exchange energies, but not for the one-electron density of states. A valley splitting of 1.9 meV is used, which is obtained from tight binding simulations that used realistic electrostatic potential such that the vertical electric fields were accurately captured. The Zeeman splitting is calculated from the g-factor and magnetic field. The direction-dependent g-factor is obtained from tight binding simulations, which is 1.998 for magnetic field aligned with the [110] crystal direction. A magnetic field of 1.4 T is used in both experiments [12, 15] and simulations.

Table 4.1.
Gate names (Fig. 4.3) and voltages used in electrostatic simulations.

Gate Name	**Gate Voltage (V)**
GC	0.1
G1	V_1
G2	V_2
G3	0.1
G4	2.6
Res	3.4

Gate Name	**Gate Voltage (V)**
SET source	2.2
SET barrier 1	0.86
SET island	2.2
SET barrier 2	0.85
SET drain	2.2

Detuning model

It is difficult to define the detuning between the dots for simulations in terms of energy levels, as the double dot potential gives bonding and anti-bonding orbitals instead of energy levels in left and right dots. In this work, the charge in left and right dots is used to numerically define a detuning point. The total charge in the double dot is fixed to 2 electrons, as the simulations are done in the two-electron regime. The target charges q_1^* and q_2^* in left and right dots are set such that $q_1^* + q_1^* = 2e$, e.g. $q_1^* = 1.4e$ and $q_2^* = 0.6e$.

To get this charge configuration, the unknown target accumulation-gate voltages are V_1^* and V_2^* respectively, which can be calculated iteratively. This is automati-

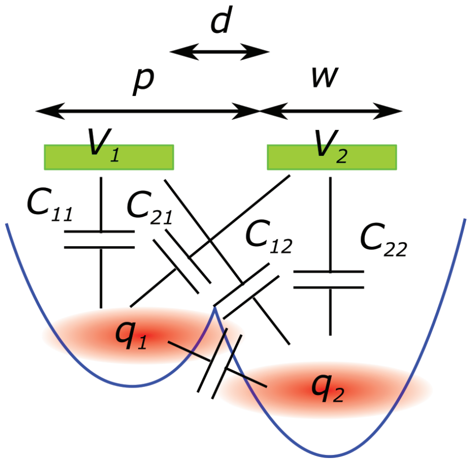

Figure 4.4. An illustration of the gate voltages, dot charges and dot-gate capacitances. Top gates are green rectangles and charges are blurry red ellipses.

cally done using a PYTHON script that calculates the gate-dot capacitance matrix containing elements C_{11}, C_{21}, C_{12} and C_{22} as shown in Fig. 4.4. The capacitance matrix at gate voltages V_1 and V_2 is calculated by adding a small value $\delta V = 1$ mV to each voltage independently and calculating the change in charges in the two dots by running an electrostatic simulation.

$$C_{GD} = \begin{bmatrix} C_{11} & C_{12} \\ C_{21} & C_{22} \end{bmatrix} = \begin{bmatrix} \delta q_1/\delta V_1 & \delta q_2/\delta V_1 \\ \delta q_1/\delta V_2 & \delta q_2/\delta V_2 \end{bmatrix} \tag{4.1}$$

The voltages to be used in the next iteration $\tilde{V}_1$ and $\tilde{V}_2$ are calculated by inverting the capacitance matrix as follows

$$\begin{bmatrix} \tilde{V}_1 - V_1 \\ \tilde{V}_2 - V_2 \end{bmatrix} = \begin{bmatrix} C_{11} & C_{12} \\ C_{21} & C_{22} \end{bmatrix}^{-1} \begin{bmatrix} q_1^* - q_1 \\ q_2^* - q_2 \end{bmatrix} \tag{4.2}$$

This algorithm converges in 3-4 iterations to order 10^{-6} accuracy in the dot charges, given a reasonable set of initial voltages.

4.2.2 Tight binding simulations

The (20 band, $sp^3d^5s^*$ with spin-orbit parameter) atomistic tight binding (TB) model used here is optimized to fit the band structure of Si obtained from the density functional theory, and most accurately represents the valence band and the lower conduction band [124]. The TB Hamiltonian matrix elements consist of on-site energies in the diagonal and coupling integrals that are modeled using the linear combination of atomic orbitals method as shown by Slater and Koster [125]. The fine structure of electron energy levels and, especially the effect of the interface electric field on the valleys in Si quantum dots can be obtained using this model. Valley splitting due to the electric field contributes to the exchange splitting as well. Additionally, atomistic effects such as surface roughness and impurities, which could be beneficial for the spin qubit operation [60, 61] can be accurately modeled using this method. The tight bonding model in the NEMO3D software [126] is used.

It has been shown that the energy levels obtained using the tight binding method in Si quantum dots as small as 3 nm in diameter can be obtained using the effective mass (EM) model [127]. Thus, the EM model is used in electrostatic simulations to reduce computational cost and the electrostatic potential obtained is used in the TB method to model the atomistic effects. The wavefunctions obtained from TB are used to calculate the 2-electron Hamiltonian discussed next.

4.2.3 Full configuration interaction simulations

The two-electron Hamiltonian consisting of the lowest 6 states was discussed in Sec. 1.2.2. The Hamiltonian constructed from the lowest 6 truncated basis states is not enough for calculating the exchange splitting as it doesn't capture the Coulomb and exchange energies due to higher valleys and orbitals [58]. Full configuration interaction (FCI) [59] can be used to computationally calculate the two-electron spectrum, with as many basis states as is required. In the FCI method, the two-electron basis states are the Slater Determinants (SD) of one-electron wavefunctions $|\psi_{a/b}$ as shown below

$$\mathrm{SD}_{a,b} = \frac{|\psi_a(\mathbf{r}_1)\rangle|\,\psi_b(\mathbf{r}_2)\rangle - |\psi_a(\mathbf{r}_2)\rangle|\,\psi_b(\mathbf{r}_1)}{\sqrt{2}} \tag{4.3}$$

The one-electron wavefunctions $|\psi_{a/b}$ are obtained from the tight binding model as described in the previous section. The two-electron FCI Hamiltonian matrix elements having 4 one-electron wavefunction indices a, b, c, d can be written in terms of Coulomb (J) and exchange (K) integrals as shown below

$$\begin{aligned} J_{a,b,c,d} &= \quad \psi_a^\dagger(\mathbf{r}_1)\psi_b^\dagger(\mathbf{r}_2)\frac{e^2}{4\pi\epsilon\,|\mathbf{r}_1-\mathbf{r}_2|}\psi_c(\mathbf{r}_1)\psi_d(\mathbf{r}_2)\,d\mathbf{r}_1\,d\mathbf{r}_2\,, \\ K_{a,b,c,d} &= \quad \psi_a^\dagger(\mathbf{r}_1)\psi_b^\dagger(\mathbf{r}_2)\frac{e^2}{4\pi\epsilon\,|\mathbf{r}_1-\mathbf{r}_2|}\psi_d(\mathbf{r}_1)\psi_c(\mathbf{r}_2)\,d\mathbf{r}_1\,d\mathbf{r}_2 \end{aligned} \tag{4.4}$$

Here the lowest 24 one-electron basis states obtained from the tight binding simulations have been used. Thus, the size of the FCI Hamiltonian is $\begin{smallmatrix}24\\2\end{smallmatrix} = 276$. The Atomistic Configuration Interaction software in NEMO5 [128] was used for the FCI simulations.

4.3 Results

This section shows one-electron and two-electron energies and wavefunctions as a function of quantum dot detuning, oxide thicknesses and gate geometry. The detuning is controlled by the charges in left and right dots. The dot charges are taken from $0.35e$ in the left and $1.65e$ in the right dot to $1.65e$ in the left and $0.35e$ in the right dot in changes of $0.05e$ in left and right dots such that the total charge in the two dots is $2e$. The gate voltages required for obtaining these charges is calculated using the method described in Sec. 4.2.1. The quantity on x-axis in all detuning plots is the difference in gate voltages of “G1” (V_1) and “G2” (V_2), called the plunger voltage $V_P = V_1 - V_2$.

4.3.1 Comparison of effective-mass and tight-binding energy levels

To ensure that the electrostatic potential obtained from self-consistent EM Schrödinger-Poisson simulations is suitable for the TB model, a comparison of EM and TB energy levels as a function of detuning is performed as shown in Fig. 4.5. An x-y cut (parallel to the interface) of the wavefunctions for leftmost, middle and rightmost detuning points obtained from the TB model are also plotted in Fig. 4.5. A difference of ~ 1.3 meV is observed between the EM and TB energy levels for all the dot separations. This difference can be attributed to an abrupt interface in the TB model due to the absence of SiO_2 where the electrons encounter an infinite barrier as compared to a finite barrier in the EM simulations.

4.3.2 Tight binding model energy spectrum

The FCI calculations require the lowest 16-24 TB wavefunctions for an accurate calculation of the exchange splitting. The lowest 24 TB wavefunctions are bonding and anti-bonding orbitals in the Z_+, Z_-, and a combination of X_+, X_-, Y_+ and Y_- valleys for both spins. The TB energy spectrum for 8-, 10- and 12-nm separation is plotted in Fig. 4.4. Care must be taken to ensure that wavefunctions for the same orbitals and valleys are used for FCI calculations at all detuning points. For example in Fig. 4.4 a), a higher orbital (shown in red, energy levels 17-18) crosses a lower orbital (energy levels 15-16). Therefore, if only 16 wavefunctions are used in FCI, this will lead to a jump in two-electron energy levels. Thus, only the energy levels depicted in black are used for FCI.

4.3.3 Two-electron energy spectrum

In this section, the lowest four two-electron energy levels and the ground state singlet amplitudes as a function of detuning is compared for 8-, 10- and 12-nm separation. The energy levels are plotted relative to the Fermi level used in electrostatic

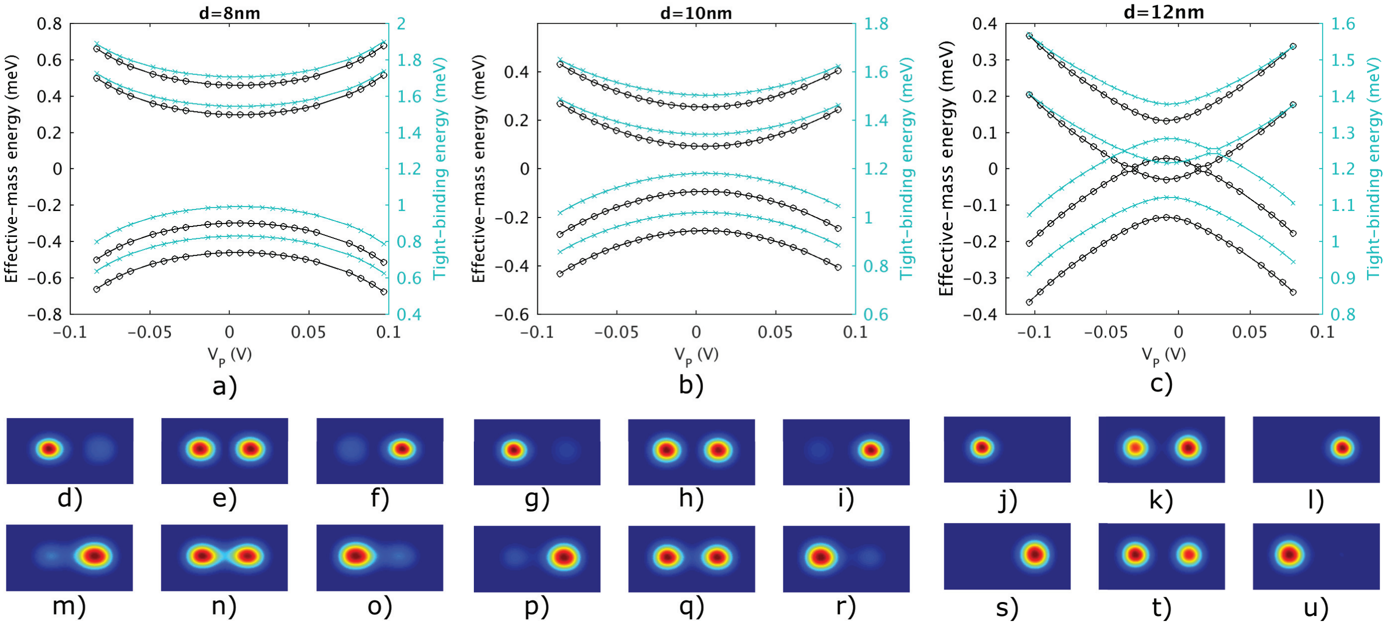

Figure 4.5. a) - c) Comparison of the lowest four energy levels obtained from effective-msss Hamiltonian (black/dark) and tight-binding Hamiltonian (cyan/light) as a function of detuning for 8-, 10- and 12-nm dot separation respectively. The Fermi level used in effective-mass electrostatic simulations is at 0 eV. d) - i) Anti-bonding, and m) - u) bonding orbital wavefunctions obtained from tight binding model. d) m), g) p) and j) s) are for leftmost, e) n), h) q) and k) t) are for zero, and f) o) i) r) and l) u) are for rightmost detuning points for 8-, 10- and 12-nm dot separation respectively. All the calculations are done using a gate pitch $p = 36$ nm, Al_2O_3 thickness $t_{Al_2O_3} = 1$ nm and SiO_2 thickness $t_{SiO_2} = 5.9$ nm.

simulations, in Fig. 4.7. The shift in TB energy levels relative to EM energy levels (Fig. 4.5) is ~ 1.3 meV. The approximate exchange and correlation energy between the bonding and anti-bonding orbitals (Eq. 1.23) obtained by subtracting $2 \times 1.3 = 2.6$ meV from the S/T_0 energy levels, are ~ 4.9 meV, ~ 4.5 meV and ~ 4.2 meV for 8-, 10- and 12-nm dot separations respectively. Exchange and correlation energy is found to dominate as it is much larger than the orbital splitting, which is ~ 0.8 meV, ~ 0.3 meV and ~ 0.1 meV for 8-, 10- and 12-nm dot separations respectively.

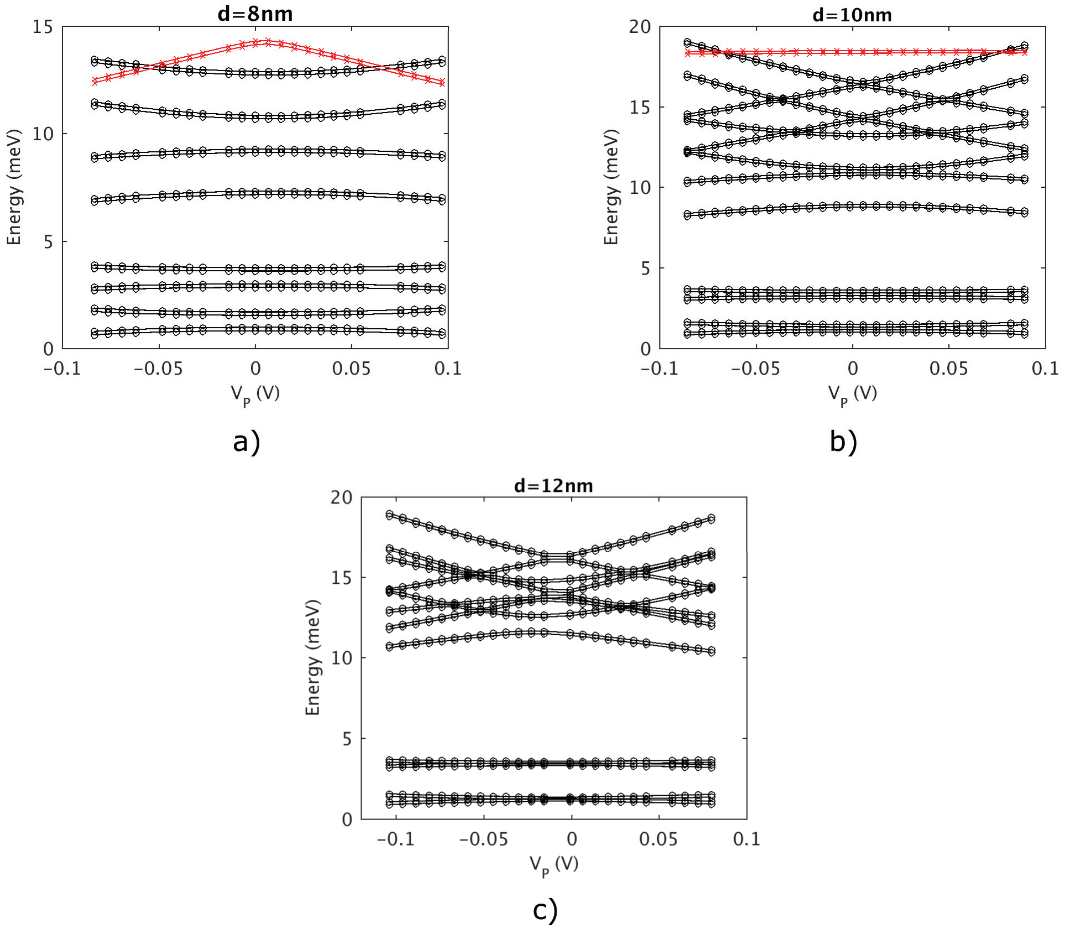

a)

b)

c)

Figure 4.6. a) - c) Tight binding energy spectrum for the double quantum dot as a function of detuning for 8-, 10- and 12-nm dot separations. The black lines with circles are the levels used in FCI calculations, whereas red lines with crosses are not used in FCI. The Fermi level used in effective-mass electrostatic simulations is at 0 eV. All the calculations are done using a gate pitch $p = 36$ nm, Al_2O_3 thickness $t_{Al_2O_3} = 1$ nm and SiO_2 thickness $t_{SiO_2} = 5.9$ nm.

4.3.4 Ground singlet composition and singlet anti-crossings

The ground singlet state is made up of the $|S(B,B)$, $|S(A,A)$ and $|S(B,A)$ singlets as shown in Sec. 1.2.2. These three singlet states are coupled to each other through one- and two-electron hopping integrals as shown in Eqs. 1.19, 1.21 and 1.22. This leads to four separate anti-crossings where the $|S(B,A)$ singlet mixes

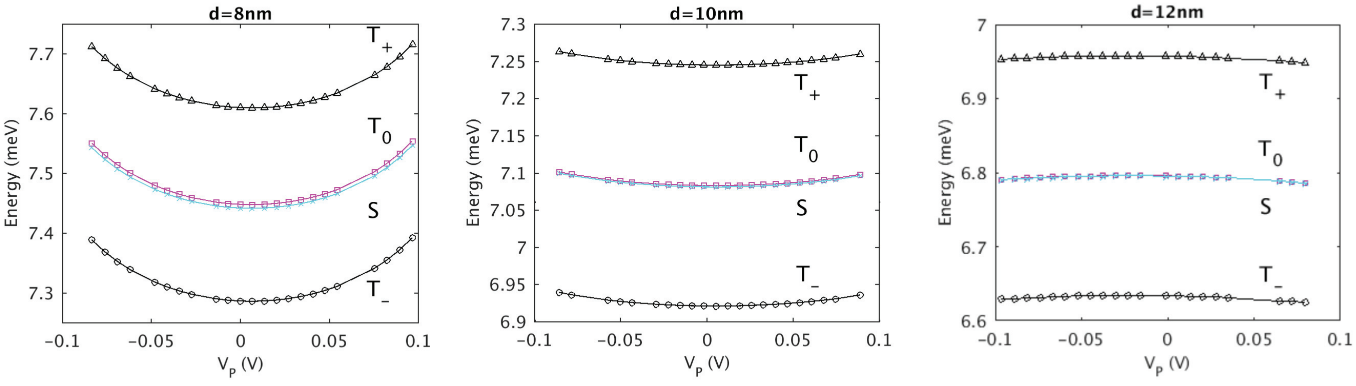

a) b) c)

Figure 4.7. a) - c) Two-electron energy levels obtained from FCI simulations for 8-, 10-, and 12-nm separation. The Fermi level used in effective-mass electrostatic simulations is at 0 eV. All the calculations are done using a gate pitch $p = 36$ nm, Al_2O_3 thickness $t_{Al_2O_3} = 1$ nm and SiO_2 thickness $t_{SiO_2} = 5.9$ nm.

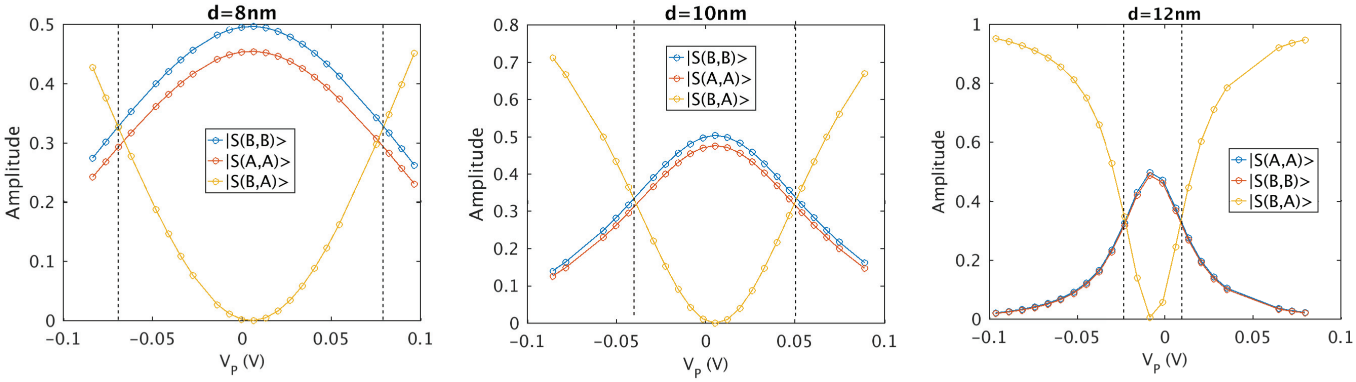

a) b) c)

Figure 4.8. a) - c) Contributions from $|S(B,B)$, $|S(A,A)$ and $|S(B,A)$ singlets to the ground singlet. Dashed lines show the anti-crossing points (not (1,1)-(0,2) anti-crossings) where amplitudes of $|S(B,B)$ and $|S(B,A)$ are equal. All the calculations are done using a gate pitch $p =$ 36 nm, Al_2O_3 thickness $t_{Al_2O_3} = 1$ nm and SiO_2 thickness $t_{SiO_2} = 5.9$ nm.

with either $|S(B,B)$ or a combination of $|S(B,B)$ and $|S(A,A)$ singlets. The anti-crossings on either side of zero detuning where $|S(B,A)$ mixes with $|S(B,B)$

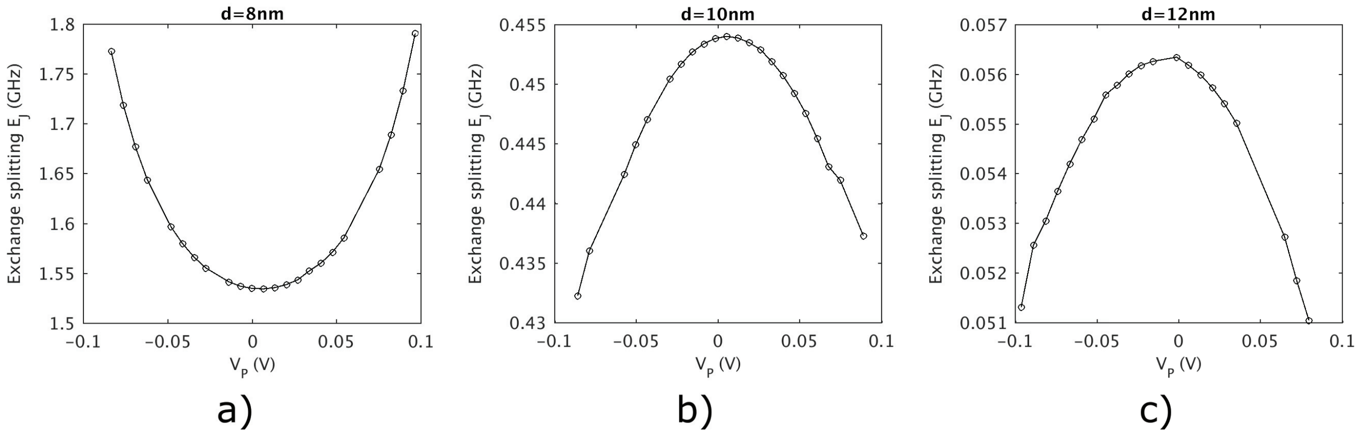

Figure 4.9. a) - c) Exchange splitting vs detuning for different dot separations. All the calculations are done using a gate pitch $p = 36$ nm, Al_2O_3 thickness $t_{Al_2O_3} = 1$ nm and SiO_2 thickness $t_{SiO_2} = 5.9$ nm.

singlet is the so-called (1,1)-(0,2) anti-crossing, where the nature of charge density changes from being in both dots to being in the lower dot. At this anti-crossing, the contributions of both $|S(B, B)$ and $|S(B, A)$ are close to 0.5. This anti-crossing is out of the detuning range plotted currently.

The other two anti-crossings are located on either side of zero detuning, where $|S(B, A)$ mixes with both $|S(B, B)$ and $|S(A, A)$ singlets. Here, the nature of the charge stays in the (1,1) regime. The relative contributions from $|S(B, B)$ and $|S(A, A)$ depends on the orbital splitting, or the energy separation between bonding and anti-bonding orbitals. Increasing the dot separation leads to a reduction in the orbital splitting, and the contributions of $|S(B, B)$ and $|S(A, A)$ become equal close to zero detuning as seen in Fig. 4.8. At zero detuning, this is similar to a H_2 molecule in which the distance between the H atoms is increased such that the wavefunction overlap decreases, and the molecular orbital goes from only having $|S(B, B)$ to having both $|S(B, B)$ and $|S(A, A)$ contributions.

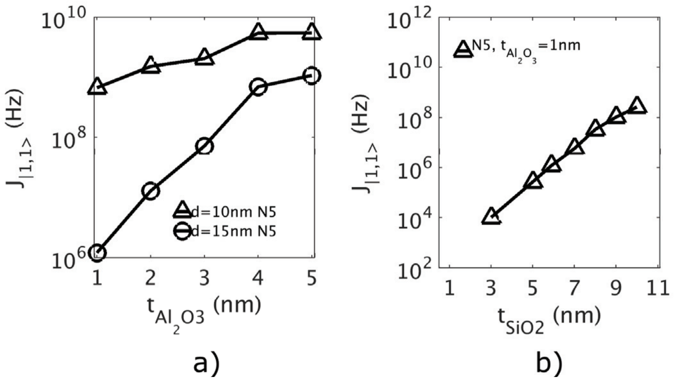

Figure 4.10. Exchange splitting at zero detuning vs SiO_2 and Al_2O_3 oxide thicknesses.

4.3.5 Exchange splitting vs detuning

Exchange splitting is the difference between ground singlet and the zero spin-component triplet: $E_J = E_{T_0} - E_S$. E_J vs detuning for 8-, 10- and 12-nm dot separations is plotted in Fig. 4.9. When the exchange-correlation energy is smaller than the orbital splitting, exchange has been shown to increase monotonously with detuning [54–58]. As can be seen in Fig. 4.9, this is not true when the exchange-correlation energy is much larger than orbital splitting. As the dot separation is increased from 8 to 12 nm, the orbital splitting reduces from ~ 0.8 meV to ~ 0.1 meV, while bonding-anti-bonding exchange-correlation energies reduce from ~ 4.9 meV to ~ 4.2 meV as discussed in Sec. 4.3.3. This causes the exchange splitting to decrease with detuning at 10- and 12-nm dot separations. This property could be useful in two-qubit gate operation when an exchange gate is used for turning the exchange on and off. A small slope of exchange splitting vs detuning would also decrease sensitivity to charge noise.

4.3.6 Exchange splitting vs oxide thicknesses

Fig. 4.10 shows exchange splitting at zero detuning vs SiO_2 and Al_2O_3 oxide thicknesses. The exchange splitting changes by orders of magnitude by changing oxides by just a few nm. This could be used to design devices with exchange splitting in the desired range. The dependence on oxides was modeled by changing the FEM mesh in electrostatic simulations to accommodate the different oxide geometries.

4.4 Summary

Si/SiO_2 based quantum dots are a strong candidate for quantum computing devices due to the long coherence time and advanced fabrication techniques. Exchange splitting between the ground singlet and triplet energy levels of two electrons in tunnel coupled quantum dots is used for two qubit operations. Exchange splitting is an important parameter in two qubit gate speed and coherence. Engineering the exchange splitting by designing devices with better suited gate geometries and oxide thicknesses is necessary, and can be sped up using realistic simulations of the devices.

In this chapter, a modeling technique is developed for the quantum dot based devices which can take the various device parameters such as gate geometry and oxide thickness into consideration while calculating the exchange splitting and two-electron energy spectrum. The electrostatics in these devices is realistically modeled by solving effective-mass Schrödinger and Poisson equations self-consistently. The converged electrostatic potential is then used for calculating atomistic wavefunctions using the empirical tight binding model for taking into account valley splitting, spin-orbit interaction due to surface roughness and the effect of electric field on the Si bands. These atomistic wavefunctions are then used in the full configuration interaction (FCI) to calculate the two-electron energy spectrum, from which exchange splitting can be obtained.

The FCI calculations show that the exchange splitting can decrease with detuning, if the orbital splitting (splitting between bonding and anti-bonding orbitals) is much smaller than the exchange-correlation energy. This wasn't observed before in analytical calculations. The configuration of the ground state singlet was also shown to consist mostly of the bonding-bonding and anti-bonding—anti-bonding singlets. Exchange splitting was shown to vary slowly with detuning as the dot separation is increased, which could be used to design low-noise two-qubit gate architecture. The behavior of exchange splitting with oxide thicknesses shows orders or magnitude of variation in changing the thickness by a few nano-meters, which could be used for device design.

5. SUMMARY AND OUTLOOK

Quantum computing is becoming increasingly important because of its potential in solving complex optimization problems that are currently impossible to solve using classical computers. Several prototype of quantum computers are currently being researched that are based on superconductors, semiconductors, trapped ions, topological collective exitations, optical cavities etc., each having their own benefits. Proposal for topological quantum computers based on quasi-particles in the fractional quantum Hall effect (FQHE) is interesting due to the topological protection of the qubits to noise. Quantum dot based quantum computers are interesting due to their practical applications. Designing these devices can be challenging and time consuming due to the large number of parameters that need to be tuned from fabrication to their operation. Computational modeling of these devices can be helpful in reducing the time required for design. An overview of FQHE based topological and quantum dot based quantum computers was given in Chap. 1.

The devices that could be used in both these types of quantum computers were computationally modeled in this work. The device modeling was guided by the three basic principles: smallest possible number of tunable parameters should be used, results should be comparable to the experiments, and predictions for design improvements should be possible. A framework to model the electrostatics in these devices was developed, so that the underlying physics can be connected to the device parameters. The electrostatic framework takes into account the effect of gates, heterostructures, doping, interface and background impurities, and most importantly the quantum mechanics that dictates the behavior of electrons. A nano-meter precision in regions containing mobile electrons was achieved over micro-meter sized device geometries by using finite element meshes that can be coarsened and refined, such that the computational burden is manageable without affecting the accuracy. An overview of the electrostatic simulation framework was given in Chap. 2.

FQHE based topological qubits are made from two quantum Hall interferometers with a common QPC between them, and two quasi-particles are trapped on an anti-dot in each of the interferometers. The gate operations are performed by sending quasi-particles through the edge states of the interferometers around the quasi-particles trapped on the anti-dots such that their world lines are braided. The quasi-particles moving on the edge states must propagate fast enough so that they maintain coherence while the operation in completed. The coherence could be improved by reducing the interferometer size, and by increasing the edge state velocity of the quasi-particles. An introduction to FQHE based topological qubits is given in Sec. 1.2.1.

A computational study of the edge state velocity of electrons in the integer quantum Hall effect (IQHE) was performed in Chap. 3. It was argued that an increase in electron velocity would also lead to an increase in the quasi-particle velocity. The velocity of electron edge states was found to be $E\ /B$, where E is the expectation value of the electric field for the edge state wavefunction, and B is the magnetic field. The electric field at the edges was also found to be correlated with the sheet density of the 2DEG. Four different structures were studied, and it was found that the double-side doped quantum well structure with trench gates had the highest E for the structures considered, and that it was an order or magnitude larger than E in modulation-doped heterostructure with top gates at certain filling factors. The edge state velocity was also found to be larger and mostly independent of magnetic field, which suggests sharp edges.

This computational framework can be extended in the future to model the edge state velocity of quasi-particles in the Composite Fermion (CF) picture, similar to the analytical work by Chklovskii et al [42]. Coulomb and Aharonov-Bohm oscillations in the interference pattern of quantum Hall interferometers can also be modeled by self-consistently solving quantum transport equations with the Poisson equation.

Si/SiO$_2$ quantum dot based qubits are made by trapping single electrons at the Si/SiO$_2$ interface, each in an electrostatic quantum dot made by applying a positive bias to the gates on top of the dots. A single qubit is made from an electron spin when an external magnetic field is applied, causing the up and down spins to have two different energies. A single qubit gate is made by applying an effectively oscillating magnetic causing Rabi oscillations between up-down spins. Two qubit operations are done by electrostatically coupling electrons in two neighboring dots such that there is a finite exchange splitting in the ground singlet and triplet (T_0) states made from the two spins. An oscillating gate voltage can then be applied to one of the top gates forming the dots so that Rabi oscillations are induced between the singlet and triplet (T_+) states making a CNOT gate. An introduction to Si/SiO$_2$ quantum dot based qubits was given in Sec. 1.2.2.

A computational study of the exchange splitting was performed in Chap. 4. The whole device was electrostatically modeled by considering the effect of top gates, interface charge and oxide thicknesses in a finite element mesh. The self-consistent electrostatic potential thus obtained was used in atomistic tight binding model to consider atomistic effects such as spin-orbit couping, valley splitting due to the electric field and surface roughenss. The one-electron atomistic wavefunctions were then used in full configuration interaction simulations to model the two-electron spectrum and configurations. Quantitative results were obtained for the orbital splitting and exchange-correlation energy of the two electrons in neighboring dots. Exchange splitting was found to change by orders or magnitude when the dot separation and oxide thicknesses were changed by a few nanometers. This result could be particularly useful when designing devices with fast, low noise two qubit operations.

This computational framework could be further extended in the future to model dots in Si/SiGe and GaAs/AlGaAs heterostructures. A local oscillatory magnetic field for addressing a single qubit out of a million qubits may not be possible using ESR lines as is being done currently in experiments. Thus spin qubit operations would have to be performed using the spin-orbit coupling induced by surface roughness in

Si. The physics involved in this operation could be modeled using the tight binding simulations with realistic potentials, a method that was presented in this thesis. A study of charge noise could also be performed by calculating the change in electrostatic environment due to charging and discharging of traps in oxides. Turning the exchange splitting ON and OFF for two-qubit operations and qubit idling respectively will be required in future devices. An exchange coupling gate could be used to achieve this, which would replace the detuning operation currently required for turning ON the exchange splitting. The behavior of exchange splitting in this case can be inferred from the simulations performed in this work.

REFERENCES

REFERENCES

[1] David Law. The Silicon Engine: Timeline (http://www.computerhistory.org/siliconengine/credits/).

[2] T. Mimura. The early history of the high electron mobility transistor (HEMT). *IEEE Transactions on Microwave Theory and Techniques*, 50(3):780–782, 2002.

[3] Xuejue Huang, Wen Chin Lee, Charles Kuo, Digh Hisamoto, Leland Chang, Jakub Kedzierski, Erik Anderson, Hideki Takeuchi, Yang Kyu Choi, Kazuya Asano, Vivek Subramanian, Tsu Jae King, Jeffrey Bokor, and Chenming Hu. Sub-50 nm P-channel FinFET. *IEEE Transactions on Electron Devices*, 48(5):880–886, 2001.

[4] K. V. Klitzing, G. Dorda, and M. Pepper. New method for high-accuracy determination of the fine-structure constant based on quantized hall resistance. *Physical Review Letters*, 45(6):494–497, 1980.

[5] D. C. Tsui, H. L. Stormer, and A. C. Gossard. Two-dimensional magnetotransport in the extreme quantum limit. *Physical Review Letters*, 48(22):1559–1562, 1982.

[6] Pierre Barthelemy and Lieven M K Vandersypen. Quantum Dot Systems: A versatile platform for quantum simulations. *Annalen der Physik*, 525(10-11):808–826, 2013.

[7] Markus Reiher, Nathan Wiebe, Krysta M Svore, Dave Wecker, and Matthias Troyer. Elucidating Reaction Mechanisms on Quantum Computers. *PNAS*, 114(29):7555–7560, 2016.

[8] Matthew S Palsson, Mile Gu, Joseph Ho, Howard M Wiseman, and Geoff J Pryde. Experimentally modeling stochastic processes with less memory by the use of a quantum processor. *Science Advances*, 3:e1601302, 2017.

[9] T. D. Ladd, F. Jelezko, R. Laflamme, Y. Nakamura, C. Monroe, and J. L. O'Brien. Quantum computers. *Nature*, 464(7285):45–53, 2010.

[10] L. M. K. Vandersypen, H. Bluhm, J. S. Clarke, A. S. Dzurak, R. Ishihara, A. Morello, D. J. Reilly, L. R. Schreiber, and M. Veldhorst. Interfacing spin qubits in quantum dots and donors - hot, dense and coherent. *npj Quantum Information*, (December 2016):1–10, 2016.

[11] M. Veldhorst, H. G.J. Eenink, C. H. Yang, and A. S. Dzurak. Silicon CMOS architecture for a spin-based quantum computer. *Nature Communications*, 8(1), 2017.

[12] M. Veldhorst, C. H. Yang, J. C.C. C Hwang, W. Huang, J. P. Dehollain, J. T. Muhonen, S. Simmons, A. Laucht, F. E. Hudson, K. M. Itoh, A. Morello, and A. S. Dzurak. A two-qubit logic gate in silicon. *Nature*, 526(7573):410–414, 10 2015.

[13] R. L. Willett, C. Nayak, K. Shtengel, L. N. Pfeiffer, and K. W. West. Magnetic-field-tuned aharonov-bohm oscillations and evidence for non-abelian anyons at v=5/2. *Physical Review Letters*, 111(18):186401, 2013.

[14] Chetan Nayak, Steven H. Simon, Ady Stern, Michael Freedman, and Sankar Das Sarma. Non-Abelian anyons and topological quantum computation. *Reviews of Modern Physics*, 80(3):1083–1159, 2008.

[15] M. Veldhorst, J. C.C. Hwang, C. H. Yang, A. W. Leenstra, B. De Ronde, J. P. Dehollain, J. T. Muhonen, F. E. Hudson, K. M. Itoh, A. Morello, and A. S. Dzurak. An addressable quantum dot qubit with fault-tolerant control-fidelity. *Nature Nanotechnology*, 9(12):981–985, 2014.

[16] M Veldhorst, C H Yang, J C C Hwang, W Huang, J P Dehollain, J T Muhonen, S Simmons, A Laucht, F E Hudson, K M Itoh, A Morello, and A S Dzurak. A two-qubit logic gate in silicon. *Nature*, 526:410, 10 2015.

[17] Gtz Uhrig. Keeping a Quantum Bit Alive by Optimized π-Pulse Sequences. *Physical Review Letters*, 98:100504, 3 2007.

[18] Wen Yang, Zhen-Yu Wang, and Ren-Bao Liu. Preserving qubit coherence by dynamical decoupling. *Frontiers of Physics*, 6(1):2–14, 9 2010.

[19] F. Jelezko, T. Gaebel, I. Popa, A. Gruber, and J. Wrachtrup. Observation of Coherent Oscillations in a Single Electron Spin. *Physical Review Letters*, 92(7):1–4, 2004.

[20] A.Yu. Kitaev. Fault-tolerant quantum computation by anyons. *Annals of Physics*, 303(1):2–30, 2003.

[21] Christopher M. Dawson and Michael A. Nielsen. The Solovay-Kitaev algorithm. 0(0):1–15, 2005.

[22] Michael A. Nielsen and Isaac L. Chuang. *Quantum Computation and Information*. Cambridge University Press, 2010.

[23] A. G. Fowler, M. Mariantoni, J. M. Martinis, and A. N. Cleland. Surface codes: towards large-scale quantum computation. *Physical Review A*, 86:032324, 2012.

[24] Sankar Das Sarma, Michael Freedman, and Chetan Nayak. Topologically Protected Qubits from a Possible Non-Abelian Fractional Quantum Hall State. *Physical Review Letters*, 94(16):166802, 4 2005.

[25] Michael J. Manfra. Molecular Beam Epitaxy of Ultra-High Quality AlGaAs/GaAs Heterostructures: Enabling Physics in Low-Dimensional Electronic Systems. *Annual Review of Condensed Matter Physics*, 5:347–373, 2014.

[26] J. Weis and K. von Klitzing. Metrology and microscopic picture of the integer quantum Hall effect. *Philosophical Transactions of the Royal Society A: Mathematical, Physical and Engineering Sciences*, 369(1953):3954–3974, 2011.

[27] H.L. Stormer. Two-dimensional electron correlation in high magnetic fields. *Physica B: Condensed Matter*, 177(1-4):401–408, 1992.

[28] R. B. Laughlin. Anomalous quantum Hall effect: An incompressible quantum fluid with fractionally charged excitations. *Physical Review Letters*, 50(18):1395–1398, 1983.

[29] J. K. Jain. Composite-Fermion Approach for the Fractional Quantum Hall Effec. *Physical Review Letters*, 63(2):199–202, 1989.

[30] Jainendra K. Jain. Composite Fermion Theory of Exotic Fractional Quantum Hall Effect. *Annual Review of Condensed Matter Physics*, 6(1):39–62, 2015.

[31] J. K. Jain. *Composite Fermions*. Cambridge University Press, 2007.

[32] P. T. Coleridge, Z. W. Wasilewski, P. Zawadzki, A. S. Sachrajda, and H. A. Carmona. Composite-fermion effective masses. *Physical Review B*, 52(16):603–606, 1995.

[33] H.-S. Sim, K. J. Chang, and G. Ihm. Composite-Fermion Edge States in Fractional Quantum Hall Systems. *Physical Review Letters*, 82(3):596–599, 1999.

[34] Gregory Moore and Nicholas Read. Nonabelions in the fractional quantum hall effect. *Nuclear Physics B*, 360(2-3):362–396, 1991.

[35] Q Qian, J Nakamura, S Fallahi, G C Gardner, J D Watson, S Lüscher, J A Folk, G A Csáthy, and M J Manfra. Quantum lifetime in ultrahigh quality GaAs quantum wells : Relationship to and impact. *Physical Review B (Condensed Matter)*, 96:035309, 2017.

[36] S Baer, C Rössler, E C de Wiljes, P L Ardelt, T Ihn, K Ensslin, C Reichl, and W Wegscheider. Interplay of fractional quantum Hall states and localization in quantum point contacts. *Physical Review B*, 89(8):85424, 2014.

[37] H. van Houten and C. W. J. Beenakker. Quantum Point Contacts. *Physics Today*, 49(July):22, 1996.

[38] Yang Ji, Yunchul Chung, D Sprinzak, M Heiblum, and D Mahalu. An electronic Mach Zehnder interferometer. *Nature*, 422(8):415–418, 2003.

[39] Nissim Ofek, Aveek Bid, Moty Heiblum, Ady Stern, Vladimir Umansky, and Diana Mahalu. Role of interactions in an electronic Fabry-Perot interferometer operating in the quantum Hall effect regime. *Proceedings of the National Academy of Sciences of the United States of America*, 107(12):5276–5281, 2010.

[40] Bertrand I. Halperin, Ady Stern, Izhar Neder, and Bernd Rosenow. Theory of the Fabry-Perot quantum Hall interferometer. *Physical Review B - Condensed Matter and Materials Physics*, 83(15):1–17, 2011.

[41] D. B. Chklovskii, B. I. Shklovskii, and L. I. Glazman. Electrostatics of edge channels. *Physical Review B*, 46(7):4026–4034, 1992.

[42] Dmitri B. Chklovskii. Structure of fractional edge states: A composite-fermion approach. *Physical Review B*, 51(15):9895–9902, 1995.

[43] H.-S. Sim, M. Kataoka, Hangmo Yi, N. Hwang, M.-S. Choi, and S.-R. Yang. Coulomb Blockade and Kondo Effect in a Quantum Hall Antidot. *Physical Review Letters*, 91(26):266801, 2003.

[44] T. F. Watson, S. G. J. Philips, E. Kawakami, D. R. Ward, P. Scarlino, M. Veldhorst, D. E. Savage, M. G. Lagally, Mark Friesen, S. N. Coppersmith, M. A. Eriksson, and L. M. K. Vandersypen. A programmable two-qubit quantum processor in silicon. *Nature Publishing Group*, 555(7698):633–637, 2017.

[45] B. M. Maune, M. G. Borselli, B. Huang, T. D. Ladd, P. W. Deelman, K. S. Holabird, A. A. Kiselev, I. Alvarado-Rodriguez, R. S. Ross, A. E. Schmitz, M. Sokolich, C. A. Watson, M. F. Gyure, and A. T. Hunter. Coherent singlet-triplet oscillations in a silicon-based double quantum dot. *Nature*, 481(7381):344–347, 2012.

[46] Benoit Bertrand, Hanno Flentje, Shintaro Takada, Michihisa Yamamoto, Seigo Tarucha, Arne Ludwig, Andreas D. Wieck, Christopher Bäuerle, and Tristan Meunier. Quantum Manipulation of Two-Electron Spin States in Isolated Double Quantum Dots. *Physical Review Letters*, 115:096801, 2015.

[47] Hendrik Bluhm, Sandra Foletti, Izhar Neder, Mark Rudner, Diana Mahalu, Vladimir Umansky, and Amir Yacoby. Dephasing time of GaAs electron-spin qubits coupled to a nuclear bath exceeding 200 μs. *Nature Physics*, 7:109–113, 12 2010.

[48] Sandra Foletti, Hendrik Bluhm, Diana Mahalu, Vladimir Umansky, and Amir Yacoby. Universal quantum control of two-electron spin quantum bits using dynamic nuclear polarization. *Nature Physics*, 5(12):11, 2010.

[49] Juha T. Muhonen, Juan P. Dehollain, Arne Laucht, Fay E. Hudson, Rachpon Kalra, Takeharu Sekiguchi, Kohei M. Itoh, David N. Jamieson, Jeffrey C. McCallum, Andrew S. Dzurak, and Andrea Morello. Storing quantum information for 30 seconds in a nanoelectronic device. *Nature Nanotechnology*, 9(12):986–991, 2014.

[50] Floris A. Zwanenburg, Andrew S. Dzurak, Andrea Morello, Michelle Y. Simmons, Lloyd C.L. Hollenberg, Gerhard Klimeck, Sven Rogge, Susan N. Coppersmith, and Mark A. Eriksson. Silicon quantum electronics. *Reviews of Modern Physics*, 85(3):961–1019, 2013.

[51] R. Hanson, L. P. Kouwenhoven, J. R. Petta, S. Tarucha, and L. M.K. Vandersypen. Spins in few-electron quantum dots. *Reviews of Modern Physics*, 79(4):1217–1265, 2007.

[52] Charles Kitell. *Introduction to Solid State Physics.* John Wiley and Sons Inc., 8th edition, 1986.

[53] C. H. Yang, A. Rossi, R. Ruskov, N. S. Lai, F. A. Mohiyaddin, S. Lee, C. Tahan, G. Klimeck, A. Morello, and A. S. Dzurak. Spin-valley lifetimes in a silicon quantum dot with tunable valley splitting. *Nature Communications*, 4(May):1–8, 2013.

[54] Dimitrije Stepanenko, Mark Rudner, Bertrand I. Halperin, and Daniel Loss. Singlet-triplet splitting in double quantum dots due to spin-orbit and hyperfine interactions. *Physical Review B - Condensed Matter and Materials Physics*, 85(7):075416, 2012.

[55] Xuedong Hu and S. Das Sarma. Hilbert-space structure of a solid-state quantum computer: Two-electron states of a double-quantum-dot artificial molecule. *Physical Review A - Atomic, Molecular, and Optical Physics*, 61(6):19, 2000.

[56] Guido Burkard, Daniel Loss, and David P. DiVincenzo. Coupled quantum dots as quantum gates. *Physical Review B*, 59(3):2070–2078, 1999.

[57] Qiuzi Li, Lukasz Cywinski, Dimitrie Culcer, Xuedong Hu, and S. Das Sarma. Exchange coupling in silicon quantum dots: Theoretical considerations for quantum computation. pages 1–17, 2009.

[58] Zack White and Guy Ramon. Extended orbital modeling of spin qubits in double quantum dots. 045306(January):1–13, 2017.

[59] Rajib Rahman, Erik Nielsen, Richard P. Muller, and Malcolm S. Carroll. Voltage controlled exchange energies of a two-electron silicon double quantum dot with and without charge defects in the dielectric. *Physical Review B - Condensed Matter and Materials Physics*, 85(12):1–6, 2012.

[60] Rifat Ferdous, Erika Kawakami, Pasquale Scarlino, Micha P. Nowak, D. R. Ward, D. E. Savage, M. G. Lagally, S. N. Coppersmith, Mark Friesen, Mark A. Eriksson, Lieven M. K. Vandersypen, and Rajib Rahman. Valley dependent anisotropic spin splitting in silicon quantum dots. (June 2017), 2017.

[61] Rifat Ferdous, Kok W Chan, Menno Veldhorst, J C C Hwang, C H Yang, Harshad Sahasrabudhe, Gerhard Klimeck, Andrea Morello, Andrew S Dzurak, and Rajib Rahman. Interface-induced spin-orbit interaction in silicon quantum dots and prospects for scalability. *Physical Review B*, 241401:1–5, 2018.

[62] E. Kawakami, T. Jullien, P. Scarlino, D. R. Ward, D. E. Savage, M. G. Lagally, V. V. Dobrovitski, Mark Friesen, S. N. Coppersmith, M. A. Eriksson, and L. M. K. Vandersypen. Gate fidelity and coherence of an electron spin in a Si/SiGe quantum dot with micromagnet. *Proceedings of the National Academy of Sciences of the United States of America*, 113(42):11738, 2016.

[63] John M. Nichol, Lucas A. Orona, Shannon P. Harvey, Saeed Fallahi, Geoffrey C. Gardner, Michael J. Manfra, and Amir Yacoby. High-fidelity entangling gate for double-quantum-dot spin qubits. *npj Quantum Information*, 3(1):1–4, 2017.

[64] A Siddiki and F Marquardt. Self-consistent calculation of the electron distribution near a quantum point contact in the integer quantum Hall effect. *Physical Review B - Condensed Matter and Materials Physics*, 75:045325, 2007.

[65] Afif Siddiki and Rolf R. Gerhardts. Incompressible strips in dissipative Hall bars as origin of quantized Hall plateaus. *Physical Review B - Condensed Matter and Materials Physics*, 70(19):195335, 2004.

[66] A. Siddiki, A. E. Kavruk, T. Öztürk, Atav, M. Şahin, and T. Hakiolu. The self-consistent calculation of the edge states at quantum Hall effect (QHE) based Mach-Zehnder interferometers (MZI). *Physica E: Low-Dimensional Systems and Nanostructures*, 40(5):1398–1400, 2008.

[67] Frank Stern and Sankar DasSarma. Electron energy levels in GaAs-Ga1-xAlxAs heterojunctions. *Physical Review B*, 30(2):840–848, 1984.

[68] Xujiao Gao, Erik Nielsen, Richard P. Muller, Ralph W. Young, Andrew G. Salinger, Nathan C. Bishop, Michael P. Lilly, and Malcolm S. Carroll. QCAD Simulation and Optimization of Semiconductor Quantum Dots. (April):1–20, 3 2014.

[69] D. J. BenDaniel and C. B. Duke. Space-Charge Effects on Electron Tunneling. *Phys. Rev.*, 152(2):683, 1966.

[70] L Hedin and BI Lundqvist. Explicit local exchange-correlation potentials. *Journal of Physics C: Solid state physics*, 4:2064, 1971.

[71] D Vasileska, M N Wybourne, S M Goodnick, and A D Gunther. 3D simulation of GaAs/AlGaAs quantum dot point contact structures. *Semicond. Sci. Technol. A37 Semicond. Sci. Technol*, 13(1398):A37–A40, 1998.

[72] S. M. Sze and Kwok K. Ng. *Physics of Semiconductor Devices.* John Wiley and Sons Ltd., 3 edition, 2007.

[73] Carl W. Wilmsen. *Physics and chemistry of III-V compound semiconductor interfaces.* Plemnum press, 1985.

[74] G Fiori, G Iannaccone, and M Macucci. Modeling of Shallow Quantum Point Contacts Defined on AlGaAs / GaAs Heterostructures : The Effect of Surface States. *Journal of Computational Electronics*, 1(1):39–42, 2002.

[75] M. G. Pala, G. Iannaccone, S. Kaiser, A. Schliemann, L. Worschech, and A. Forchel. Extraction of parameters of surface states from experimental test structures. *Nanotechnology*, 13(3):373–377, 2002.

[76] Minhan Chen, Wolfgang Porod, and David J. Kirkner. Coupled finite element/boundary element method for semiconductor quantum devices with exposed surfaces. *Journal of Applied Physics*, 75(5):2545–2554, 1994.

[77] Gilbert Strang and George Fix. *An Analysis of the Finite Element Method.* 1973.

[78] Benjamin S. Kirk, John W. Peterson, Roy H. Stogner, and Graham F. Carey. libMesh : a C++ library for parallel adaptive mesh refinement/coarsening simulations. *Engineering with Computers*, 22(3-4):237–254, 11 2006.

[79] Christophe Geuzaine and Jean Franois Remacle. Gmsh: A 3-D finite element mesh generator with built-in pre- and post-processing facilities. *International Journal for Numerical Methods in Engineering*, 79(11):1309–1331, 2009.

[80] Geoffrey C. Gardner, John D. Watson, Sumit Mondal, Nianpei Deng, Gabor a. Csathy, and Michael J. Manfra. Growth and electrical characterization of Al0.24Ga0.76As/AlxGa1xAs/Al0.24Ga0.76As modulation-doped quantum wells with extremely low x. *Applied Physics Letters*, 102(2013):252103, 2013.

[81] Vicente Hernandez, Jose E Roman, and Vicente Vidal. SLEPc. *ACM Trans. Math. Softw.*, 31(3):351–362, 2005.

[82] V Hernandez, J E Roman, and V Vidal. {SLEPc}: {S}calable {L}ibrary for {E}igenvalue {P}roblem {C}omputations. *Lecture Notes in Computer Science*, 2565:377–391, 2003.

[83] Satish Balay, Shrirang Abhyankar, Mark F. Adams, Jed Brown, Peter Brune, Kris Buschelman, Lisandro Dalcin, Victor Eijkhout, William D. Gropp, Dinesh Kaushik, Matthew G. Knepley, Lois Curfman McInnes, Karl Rupp, Barry F. Smith, Stefano Zampini, and Hong Zhang. {PETS}c Users Manual. Technical Report ANL-95/11 - Revision 3.6, Argonne National Laboratory, 2015.

[84] Satish Balay, Shrirang Abhyankar, Mark F. Adams, Jed Brown, Peter Brune, Kris Buschelman, Lisandro Dalcin, Victor Eijkhout, William D. Gropp, Dinesh Kaushik, Matthew G. Knepley, Lois Curfman McInnes, Karl Rupp, Barry F. Smith, Stefano Zampini, and Hong Zhang. {PETS}c {W}eb page. \url{http://www.mcs.anl.gov/petsc}, 2015.

[85] H. Sahasrabudhe, B. Novakovic, J. Nakamura, S. Fallahi, M. Povolotskyi, G. Klimeck, R. Rahman, and M. J. Manfra. Optimization of edge state velocity in the integer quantum Hall regime. *Physical Review B*, 97(8):085302, 2018.

[86] Itamar Gurman, Ron Sabo, Moty Heiblum, Vladimir Umansky, and Diana Mahalu. Dephasing of an electronic two-path interferometer. *Physical Review B - Condensed Matter and Materials Physics*, 93(12):121412, 2016.

[87] R. L. Willett, L. N. Pfeiffer, and K. W. West. Alternation and interchange of e/4 and e/2 period interference oscillations consistent with filling factor 5/2 non-Abelian quasiparticles. *Physical Review B*, 82(20):205301, 11 2010.

[88] D. T. McClure, Yiming Zhang, B. Rosenow, E. M. Levenson-Falk, C. M. Marcus, L. N. Pfeiffer, and K. W. West. Edge-state velocity and coherence in a quantum hall Fabry-P??rot interferometer. *Physical Review Letters*, 103(20):206806, 2009.

[89] C. L. Kane, Matthew P. A. Fisher, and J. Polchinski. Randomness at the Edge: Theory of Quantum Hall Transport at Filling v=2/3. *Physical Review Letters*, 72(26):4129–4132, 1994.

[90] Xin Wan, Kun Yang, and E. H. Rezayi. Reconstruction of fractional quantum Hall edges. *Physical Review Letters*, 88(5):056802, 2002.

[91] Aveek Bid, N. Ofek, H. Inoue, M. Heiblum, C. L. Kane, V. Umansky, and D. Mahalu. Observation of neutral modes in the fractional quantum Hall effect regime. *AIP Conference Proceedings*, 1399(7306):633–634, 2011.

[92] Hiroyuki Inoue, Anna Grivnin, Yuval Ronen, Moty Heiblum, Vladimir Umansky, and Diana Mahalu. Proliferation of neutral modes in fractional quantum Hall states. *Nature communications*, 5(May):4067, 2014.

[93] Moshe Goldstein and Yuval Gefen. Suppression of interference in quantum Hall Mach-Zehnder geometry by upstream neutral modes. *Physical Review Letters*, 117(December):276804, 2016.

[94] Ki Hoon Lee, Zi Xiang Hu, and Xin Wan. Construction of edge states in fractional quantum Hall systems by Jack polynomials. *Physical Review B - Condensed Matter and Materials Physics*, 89(16):165124, 2014.

[95] Zi Xiang Hu, E. H. Rezayi, Xin Wan, and Kun Yang. Edge-mode velocities and thermal coherence of quantum Hall interferometers. *Physical Review B - Condensed Matter and Materials Physics*, 80(23):235330, 2009.

[96] M. Kataoka, N. Johnson, C. Emary, P. See, J. P. Griffiths, G. A C Jones, I. Farrer, D. A. Ritchie, M. Pepper, and T. J B M Janssen. Time-of-Flight Measurements of Single-Electron Wave Packets in Quantum Hall Edge States. *Physical Review Letters*, 116(12):126803, 2016.

[97] H. Kamata, T. Ota, K. Muraki, and T. Fujisawa. Voltage-controlled group velocity of edge magnetoplasmon in the quantum Hall regime. *Physical Review B - Condensed Matter and Materials Physics*, 81(8):085329, 2010.

[98] N. Kumada, H. Kamata, and T. Fujisawa. Edge magnetoplasmon transport in gated and ungated quantum Hall systems. *Physical Review B - Condensed Matter and Materials Physics*, 84(4):045314, 2011.

[99] S. Birner, S. Hackenbuchner, M. Sabathil, G. Zandler, J. a. Majewski, T. Andlauer, T. Zibold, R. Morschl, a. Trellakis, and P. Vogl. Modeling of semiconductor nanostructures with nextnano3. *Acta Physica Polonica A*, 110(2):111–124, 2006.

[100] S. Arslan, E. Cicek, D. Eksi, S. Aktas, A. Weichselbaum, and A. Siddiki. Modeling of quantum point contacts in high magnetic fields and with current bias outside the linear response regime. *Physical Review B - Condensed Matter and Materials Physics*, 78(12):125423, 2008.

[101] K. Panos, R. R. Gerhardts, J. Weis, and K. Von Klitzing. Current distribution and Hall potential landscape towards breakdown of the quantum Hall effect: A scanning force microscopy investigation. *New Journal of Physics*, 16, 2014.

[102] G Fiori, G Iannaccone, M Macucci, S Reitzenstein, S Kaiser, M Kesselring, L Worschech, and A Forchel. Experimental and theoretical investigation of quantum point contacts for the validation of models for surface states. *Nanotechnology*, 13(3):299–303, 2002.

[103] D Eksi, O Kilicoglu, O Goktas, and A Siddiki. Screening model of metallic nonideal contacts at integer quantized Hall regime. *Physical Review B*, 82:165308, 2010.

[104] Sebastian Steiger, Michael Povolotskyi, Hong Hyun Park, Tillmann Kubis, and Gerhard Klimeck. NEMO5: A parallel multiscale nanoelectronics modeling tool. *IEEE Transactions on Nanotechnology*, 10(6):1464–1474, 2011.

[105] M. Stopa. Quantum dot self-consistent electronic structure and the Coulomb blockade. *Physical Review B*, 54(19):13767–13783, 11 1996.

[106] Christoph W. Groth, Michael Wimmer, Anton R. Akhmerov, and Xavier Waintal. Kwant: A software package for quantum transport. *New Journal of Physics*, 16, 2014.

[107] F E Camino, Wei Zhou, and V J Goldman. Quantum transport in electron Fabry-Perot interferometers. *Physical Review B*, 76(October):155305, 2007.

[108] A. Trellakis, A. T. Galick, A. Pacelli, and U. Ravaioli. Iteration scheme for the solution of the two-dimensional Schrodinger-Poisson equations in quantum structures. *Journal of Applied Physics*, 81(12):7880, 1997.

[109] E. F. Schubert and K. Ploog. Shallow and deep donors in direct-gap n-AlGaAs-Si grown by MBE. *Physical Review B*, 30(12):7021–7029, 1984.

[110] D. J. Chadi and K. J. Chang. Energetics of DX-center formation in GaAs and AlxGa1-xAs alloys. *Physical Review B*, 39(14):10063–10074, 1989.

[111] G Iannaccone, M Macucci, E Amirante, Y Jin, H Lanois, and C Vieu. Tuning of surface boundary conditions for the 3D simulation of gated heterostructures. *Superlattices and Microstructures*, 27(5-6):369–372, 2000.

[112] John H Davies, Ivan a. Larkin, and E. V. Sukhorukov. Modeling the patterned two-dimensional electron gas: Electrostatics. *Journal of Applied Physics*, 77(9):4504–4512, 1995.

[113] Tarek A Ameen, Hesameddin Ilatikhameneh, Jun Z Huang, Michael Povolotskyi, Rajib Rahman, and Gerhard Klimeck. Combination of Equilibrium and Nonequilibrium Carrier Statistics Into an Atomistic Quantum Transport Model for Tunneling Heterojunctions. *IEEE Transactions on Electron Devices*, 64(6):2512–2518, 2017.

[114] Kaan Güven and Rolf R. Gerhardts. Self-consistent local equilibrium model for density profile and distribution of dissipative currents in a Hall bar under strong magnetic fields. *Physical Review B*, 67(11):115327, 2003.

[115] Rolf R. Gerhardts. The effect of screening on current distribution and conductance quantisation in narrow quantum Hall systems. *Physica Status Solidi (B) Basic Research*, 245(2):378–392, 2008.

[116] R L Willett, L N Pfeiffer, and K W West. Measurement of filling factor 5/2 quasiparticle interference with observation of charge e/4 and e/2 period oscillations. *Proceedings of the National Academy of Sciences*, 106(22):8853–8858, 2009.

[117] Tsai-Yu Huang, Chi-Te Liang, Yang Fang Chen, Michelle Y Simmons, Gil-Ho Kim, and David a Ritchie. Direct measurement of the spin gaps in a gated GaAs two-dimensional electron gas. *Nanoscale research letters*, 8(1):138, 2013.

[118] G. Bilgeç, H. Üstünel Toffoli, A. Siddiki, and I. Sokmen. The self-consistent calculation of exchange enhanced odd integer quantized Hall plateaus within Thomas-Fermi-Dirac approximation. *Physica E: Low-Dimensional Systems and Nanostructures*, 42(4):1058–1061, 2010.

[119] Christophe Geuzaine and Jean-Francois Remacle. Gmsh : A 3-D finite element mesh generator with built-in pre- and post-processing facilities. *International Journal for Numerical Methods in Engineering*, 79(May):1309–1331, 2009.

[120] Vicente Hernandez, Jose E Roman, and Vicente Vidal. {SLEPc}: A Scalable and Flexible Toolkit for the Solution of Eigenvalue Problems. *{ACM} Trans. Math. Software*, 31(3):351–362, 2005.

[121] Supriyo Datta. *Electronic Transport in Mesoscopic Systems.* Cambridge University Press, 5 edition, 1995.

[122] Roger Lake, Gerhard Klimeck, R. Chris Bowen, and Dejan Jovanovic. Single and multiband modeling of quantum electron transport through layered semiconductor devices. *Journal of Applied Physics*, 81(12):7845, 1997.

[123] Craig S. Lent and David J. Kirkner. The quantum transmitting boundary method. *Journal of Applied Physics*, 67(10):6353–6359, 1990.

[124] Timothy B. Boykin, Gerhard Klimeck, and Fabiano Oyafuso. Valence band effective-mass expressions in the sp3d5s* empirical tight-binding model applied to a Si and Ge parametrization. *Physical Review B - Condensed Matter and Materials Physics*, 69(11):1–10, 2004.

[125] J. C. Slater and G. F. Koster. Simplified LCAO method for the periodic potential problem. *Physical Review*, 94(6):1498–1524, 1954.

[126] Gerhard Klimeck, Shaikh Ahmed, Neerav Kharche, Hansang Bae, Steve Clark, Benjamin Haley, Sunhee Lee, Maxim Naumov, Hoon Ryu, Faisal Saied, Marta Prada, Marek Korkusinski, and Timothy B Boykin. Atomistic Simulation of Realistically Sized Nanodevices Using NEMO 3-D : Part I Models and Benchmarks. *Computer Engineering*, 54(1):1–38, 2007.

[127] Johann Sée, Philippe Dollfus, and Sylvie Galdin. Comparison between a sp3d5 tight-binding and an effective-mass description of silicon quantum dots. *Physical Review B*, 66(19):193307, 2002.

[128] Archana Tankasala, Joseph Salfi, Juanita Bocquel, Benoit Voisin, Muhammad Usman, Gerhard Klimeck, Michelle Y. Simmons, Lloyd C.L. Hollenberg, Sven Rogge, and Rajib Rahman. Two-electron states of a group-V donor in silicon from atomistic full configuration interactions. *Physical Review B*, 97(19):1–7, 2018.

[129] Frank Stern. Iteration methods for calculating self-consistent fields in semiconductor inversion layers. *Journal of Computational Physics*, 6(1):56–67, 1970.

[130] Satish Balay, William D. Gropp, Lois Curfman McInnes, and Barry F. Smith. *Efficient Management of Parallelism in Object Oriented Numerical Software Libraries.* Birkhäuser press, 1997.

[131] Steven E. Laux and Frank Stern. Electron states in narrow gate-induced channels in Si. *Applied Physics Letters*, 49(2):91–93, 1986.

[132] C. Moglestue. Self-consistent calculation of electron and hole inversion charges at silicon-silicon dioxide interfaces. *Journal of Applied Physics*, 59(9):3175–3183, 1986.

[133] J. Sune, P. Olivo, and B. Ricco. Self-consistent solution of the Poisson and Schr??dinger equations in accumulated semiconductor-insulator interfaces. *Journal of Applied Physics*, 70(1):337–345, 1991.

[134] R E Bank and D J Rose. Parameter selection for Newton-like methods applicable to non-linear partial differential equations. 17(6):806–822, 1980.

APPENDICES

A. WEAK FORMULATION OF SCHRÖDINGER AND POISSON EQUATIONS

In this chapter, the FEM weak formulation of Schrödinger (Eq. 2.1) and Poisson (Eq. 2.9) equations is derived.

Schrödinger equation

The 3D EM Schrödinger equation 2.1 is discretized over a volume Ω with surface Γ. The wavefunction of this equation is assumed to be completely confined within the volume V such that its derivative at the surface Γ is zero

$$\nabla\psi(\mathbf{r}).\hat{\mathbf{n}} = 0,\ \ \hat{\mathbf{n}} \perp \Gamma \tag{A.1}$$

Equation 2.1 is multiplied with an arbitrary smooth function $\nu(\mathbf{r})$.

$$-\frac{\hbar^2}{2}\nabla.\quad \frac{1}{m^*(\mathbf{r})}\nabla\psi(\mathbf{r})\quad \nu(\mathbf{r}) + V_{tot}(\mathbf{r})\psi(\mathbf{r})\nu(\mathbf{r}) = E\psi(\mathbf{r})\nu(\mathbf{r})$$

Integrating over the volume Ω

$$-\frac{\hbar^2}{2}\quad \nabla.\quad \frac{1}{m^*(\mathbf{r})}\nabla\psi(\mathbf{r})\quad \nu(\mathbf{r})\,d\Omega + \quad V_{tot}(\mathbf{r})\psi(\mathbf{r})\nu(\mathbf{r})\,d\Omega = \quad E\psi(\mathbf{r})\nu(\mathbf{r})\,d\Omega$$

Assuming the gradient of effective mass to be zero and expanding the first integral using integration by parts

$$\begin{aligned}-\frac{\hbar^2}{2}\quad & \nabla.\quad \nu(\mathbf{r})\frac{1}{m^*(\mathbf{r})}\nabla\psi(\mathbf{r})\quad d\Omega - \quad \frac{1}{m^*(\mathbf{r})}\nabla\nu(\mathbf{r}).\nabla\psi(\mathbf{r})\,d\Omega \\ & + \quad V_{tot}(\mathbf{r})\psi(\mathbf{r})\nu(\mathbf{r})\,d\Omega = \quad E\psi(\mathbf{r})\nu(\mathbf{r})\,d\Omega\end{aligned}$$

The assumption of a zero effective mass gradient is valid because it only changes at the interface of two different materials and its derivative is a delta function at the interface. As flux is conserved at the element boundaries, a delta function derivative of effective mass will not have a considerable effect on the wavefuntion. Using divergence theorem, the first integral is converted into a surface integral which is zero due to the wavefunction vanishing at the boundary

$$\nabla. \quad \nu(\mathbf{r})\frac{1}{m^*(\mathbf{r})}\nabla\psi(\mathbf{r}) \quad d\Omega = \quad \nu(\mathbf{r})\frac{1}{m^*(\mathbf{r})}\nabla\psi(\mathbf{r}).\hat{\mathbf{n}}\, d\Gamma = 0$$

Thus the equation reduces to it's weak form

$$\frac{\hbar^2}{2} \quad \frac{1}{m^*(\mathbf{r})}\nabla\nu(\mathbf{r}).\nabla\psi(\mathbf{r})\, d\Omega + \quad V_{tot}(\mathbf{r})\psi(\mathbf{r})\nu(\mathbf{r})\, d\Omega = \quad E\psi(\mathbf{r})\nu(\mathbf{r})\, d\Omega \tag{A.2}$$

Applying Galerkin's method to approximate the wavefunction ψ and the arbitrary function ν

$$\psi(\mathbf{r}) = \underset{i}{\quad} \psi_i\varphi_i(\mathbf{r}),\ \nu(\mathbf{r}) = \underset{i}{\quad} \nu_i\varphi_i(\mathbf{r})$$

where ψ_i and ν_i are the coefficients of i^{th} FEM basis function $\varphi_i(\mathbf{r})$. Substituting this in the weak form gives us

$$\begin{aligned} \underset{i,j}{\quad} \psi_i\nu_j \ \frac{\hbar^2}{2} \quad \frac{\nabla\varphi_i(\mathbf{r}).\nabla\varphi_j(\mathbf{r})}{m^*(\mathbf{r})}\, d\Omega + \quad V_{tot}(\mathbf{r})\varphi_i(\mathbf{r})\varphi_j(\mathbf{r})\, d\Omega \\ = \underset{i,j}{\quad} \psi_i\nu_j E \quad \varphi_i(\mathbf{r})\varphi_j(\mathbf{r})\, d\Omega \end{aligned}$$

Since ν is an arbitrary function, we can drop it from the equation. Then the equation becomes a matrix equation

$$\begin{aligned} K_{ij}\psi_i &= EM_{ij}\psi_i, \\ K_{ij} &= \frac{\hbar^2}{2} \quad \frac{\nabla\varphi_i(\mathbf{r}).\nabla\varphi_j(\mathbf{r})}{m^*(\mathbf{r})}\, d\Omega + \quad V_{tot}(\mathbf{r})\varphi_i(\mathbf{r})\varphi_j(\mathbf{r})\, d\Omega, \\ M_{ij} &= E \quad \varphi_i(\mathbf{r})\varphi_j(\mathbf{r})\, d\Omega \end{aligned} \tag{A.3}$$

K_{ij} matrix is the stiffness matrix and M_{ij} is the mass or S matrix. Since the basis functions only span the elements surrounding a node, the integrals are performed over each element with basis functions from surrounding nodes. This gives us overlaps only on the nearest neighbor nodes thus making the stiffness and S matrices sparse. Having these matrices sparse is important because it reduces matrix operation cost. The integrals are performed using Gaussian or Trapezoidal quadratures. Trapezoidal quadrature gives us a diagonal S matrix, which improves the scaling of Eigenvalue problem.

Poisson equation

The weak form of Poisson equation (Eq. 2.9) is derived in a way similar to the Schrödinger equation. Eq. 2.9 is multiplied by an arbitrary function $\nu(\mathbf{r})$ and integrated over volume Ω

$$- \quad \nabla.\,(\ {}_0\ {}_r(\mathbf{r})\nabla V(\mathbf{r}))\,\nu(\mathbf{r})\,d\Omega = \quad \rho(\mathbf{r})\nu(\mathbf{r})\,d\Omega$$

It is assumed that the gradient of the dielectric constant is zero, which is true inside a material and untrue at a material interface. Integrating by parts and using the divergence theorem, gives the weak form of the equation

$$\nabla\nu(\mathbf{r}).\nabla V(\mathbf{r})\ {}_0\ {}_r(\mathbf{r})\,d\Omega - \quad \nu(\mathbf{r})\ {}_0\ {}_r(\mathbf{r})\nabla V(\mathbf{r}).\hat{\mathbf{n}}\,d\Gamma = \quad \rho(\mathbf{r})\nu(\mathbf{r})\,d\Omega \qquad \text{(A.4)}$$

Applying the Galerkin approximation

$$V(\mathbf{r}) = \underset{i}{\ } V_i\varphi_i(\mathbf{r}),\ \nu(\mathbf{r}) = \underset{i}{\ } \nu_i\varphi_i(\mathbf{r})$$

and eliminating the arbitrary function ν gives the linear matrix equation

$$
\begin{aligned}
K_{ij}V_i &= B_j, \\
K_{ij} &= \quad \nabla\varphi_i(\mathbf{r}).\nabla\varphi_j(\mathbf{r})\ {}_r(\mathbf{r})\,d\Omega - \quad \varphi_j(\mathbf{r})\ {}_r(\mathbf{r})\nabla\varphi_i(\mathbf{r}).\hat{\mathbf{n}}\,d\Gamma \\
B_j &= \frac{4\pi}{{}_0} \quad \rho(\mathbf{r})\varphi_j(\mathbf{r})\,d\Omega
\end{aligned}
\tag{A.5}
$$

This equation can be either linear or non-linear depending the form of charge density. For a fixed charge density, Eq. A.5 becomes a linear equation. For charge density that is potential dependent, it is a non-linear equation which can be solved iteratively.

B. BOUNDARY CONDITIONS FOR THE POISSON EQUATION

Boundary conditions (BCs) are used to model the effects of surface charges and gates. Surface charges and external electric fields can be incorporated using the Neumann boundary condition. Mixed or Robin boundary conditions can also be used for surface charges when a voltage is also specified at the boundary. Dirichlet boundary conditions are used for setting the electrostatic potential at a boundary.

Dirichlet boundary conditions

Dirichlet BC is set in FEM for a surface node i by setting the elements of the stiffness matrix of Poisson equation (Eq. A.5) as follows

$$K_{ij} = \begin{cases} 1, & i = j \\ 0, & i = j \end{cases}, \ B_i = V_0 \tag{B.1}$$

where V_0 is the value of the electrostatic potential at the surface.

Neumann boundary conditions

In Neumann type boundary condition, the derivative of the potential (or the electric field) perpendicular to surface is specified. This can be included in the matrix form for a surface node i and any j in the following way

$$\begin{aligned} K_{ij} &= \quad \nabla\varphi_i(\mathbf{r}).\nabla\varphi_j(\mathbf{r}) \ {}_0 \ {}_r(\mathbf{r})\, d\Omega \\ B_i &= \quad \varphi_i(\mathbf{r}) \ {}_0 \ {}_r(\mathbf{r})\mathbf{E}_0.\hat{\mathbf{n}}\, d\Gamma\, d\Omega \end{aligned} \tag{B.2}$$

where E_0 is the electric field to be specified on the surface. If the potential drops just inside the boundary, the electric field at the boundary is positive.

Mixed or Robin boundary conditions

In some cases when a gate has a high bias, charge accumulates under the gate because of either conduction band going below, or valence band going above the Fermi level. In such cases, it is better to specify the charge using a boundary condition rather than solving it in the 3D domain, which will require very fine elements near the surface. For boundaries with surface charge under the gate, the gate electrostatic potential and jump in flux due to the charge needs to be specified. This can be done using Robin or mixed boundary condition.

For a mixed boundary condition, a point some distance d away from the surface is assumed to be at the fixed electrostatic potential V_0. Derivation of this equation is done in [68]. The potential on the actual surface is still floating (obtained after solving the linear equation). Lets assume a surface charge σ_0 stuck to the surface. The electric field will then jump by a value $q\sigma_0/\epsilon$. This can be written in a mathematical form as follows

$$\nabla V.\hat{\mathbf{n}} = \underset{j}{} V_j\nabla\varphi_j.\hat{\mathbf{n}} = \frac{V_0 - V}{d} - q\sigma_0 = \frac{V_0 - {}_{j} V_j\varphi_j}{d} - q\sigma_0 \tag{B.3}$$

where $\hat{\mathbf{n}}$ is the direction perpendicular to the surface Γ at the face of the element. This can be substituted in Eq. A.5 by replacing ${}_{j} V_j\nabla\varphi_j.\hat{\mathbf{n}}$ in the surface part of K_{ij}. This gives the following forms for K_{ij} and B_j for a mixed boundary condition

$$\begin{aligned} K_{ij} &= \quad \nabla\varphi_i(\mathbf{r}).\nabla\varphi_j(\mathbf{r}) \ {}_{0}\ {}_{r}(\mathbf{r})\, d\Omega + \quad \frac{{}_{0}\ {}_{r}(\mathbf{r})}{d}\varphi_i(\mathbf{r})\varphi_j(\mathbf{r})\, d\Gamma \\ B_j &= \quad \varphi_j \quad {}_{0}\ {}_{r}(\mathbf{r})\frac{V_0}{d} - d\sigma_0 \quad d\Gamma \end{aligned} \tag{B.4}$$

C. NEWTON'S METHOD FOR ITERATIVELY SOLVING THE SCHRÖDINGER-POISSON EQUATIONS

The Newton's method works to minimize a function by successively calculating corrections to the variable calculated using linear extrapolation. A very simple example of a Newton iteration with a function of 1 variable is show in Fig. C.1.

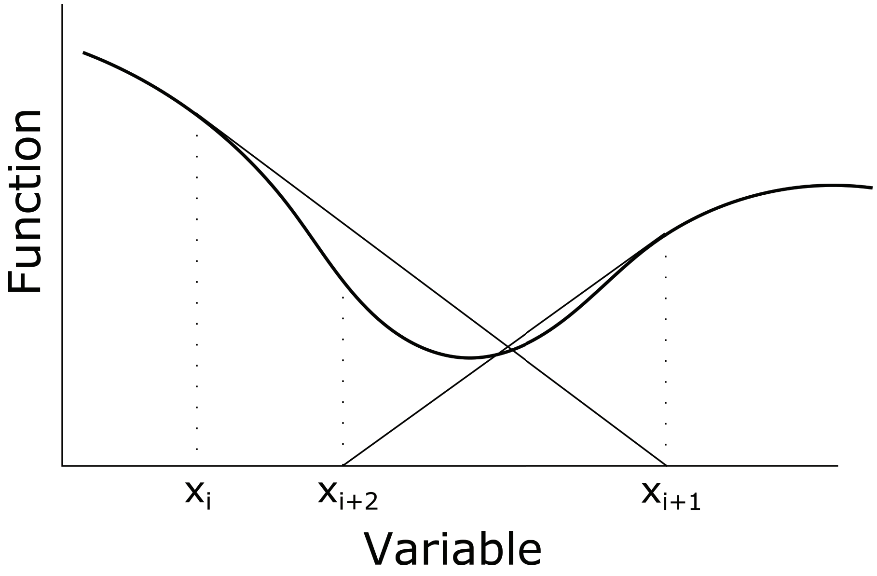

Figure C.1. An example of a Newton iteration with 1 function and 1 variable.

At each iteration, the slope of the function with respect to the variable is calculated. This slope is the Jacobian when we have multiple functions with multiple variables. When discretizing the Poisson equation (Eq. A.5), the function of the Poisson equation is written as

$$F_i = K_{ij} V_j - B_i$$

where K_{ij} B_i are as described in Eq. A.5. To solve the Poisson equation, the Euclidean norm of function F is minimized. A measure of the degree to which the equation is solved is the Euclidean norm of the function, also know as the residual and denoted by $||F||_2$.

For a given potential V_i^n at point i in the n^{th} iteration, the potential in $n + 1^{th}$ iteration can be found by linear extrapolation. For this, the slope of the functions with respect to each variable has to be calculated. This slope is called the Jacobian J_{ij}

$$V_i^{n+1} = V_i^n - J_{ij}^{-1} F_j \tag{C.1}$$

The Jacobian of the Poisson equation is calculated by differentiating the function at point i with respect to potential at point j.

$$J_{ij} = \frac{\partial F_i}{V_j} = K_{ij} - \frac{\partial B_i}{\partial V_j} \tag{C.2}$$

When differentiating the right hand side of Poisson equation (Eq. A.5), the derivative of charge density with respect to the potential is required

$$\frac{\partial B_i}{\partial V_j} = \quad \frac{\partial \rho(\mathbf{r})}{\partial V_j} \varphi_j(\mathbf{r}) \, d\Omega$$

This derivative is evaluated by observing that the position dependent conduction band edge depends on the potential $E_C(\mathbf{r}) = E_C - qV$. Thus, differentiating the quantum electron density (2.3) gives the following expressions for no periodicity (0-dimensional for QDs), periodicity in 1 dimension (QPCs) and 2 dimensions (2DEG)

$$\begin{aligned} \frac{\partial n(\mathbf{r})}{\partial V(\mathbf{r})} &\approx \underset{i}{\quad} \frac{\partial N_i(\mathbf{r})}{\partial V_i} \psi_i(\mathbf{r}), \\ \frac{\partial N_i(\mathbf{r})}{\partial V_i(\mathbf{r})} &= \begin{cases} \frac{g_v g_s q}{kT} \frac{\exp((E_i - E_F)/kT)}{[1 + \exp((E_i - E_F)/kT)]^2}, & 0 - D \\ g_v \frac{q m_t^*(\mathbf{r})}{\pi \hbar^2} \frac{\exp\left(\frac{E_F - E_i}{kT}\right)}{1 + \exp\left(\frac{E_F - E_i}{kT}\right)}, & 1 - D \\ g_v \frac{2 q m_t^*(\mathbf{r})}{\pi \hbar^2} \mathcal{F}_{-\frac{3}{2}} \quad \frac{E_i - E_F}{kT} \quad , & 2 - D \end{cases} \end{aligned} \tag{C.3}$$

In (C.3) it is assumed that the change in conduction band only affects the density and not the wavefunctions. This approximation leads to a diagonal Jacobian, and causes a slower convergence in QDs at low temperature. A damping factor $\alpha < 1$ can be introduced in (C.1) to damp oscillations of F

$$V_i^{n+1} = V_i^n - \alpha J_{ij}^{-1} F_j$$

Similarly, the derivatives for donor and acceptor incomplete ionized densities with respect to the electrostatic potential can be calculated as follows

$$\frac{\partial n_{\text{semicl}}(\mathbf{r})}{\partial V(\mathbf{r})} = \frac{qN_C}{kT} \mathcal{F}_{-\frac{1}{2}} \quad \frac{E_F - E_C(\mathbf{r})}{kT} \tag{C.4}$$

$$\frac{\partial p_{\text{semicl}}(\mathbf{r})}{\partial V(\mathbf{r})} = -\frac{qN_V}{kT} \mathcal{F}_{-\frac{1}{2}} \quad \frac{E_V(\mathbf{r}) - E_F}{kT} \tag{C.5}$$

Newton method along with damping schemes such as under-relaxation [129], trust region [130] and others [131–134], works well when density of states is smooth.

D. PREDICTOR-CORRECTOR METHOD

The Schrödinger-Poisson equation system can be solved self-consistently using Newton's method as shown in Appendix C. For 3D, 2D and 1D periodicity the DOS (Fig. D is a smooth function of energy and Newton's method converges even at low temperatures. Newton's method has problems with convergence for 0D DOS (QDs) at low temperature because the energy levels are delta-function like. The Predictor-Corrector method can be used in this case.

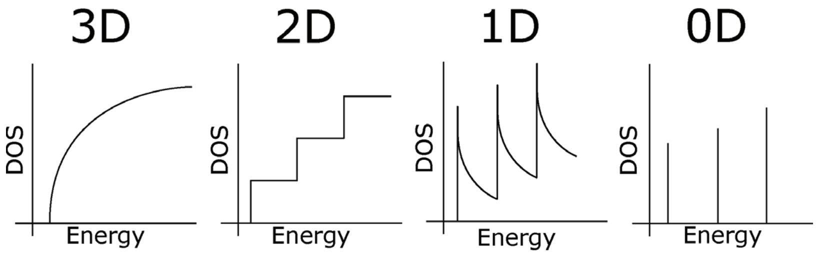

Figure D.1. Density of states (DOS) for periodicity in 3, 2, 1 and 0 directions.

This method relies on separating the non-linearity between 3D Schrödinger and Poisson equation and putting it into the Poisson equation. It was introduced for 1D and 2D periodic systems by Trellakis et. al. [108], and extended to quantum dots by Gao et. al. [68]. A derivation for quantum dots following that of Trellakis et. al. is presented here. In this method, the equations are decoupled by writing the quantum density approximately as a function of potential. The non-linear equation containing this approx. density is solved in an inner loop (Predictor) and the update carried to outer loop (Corrector) as shown in fig. D.2.

The variation in electronic charge density in terms of variation of eigenvalues and eigenfunctions with respect to the potential is first expanded. Here, all three are assumed to be functionals of the potential.

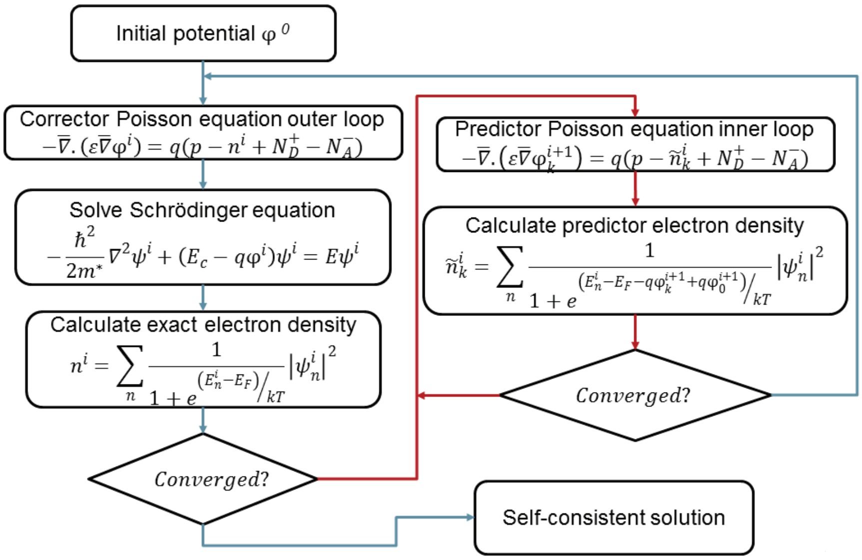

Figure D.2. Flow chart of the Predictor-corrector method. Inner loop uses Newton's method to solve predictor Poisson equation and gives a potential update to the outer Schrödinger solver. Initial potential is obtained by solving Poisson equation with semi-classical density.

$$\tilde{n}\left[V+\delta V\right] = \tilde{n}\left[V\right] + \delta\tilde{n}\left[V,\delta V\right],$$

$$\begin{aligned}\delta\tilde{n}\left[V,\delta V\right] &= \delta \underset{i}{} \frac{\left|\psi_i\left[V\right]\right|^2}{1+\exp\left(E_i\left[V\right]-E_F\right)/kT} \\ &= \underset{i}{} -\frac{\delta E_i\left[V,\delta V\right]}{kT}\frac{\left|\psi_i\left[V\right]\right|^2\exp\left(E_i\left[V\right]-E_F\right)/kT}{\left(1+\exp\left(E_i\left[V\right]-E_F\right)/kT\right)^2} \\ &+ \underset{i}{} \frac{2\psi_i\left[V\right]\delta\psi_i\left[V,\delta V\right]}{1+\exp\left(E_i\left[V\right]-E_F\right)/kT}\end{aligned}$$

Next, non-degenerate first order perturbation theory is applied for computing $\delta\psi_i\left[V,\delta V\right]$ and $E_i\left[V\right]$

$$\delta\psi_i\left[V,\delta V\right] \approx -q \underset{j,j=i}{} \psi_j\left[V\right]\frac{\psi_j|\,\delta\hat{V}\,|\psi_i}{E_i\left[V\right]-E_j\left[V\right]}$$

$$\delta E_i\left[V,\delta V\right] = -q\ \ \psi_i|\,\delta\hat{V}\,|\psi_n$$

Substituting this back in the previous equation and using the symmetry of indices j and i,

$$\delta\tilde{n}\left[V,\delta V\right] \approx \underset{i}{} \frac{q}{kT}\frac{\left|\psi_i\left[V\right]\right|^2 \exp\left(E_i\left[V\right]-E_F\right)/kT}{\left(1+\exp\left(E_i\left[V\right]-E_F\right)/kT\right)^2}$$

In deriving this, the assumption that the basis is complete is made and the derivative of the Fermi function is approximated as follows,

$$\frac{2\left(1+\exp\left(E_i\left[V\right]-E_F\right)/kT\right)^{-1}}{E_i\left[V\right]-E_j\left[V\right]} \approx -\frac{1}{kT}\frac{\exp\left(E_i\left[V\right]-E_F\right)/kT}{\left(1+\exp\left(E_i\left[V\right]-E_F\right)/kT\right)^2}$$

$$\underset{j,j=i}{} \psi_j\left[V\right]\ \ \psi_j\right|\delta\hat{V}\left|\psi_i\ \ = \delta V\psi_i\left[V\right]-\psi_i\left[V\right]\ \ \psi_i\right|\delta\hat{V}\left|\psi_i\right.$$

. This approximation gives an non-exact and diagonal Jacobian. Thus, the Predictor density and it's derivative with respect to potential can be written as

$$\begin{aligned}\tilde{n}\left(\delta V\right) &= \underset{i}{} \frac{\left|\psi_i\right|^2}{1+\exp\left(E_i-E_F-q\delta V\right)/kT},\\ \frac{\partial n}{\partial V} &= \underset{i}{} \frac{\left|\psi_i\right|^2\exp\left(E_i-E_F-q\delta V\right)/kT}{\left(1+\exp\left(E_i-E_F-q\delta V\right)/kT\right)^2}\end{aligned} \tag{D.1}$$

Thus, the predictor density only on change in potential from the outer loop and wavefunctions calculated in the outer loop.

E. AGREEMENTS FOR REUSE OF PUBLISHED PAPERS

American Physical Society
Reuse and Permission License

13- n- 018

This license agreement between the American Physical Society (APS) and Harshad Sahasrabudhe ("You") consists of your license details and the terms and conditions provided by the American Physical Society and SciPris.

Licensed Content Information

License Number:	**RN /18/JUN/005178**
License date:	13- n- 018
DOI:	10.1103/PhysRevB.97.085302
Title:	Optimization of edge state velocity in the integer quantum Hall regime
Author:	H. Sahasrabudhe et al.
Publication:	Physical Review B
Publisher:	American Physical Society
Cost:	USD $ 0.00

Request Details

Does your reuse require significant modifications : No

Specify intended distribution locations :	Worldwide
Reuse Category :	Reuse in a thesis/dissertation
Requestor Type:	Author of requested content
Items for Reuse:	Whole Article
Format for Reuse:	Electronic

Information about New Publication:

University / Publisher:	Purdue University
Title of dissertation/thesis :	Low temperature simulations framework for quantum dots and point contacts
Author(s):	Harshad Sahasrabudhe
Expected completion date:	l. 018

License Requestor Information

Name:	Harshad Sahasrabudhe
Affiliation:	Individual
Email Id:	harshad.sahasrabudhe@gmail.com
Country :	United States

American Physical Society
Reuse and Permission License

TERMS AND CONDITIONS

The American Physical Society (APS) is pleased to grant the Requestor of this license a non-exclusive, non-transferable permission, limited to Electronic format, provided all criteria outlined below are followed.

1. You must also obtain permission from at least one of the lead authors for each separate work, if you haven't done so already. The author's name and affiliation can be found on the first page of the published Article.
2. For electronic format permissions, Requestor agrees to provide a hyperlink from the reprinted APS material using the source material's DOI on the web page where the work appears. The hyperlink should use the standard DOI resolution URL, http://dx.doi.org/{DOI}. The hyperlink may be embedded in the copyright credit line.
3. For print format permissions, Requestor agrees to print the required copyright credit line on the first page where the material appears: Reprinted (abstract/excerpt/figure) with permission from [(FULL REFERENCE CITATION) as follows: Author's Names, APS Journal Title, Volume Number, Page Number and Year of Publication.] Copyright (YEAR) by the American Physical Society.
4. Permission granted in this license is for a one time use and does not include permission for any future editions, updates, databases, formats or other matters. Permission must be sought for any additional use.
5. Use of the material does not and must not imply any endorsement by APS.
6. APS does not imply, purport or intend to grant permission to reuse materials to which it does not hold copyright. It is the requestor's sole responsibility to ensure the licensed material is original to APS and does not contain the copyright of another entity, and that the copyright notice of the figure, photograph, cover or table does not indicate it was reprinted by APS with permission from another source.
7. The permission granted herein is personal to the Requestor for the use specified and is not transferable or assignable without express written permission of APS. This license may not be amended except in writing by APS.
8. You may not alter, edit or modify the material in any manner.
9. You may translate the materials only when translation rights have been granted.
10. APS is not responsible for any errors or omissions due to translation.
11. You may not use the material for promotional, sales, advertising or marketing purposes.

1 . The foregoing license shall not take effect unless and until APS or its agent, Aptara, receives payment in full in accordance with Aptara Billing and Payment Terms and Conditions, which are incorporated herein by reference.

1 . Should the terms of this license be violated at any time, APS or Aptara may revoke the license with no refund to you and seek relief to the fullest extent of the laws of the USA. Official written notice will be made using the contact information provided with the permission request. Failure to receive such notice will not nullify revocation of the permission.

14. APS reserves all rights not specifically granted herein.
15. This document, including the Aptara Billing and Payment Terms and Conditions, shall be the entire agreement between the parties relating to the subject matter hereof.

VITA

VITA

Harshad Sahasrabudhe was born in Nagpur, Maharashtra, India. He completed his Bachelor of Engineering (Hons.) in Electrical and Electronics and Master of Science (Hons.) in Physics from Birla Institute of Technology and Science, Pilani, India in 2010. He worked as an Associate Member of Technical Staff in Oracle India Pvt. Ltd, Hyderabad from 2010 to 2011. He joined Purdue University in 2012 to pursue a Ph.D. degree in Physics. Harshad's Ph.D. work focuses on computational modeling of electrostatics in nano-electronic devices.